Exotic quantum phases and interactions in cold atomic systems

MÁRTON KANÁSZ-NAGY

Advisor: Prof. Gergely Zaránd

Budapest University of Technology and Economics, 2015

"I therefore believe it's true that with a suitable class of quantum machines you could imitate any quantum system, including the physical world."

— Richard P. Feynman, *Simulating Physics with Computers*

Contents

1 Introduction

The goal of reaching quantum degeneracy with ultracold gases triggered an immense interest in the field of atomic, molecular and optical physics, and has led to a major experimental development in cooling, trapping and manipulation of these gases. These efforts culminated in the first experimental demonstration of Bose–Einstein condensation (BEC) of weakly interacting bosonic atoms, forming an essentially pure condensate at very low temperatures [1–3]. This breakthrough, and the achievement of Fermi degenerate quantum gases a few years later [4, 5], marked the starting of the era of investigating quantum phenomena with ultracold gases. Honoring the first significant step in this direction, the 1997 Nobel prize in Physics was awarded to Steven Chu, Claude Cohen-Tannoudji, and William D. Phillips for the development of methods to cool and trap atoms using laser light and magnetic fields. The temperature regime reached in these experiments was three to four orders of magnitude lower than the ones ever obtained before. Just four years later, Eric A. Cornell, Wolfgang Ketterle and Carl E. Wieman also received the Nobel prize for the realization of Bose-Einstein condensates, hallmarking an era of quantum emulation experiments of many-body physics.

These developments were an important leap towards realizing Richard P. Feynman's idea of quantum emulators [6]. Feynman tried to find a way around the fundamental problem, that the dimension of the parameter space of many-body quantum systems, and thus the computational load of simulating it with classical computers, increases exponentially with the system size – an obstacle to numerical simulations to date. This limitation can only be circumvented by invoking quantum mechanics, and emulating the intricate behavior of the many-body system at interest using simpler quantum systems that are easier to handle experimentally. He argued that, just like the basic phenomena of field theory are well imitated by many phenomena in solid state theory, many quantum phenomena could be effectively

modeled by the low energy degrees of freedom of even simpler quantum systems.

The goal of simulating ever greater variety of physical systems using the low energy degrees of freedom of dilute atomic vapors has led to a subtle experimental machinery, with which almost all relevant parameters of an ultracold gas can be tuned. For a number of years after the achievement of quantum degeneracy with bosons and fermions, a main focus in ultracold atomic physics was the exploration of phenomena associated with coherent matter waves in weakly interacting gases. Notable examples include interference experiments with overlapping Bose-Einstein condensates [7], Josephson oscillations [8] and the realization of topological excitations, such as vortices, vortex lattices and solitons [9–13]. Furthermore, fermionic condensates have been the source of various novel phenomena associated with fermionic superconductivity [10]. Common characteristics of these systems is the existence of a coherent order parameter, allowing an effective single particle description of the system, by treating interactions on the mean-field level. The Gross-Pitaevskii and Bogoliubov-de Gennes equations for bosons and fermions, respectively, allow for the efficient description of time dependent dynamics and condensate excitations by non-interacting quasi-particles.

The possibility to control atom-atom interactions through the so-called Feshbach resonances, however, opened up a completely new arena of physical phenomena, by allowing experimentalists to tune the gases into the strongly interacting regime. Here, the effective cross-section of colliding particles can be several thousand times the effective size of the atoms, and scattering lengths become comparable to the average interparticle distance[1]. In this regime, even these extremely dilute gases can no longer be described by a picture based on non-interacting quasi-particles, and quantum correlations play a determining role. Such systems had been previously been thought of as belonging to the field of strongly interacting quantum liquids in solids, stars and nuclei, and have fascinated physicists in the condensed matter and particle physics community for decades. However, in many cases, these correlated states remained elusive to analytical and numerical investigations, due to their complex nature. Rather counter-intuitively, they can be realized in dilute ultracold gases today. Ultracold systems thus provide a flexible tool to create model systems, that grasp the essence of several strongly correlated physical phenomena.

A different approach to realizing strongly correlated many-body phases came from experiments with optical lattices. In these systems, standing waves of laser light produce a strong lattice potential for the atoms, realizing effectively a tunable version of the Hubbard model – an idealized model system of many strongly correlated problems in solid state physics. With their kinetic energy suppressed, atoms can form strongly interacting phases even at moderate values of their scattering lengths. For instance, loading a Bose-Einstein condensate into an optical lattice had made it possible to observe the quantum phase transition from a superfluid to a Mott insulator state [14].

[1] In ultracold gases, atomic interactions are typically characterized by the associated s-wave scattering lengths, see Sec. 2.6.

Strong confinement by a strong optical lattice in two or one spatial directions can also be used to create effectively one and two dimensional systems. In two dimensional systems, increased fluctuations can lead to interesting many-body phenomena, one of them being the Berezinskii-Kosterlitz-Thouless phase transition of bosons [15–18], with algebraically decaying correlation functions. One dimensional systems, on the other hand, provide a useful test ground for integrable systems, such as the Tomonaga-Luttinger liquid and the Tonks-Girardeau gas [19–22]. Furthermore, they provide new insights into the study of basic statistical mechanical phenomena, such as prethermalization [23]. In addition, by populating the different energy levels of the atoms, one can create novel kinds of multicomponent Bose and Fermi mixtures, as well as spinful condensates of almost arbitrary spin. The high flexibility of these systems have gradually promoted them to quantum emulators of many condensed matter and particle physics systems, as well as to sources of completely new physical phenomena, never observed before.

In this thesis, we shall investigate the correlated quantum states of various multicomponent ultracold atomic systems, with a special focus on their interactions and phase diagrams. We will also discuss one of the author's works on an exotic topological excitation. To study these phenomena, we shall use the machinery of field theoretical methods, as well as numerical simulations. In the second chapter, we will review some aspects of the experimental techniques used in current ultracold atomic experiments. We will focus on the basic aspects of cooling and trapping, optical lattices, magnetic Feshbach resonances, and detection techniques, including absorption imaging and time-of-flight imaging.

In the third chapter, we shall discuss how confinement modifies interactions in quasi-two dimensional quantum gases. In these systems, reduced dimensionality leads to an increased role of fluctuations, and it strikingly modifies interactions between the particles – leading to exotic interaction resonances, induced by the confinement. Although one-component systems have been the focus of intense experimental investigations [17, 18], two-component systems are much less explored. To investigate their properties, especially their phase diagram, *independent* control of the interaction parameters between different species would be beneficial. However, with current methods using magnetic Feshbach resonances, these parameters can only be tuned simultaneously. In this part of the thesis, we will focus on two-component quasi-two dimensional quantum gases, and demonstrate how this interaction control can be reached by simple geometrical means. In particular, we will study the interaction between two species of bosons confined parabolically into two parallel layers. We will demonstrate the existence of interlayer confinement-induced interaction resonances that can be tuned by changing separation between the layers. They thus provide another experimental 'knob', besides the commonly used magnetic Feshbach resonances, to control interspecies interactions, in a purely geometrical way. These resonances are due to novel interlayer quasi-bound states that can be made increasingly long-lived by tuning layer separations. Furthermore, their increased lifetime makes it possible to observe these molecular states in the shaking spectrum of the two-dimensional layers, as will be demonstrated using detailed

many-body calculations for a thermal Bose gas.

In the fourth chapter, we will investigate the rich superfluid phase diagram of a weakly interacting three-component fermionic gas, which can be viewed as a considerably simplified model of large density quantum-chromodynamics, the theory of quarks. We will analyze how the interplay between superfluid and magnetic order parameters can lead to ferromagnetic superfluid states. We find various chemical potential driven first- and second-order transitions, as well as bicritical lines with special $O(2,2)$ symmetry. To capture these effects, a self-consistent "equation of motion" based approach, as well as a Gaussian variational approach will be introduced that both treat the superfluid and magnetic ordering unambiguously, in contrast to the frequently used Hubbard–Stratonovich transformation. Using this approaches, we will explore the full range of temperatures and chemical potentials and determine the global phase diagram.

In the fifth chapter, we will see how a single skyrmion topological excitation can be stabilized in the ultracold atomic setting by exploiting strong interactions. Skyrmions are three-dimensional monopole-like configurations of a vector order parameter field. They have been proposed theoretically in several fields of physics, however, they have thus far remained elusive to ultracold experiments due to various instability problems. In particular, skyrmions in earlier experiments were prone to gradually slipping away from the atomic trap. We shall discuss a novel proposal to circumvent this difficulty, and create an individual skyrmion of extreme stability, the so-called "Mott skyrmion". Specifically, by loading a spin-1 nematic superfluid (such as ^{23}Na) into an optical lattice, a Mott insulator core forms in the middle of the trap, surrounded by a superfluid shell that can naturally host a skyrmion configuration. The Mott core thus pins the skyrmion and keeps it from sliding away from the trap. A further advantage of this compact geometry is that the superfluid excitation spectrum of the skyrmion becomes discrete, and one can study how its quantum numbers change in the presence of the skyrmion, due to the skyrmion's topological winding. Such an interplay between topology and excitations is ubiquitous in the theory of topological excitations. However, since individual three-dimensional topological excitations have never been observed experimentally, it has only been observed in lower dimensional topological excitations, such as solitions (domain walls) [11, 12].

We shall summarize the scientific results in the thesis points in the Summary that synthesize the conclusions of Chapters 3, 4, and 5. Some of the more technical derivations are transferred to the appendices.

2

Basic concepts of ultracold gases

Gases at room temperature and atmospheric pressures are basically classical media. In most cases, even cooled down to very low temperatures, up to the point where they liquefy or solidify, they retain their classical nature, lacking any quantum mechanical characteristics. For instance, there is no indication of the bosonic or fermionic nature of gas atoms or molecules. Quantum mechanics only comes into play only at such low temperatures T, where the thermal de Broglie wavelength of particles,

$$\lambda_T = \frac{h}{\sqrt{2\pi m k_B T}}$$

characterizing the spatial extent of quantum mechanical wave packets, becomes comparable to the average interparticle spacing [24]. Here m denotes the particle masses, whereas k_B and h denote the Boltzmann and Planck constants, respectively. At such low temperatures, the gas enters the quantum degenerate regime, where the behavior of their constituents is determined by their bosonic or fermionic nature, and interesting many-body quantum phenomena can be observed. However, in case of gases at atmospheric pressure, this quantum limit corresponds to extremely low temperatures, where the gaseous state is only metastable.[1] In a typical gas, such as N_2 and Ne, three-body collisions are frequent enough to cause rapid crystallization, making the gas atoms freeze out and form solids as T is decreased. In experiments with ultracold gases, crystallization is circumvented by diluting the gas to the point where its lifetime becomes of the order of seconds and the quantum limit can be reached by lowering its temperature to the nK range. These systems are thus characterized by rather extreme conditions. Typical values of the density, $n \sim 10^{13}\,\mathrm{atoms/cm^3}$, are six orders of magnitude lower than those of a gas at room

[1] In contrast, due to their small mass and large density, electrons in a metal are quantum degenerate even at room temperatures.

temperature at atmospheric pressure. In such dilute gases, quantum-degeneracy is reached only at extreme temperatures, typically below $T \sim 100\,\mathrm{nK}$, at least four orders of magnitude lower than those achievable by the best cryostats today. These extremely fragile systems thus need very good isolation from their environments, they can only be realized in ultrahigh vacuum chambers, and are generally trapped and manipulated using laser light and magnetic fields. Typical experiments involve only $10^3 - 10^7$ atoms that are held together in a sub-millimeter sized magnetic or optical trap.

In this section, we will introduce the basic experimental techniques that made it possible to realize these special systems, requiring an enormous technological progress in the past 20 years of ultracold atomic experiments. We will start by describing basic cooling and trapping techniques using lasers and magnetic fields, with a short detour on the basics of light-atom interaction. Then, we shall introduce magnetic Feshbach resonances as means of flexibly controlling interactions by static magnetic fields. Finally, we will review the physics of optical lattices and that of the superfluid to Mott insulator phase transition.

2.1 Multicomponent and spinful condensates

Experiments with ultracold atoms provide a way to model multicomponent and multi-spin systems, by populating the different hyperfine states of atoms. Hyperfine splitting of energy levels is produced by the interaction between total electronic angular momentum and the nuclear spin[2]. This energy is in the $1\,\mathrm{K} - 100\,\mathrm{mK}$ range, three orders of magnitude smaller even than the fine structure of atoms. Yet, the temperature range of ultracold experiments is so low that the thermal collisions are insufficient to create transitions between different hyperfine states of the colliding atoms. Thus, atoms retain their hyperfine states, and they can be described as different atomic species, opening the way to model multicomponent condensates. Furthermore, atoms of even hyperfine spin isotopes are bosonic, whereas odd hyperfine spin isotopes are of fermionic nature. For instance, the two stable isotopes of lithium, ^{6}Li and ^{7}Li are fermionic and bosonic, respectively. This makes it possible to model bosonic systems, such as Bose-superfluids and Bose–Einstein condensates (BECs), as well as degenerate Fermi liquids in the ultracold atomic setting.

The hyperfine structure of certain elements makes it possible to create spinful condensates, with special symmetries of the atom-atom interaction. As an example, ^{23}Na and ^{87}Rb atoms possess states with hyperfine spin 1 and $SO(3)$ symmetric interactions [25–27] at zero magnetic field, see also Chapter 5.

[2]Due to the coupling between the core and the electrons, atomic energy levels can be characterized by their hyperfine spin $\mathbf{F} = \mathbf{J} + \mathbf{I}$. Here $\mathbf{I}$ stands for the nuclear spin, and $\mathbf{J}$ denotes the total electronic angular momentum, $\mathbf{J} = \mathbf{L} + \mathbf{S}$, given by the electronic orbital angular momentum, $\mathbf{L}$, and spin, $\mathbf{S}$.

2.2 Laser cooling

The interaction of atoms with photons has been traditionally used to probe properties of atoms – primarily their energy level structure in spectroscopy experiments. However, atom-photon interactions can also be used to manipulate the atom's internal degrees of freedom, such as its spin and orbital angular momentum, as well as its kinetic energy. This opens up the way for laser cooling of atomic gases and trapped ions. The idea of laser cooling is based on the resonant exchange of momentum between atoms and photons in a laser field, allowing to decrease the kinetic energy of the atoms, and thereby cooling the gas. Although the linear momentum exchanged may be tiny, several cycles of this process can take the thermal atoms to rest, vastly decreasing their temperature. Laser cooling has been originally proposed with the primary aim to reduce temperature broadening of atomic levels in ultrahigh spectroscopy experiments and in atomic clocks, and allowed to reach temperatures as low as a few hundred microkelvins [28, 29]. However, this technique has later found much broader use in atomic physics through a series of unexpected developments that allowed for reaching ever colder temperature ranges. Finally, this has led to the development of the experimental techniques used today with ultracold atomic vapors.

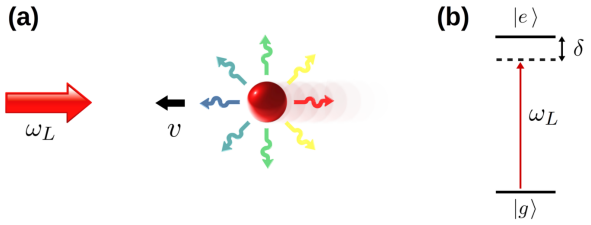

Figure 2.1: Doppler cooling scheme. An atom propagating towards laser, tuned below one of its atomic transition lines (**b**), becomes resonant to the laser field due to the Doppler effect. The momentum transfer between the atoms and photons that it absorbs and re-emits in random directions produces a net average force, that slows the atom down.

The simplest, and most widely used laser cooling technique is Doppler cooling, whose idea can be demonstrated by considering a two-level atom in a weak light field. The field is produced by a pair of counter-propagating laser beams, whose frequency ω_L is tuned slightly below that of the atomic transition frequency ω_A, as depicted schematically in Fig. 2.1. Thus, the atom constantly scatters photons by virtually absorbing and re-emitting them in isotropic directions. If the atom moves towards one of the lasers with velocity v, the laser frequencies exhibit opposite Doppler shifts $\delta\omega_L = \pm\omega_L\,(v/c)$. The frequency of the laser traveling opposite to the atom gets shifted towards resonance, whereas the other laser's frequency is pushed away from it. This imbalance of the left and right fluorescence processes, averaged over several cycles, leads to a velocity-dependent radiation pressure that reduces the atom's

velocity. This can be described by a net friction force, F, that slows down the atoms to temperatures below the mK range [30].

Three-dimensional cooling of untrapped atoms requires the use of pairs of lasers along all three coordinate axes. This configuration, besides the cooling effect described above, leads to a viscous confinement of the gas, the so-called "optical molasses" setting [31]. In an appropriately tuned laser field, the atoms have so short mean-free paths that it may take them a few hundreds of milliseconds to drift out from the trap, whereas propagating ballistically they would leave the trap on a millisecond timescale [30]. This mechanism is analogous to the confinement of particles in a viscous fluid.

The Doppler cooling mechanism is also used as the first step of experiments with ultracold atoms. In the usual setting a beam of alkali atoms, leaving an ion source with large velocity, needs to be slowed down for the atoms to be trapped and manipulated. In this case, only one laser, facing the atomic beam, is used, creating a net radiation force on the atoms that stops them roughly after a meter of flight.

2.3 Magnetic trapping

After slowing down the atoms and cooling them down to the μK regime by laser cooling techniques, they are usually confined using magnetic, optical or magneto-optical traps. Trapped gases allow for the application of more effective cooling mechanisms that can reduce the temperature until quantum degeneracy is reached. These traps make use of the effective potentials created for the atoms by a non-uniform laser field in case of optical traps, or by a spatially inhomogeneous Zeeman shift, created by magnetic trapping potentials, as we show below in this section.

2.3.1 Magnetic traps

The hyperfine interaction between the nuclear spin $\mathbf{I}$, and the total angular momentum $\mathbf{J}$, of electrons leads to a tiny hyperfine splitting of their energy levels. This splitting being nevertheless significantly larger than the temperature of the ultracold gas, the energy levels of the atoms are characterized by their hyperfine spin $\mathbf{F} = \mathbf{I}+\mathbf{J}$. The idea of a magnetic trap is to confine the atoms using an inhomogeneous magnetic field $\mathbf{B}(\mathbf{r})$ that acts as a parabolic potential for the atoms. The effect of the magnetic field can be described by the Zeeman term $U(\mathbf{r}) = (g_F \mu_B/\hbar)\ \mathbf{F}\cdot\mathbf{B}(\mathbf{r})$, with g_F and μ_B denoting the Landé g-factor, and the Bohr magneton, respectively. During its motion, the atom's spin precesses around the local magnetic field with a Larmor frequency $\hat{\omega}_L(\mathbf{r}) = g_F\mu_B|\mathbf{B}(\mathbf{r})|/\hbar$. As long as the change of the magnetic field along the atom's path is adiabatic, as specified by the condition $\frac{d}{dt}\hat{\omega}_L(\mathbf{r}(t)) \ll \hat{\omega}_L^2(\mathbf{r}(t))$, the precession of the magnetic moment follows the local direction of the field, and the atom retains its hyperfine spin component, m_F. Thus, the magnetic field creates an effective potential for the atoms

$$U(\mathbf{r}) = g_F \mu_B\, m_F\, |\mathbf{B}(\mathbf{r})|.$$

This technique allows for trapping an atomic cloud already at a few tens of microkelvins. However, one of its important limitations is that magnetic traps cannot confine atoms in all hyperfine states, since the Maxwell equations do not allow for static magnetic field configurations whose absolute value has a maximum at a certain point in space, only minima are allowed[3]. Thus, only such traps can be created, in which the magnetic field strength is minimal in the middle, and gradually increases in the radial direction. These allow to trap only the so-called low field seeking states that acquire a lower Zeeman energy at lower magnetic fields [32, 33].

2.4 Evaporative cooling

The use of the evaporative cooling mechanism has been the key technique to achieve Bose-Einstein condensation in magnetic or so-called magneto-optical traps. The basic idea is to gradually lower the trapping potential and thus let the most energetic atoms leave the trap. Meanwhile, the gas thermalizes through elastic collisions. Like a cup of coffee cools through its fastest atoms leaving the coffee's surface, evaporative cooling can reduce the gas temperature orders of magnitude lower, down to quantum degeneracy – at the cost of simultaneously loosing the majority of atoms [34]. Thus, evaporative cooling requires large initial particle numbers and also high initial densities in order to assure fast thermalization rates. To become efficient, elastic collisions, leading to thermalization, have to be significantly more frequent than inelastic collisions that cause losses and heating.

2.5 Optical trapping

The first observation of Bose-Einstein condensates in a series of remarkable experiments with ultracold atomic vapors [1–3] led to a well-established recipe for reaching the condensate phase: the atomic vapor is first precooled to the sub-millikelvin temperatures, typically by laser cooling techniques and then transferred to a magnetic trap. Further cooling to the BEC phase is then achieved by evaporative cooling in a magnetic or magneto-optical trap, often using forced evaporation [34], see also Sec. 2.4.

However, an external magnetic field destroys the special spin symmetries of certain spinful condensates. Therefore, by definition, the above mentioned magnetic traps are unsuitable for studying the rich physics of these systems (see Chapter 5). Thus, the interest in multicomponent and spinful condensates led to the development of all-optical trapping techniques. These methods make use of the energy shift of the atoms in a strong laser field that 'dresses' the atoms with photons, and the resulting quasi-particles (the so-called dressed states) have an energy that depends

[3] Assuming that $\mathbf{B}^2$ acquires a local maximum at a point, all eigenvalues of the matrix $\partial_i \partial_j \mathbf{B}^2$ should be negative here. This would imply that the trace of this matrix would also be negative. However, since the static Maxwell equations imply $\Delta \mathbf{B} = \nabla(\nabla \cdot \mathbf{B}) - \nabla \times (\nabla \times \mathbf{B}) = 0$, the trace $\mathrm{Tr}(\partial_i \partial_j \mathbf{B}^2) = \Delta \mathbf{B}^2 = 2\left(\mathbf{B} \cdot \Delta \mathbf{B} + \sum_i (\partial_i \mathbf{B})^2\right)$ is positive.

on the intensity of the local laser field. In general, "red-detuned" lasers, with a frequency below an atomic transition, attract atoms to high laser intensity regions, whereas blue-detuned lasers, tuned above the transition energy, repel atoms. Thus, a strong red-detuned laser focused sharply to a point can create a parabolic confinement potential to the atomic vapor, and can hold spinful condensates as well [35].

In the remaining part of this chapter, we shall review the basic concepts of atom-photon interactions in a strong laser field in order to understand the mechanism beyond optical forces acting on atoms, and we will discuss basic trapping geometries.

2.5.1 Atoms in strong laser fields

The absorption and emission processes of an atom in a laser field leads to radiative forces that fluctuate around their mean value. On time scales much larger than the radiative lifetime, the fluctuations average out, and the resulting average forces lead to intriguing effects, such as Doppler cooling. For a slowly moving atom, there are two parts of the mean radiative force. The first part is related to the phase gradient of the laser wave and leads to the radiation pressure discussed earlier in the context of Doppler cooling [36]. The second part is related to the intensity gradient of the laser, and it is often referred to as the dipole force [36, 37]. As we discussed in the first part of this chapter, the dipole force can be exploited for all-optical trapping using an inhomogeneous laser field.

The radiation-pressure force can be analyzed in detail in terms of fluorescence cycles involving the spontaneous absorption and emission of photons. Such perturbative treatment, however fails to explain some characteristics of the dipole force, especially at high laser intensity. In that case, a new theoretical treatment is required that considers first the energy levels of the combined atom-photon system, whose energy gets shifted by their coupling produced by the dipole moment of the atom. This approach is especially appropriate if the energy splitting in the combined system, the so-called generalized Rabi frequency, Ω, is large compared to the rate of spontaneous emission or damping rate, Γ [36]. Then, as a second step, one can take into account the effect of spontaneous emission to the other empty modes of the electromagnetic field that leads to relaxation mechanisms between the dressed states. However, the treatment of these processes is beyond the scope of this section.

In order to investigate the dipole force, let us consider a two-level atom with a ground state $|g\rangle$ and an excited state $|e\rangle$, with an energy splitting ω_A. Let us furthermore neglect the empty modes of the electromagnetic field, and consider only the laser mode of frequency ω_L. The interaction of the atom to the laser field is customarily described within the dipole approximation, taking into account the coupling between the atomic dipole moment to the local electric field [38].

In the absence of an atom–laser coupling, the eigenmodes of the of the dressed Hamiltonian have two almost degenerate branches $|g, n+1\rangle$ and $|e, n\rangle$, for all integer number n of photons (see Fig. 2.2 a). These manifolds of states are separated by the energy $\hbar\omega_L$ of adding an additional laser photon to the system, whereas the energy separation between the states within a manifold is simply the laser detuning

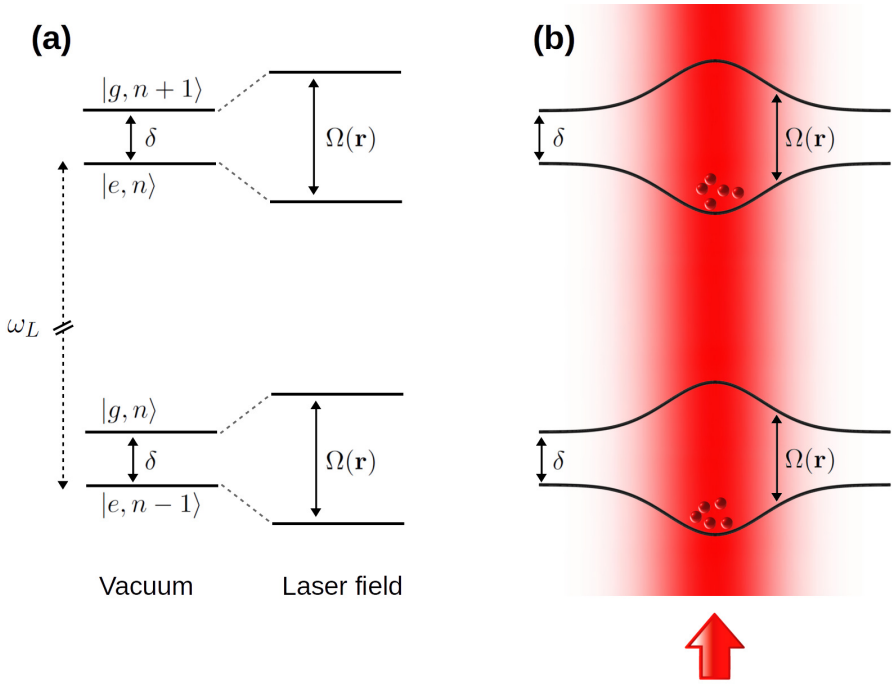

Figure 2.2: Energy of atomic levels in a strong laser field. (**a**) In the absence of a dipole coupling (left), the energy levels are simply split by the laser detuning. However, in a strong laser field, the scattering of photons due to the atom's matrix element couples the dressed states $|g, n+1\rangle$ and $|e, n\rangle$ that leads to a splitting of their energy levels, given by the generalized Rabi frequency Ω. (**b**) In a spatially varying red-detuned laser field, the variation of $\Omega(\mathbf{r})$ leads to optical trapping of the ground state atoms in the high-intensity regions. In the small intensity regions, the energy splitting of the levels simply coincides with the laser detuning δ.

$\delta = \omega_L - \omega_A$ (see Fig. 2.2.a). The dipole interaction then couples these states by making an atom in its excited state $|e, n\rangle$ emit a photon into the laser field and jump back to its ground state $|g, n+1\rangle$, and vice versa. If the detuning is small, $\delta \ll \omega_L, \omega_A$ [36], other absorption and emission processes can be neglected, and we can determine the dressed energy eigenstates of the coupled system, whose splitting is given by the generalized Rabi frequency [38]

$$\Omega(\mathbf{R}) = \sqrt{\Omega_0(\mathbf{R})^2 + \delta^2},$$

with $\Omega_0(\mathbf{R}) \propto \sqrt{I(\mathbf{R})}$. The dependence of the dressed state energies on the laser intensity leads to trapping effects in spatially inhomogeneous laser configurations. Far from the beam, the dressed states just coincide with the bare ones, whereas in the beam center their splitting is determined by the local Rabi frequency that is always greater than the detuning, see Fig. 2.2. This energy difference leads to an effective potential, whose sign depends on the laser detuning. In the red-detuned

case, the atomic ground state $|g, n+1\rangle$ is below its excited state $|e, n\rangle$. As the atom moves adiabatically towards increasing laser intensities, these two states get mixed by the atomic dipole matrix element, and the atom, originally in its ground state, remains in the lower energy state, whose energy becomes lowered towards the center of the laser beam. This mechanism creates an attractive potential for the atom that is dragged to the large intensity region of the laser. The opposite mechanism leads to a repulsive potential in case of blue-detuned lasers. It can be shown that the depth of this potential is proportional to the laser intensity, and is inversely proportional to the detuning [37]

$$U(\mathbf{R}) = \hbar \left(\pm\Omega(\mathbf{R}) - \delta(\mathbf{R}) \right) \simeq \frac{\Omega_0^2(\mathbf{R})}{\delta} \propto \frac{I(\mathbf{R})}{\delta}.$$

This formula suggests that one can reach strong optical trapping frequencies either by increasing the intensity of our trapping laser or tuning the laser frequency close to resonance. It turns out, however that the latter approach leads to undesired heating of the gas since atoms increasingly scatter laser photons close to resonance. This effect can be taken into account by considering the coupling of the dressed states to the empty modes of the electromagnetic field, responsible for spontaneous emission of fluorescence photons that is facilitated by the non-zero matrix elements of the atomic dipole coupling. It can be shown that close to the resonance, the scattering rate of photons is given by the inverse *square* of the detuning [37],

$$\Gamma_{sc}(\mathbf{R}) \propto \frac{I(\mathbf{R})}{\delta^2},$$

that leads to vastly increased heating processes close to resonance. Thus optical dipole traps usually apply lasers tuned far from resonance as compared to the natural linewidth of the atomic transition, in order to reduce unwanted heating effects, and strong traps are achieved by ramping up laser intensities.

2.6 Interactions

So far we have considered experimental tools to trap and cool ultracold vapors to the quantum degenerate regime, and neglected interactions between the atoms. Many properties of these quantum gases, including the thermalization rates and condensate density profiles, are, however, determined by two-particle interactions.

Furthermore, with the advent of magnetic Feshbach resonances, experiments could reach the strongly interacting regime, where many-body effects, rather than simple quasi-particle dynamics dominate the behavior of the system. Before diving into the many-body physics of ultracold gases, we discuss in this chapter the basic interaction mechanisms in gases of neutral atoms, and investigate how the interaction strength can be tuned in these systems almost arbitrarily.

2.6.1 Ultracold elastic collisions

Ultracold gases are so dilute that interactions predominantly manifest in two-particle collisions. Furthermore, the kinetic energy of the particles is usually low enough so that their interaction cannot create transitions between different hyperfine levels thus the collisions are typically elastic. The elastic scattering properties of two neutral atoms are usually described by an interaction potential $V_0(\mathbf{r})$, whose attractive Van der Walls tail at large distances, $V_0(\mathbf{r}) \sim -1/r^6$, is cut-off by an almost hard-core repulsive potential when the atoms are close to each other. Since the interactions depend on the relative position of the particles $\mathbf{r} = \mathbf{r}_1 - \mathbf{r}_2$, their center of mass motion trivially decouples from their relative motion. Introducing their relative momentum $\mathbf{p} = (\mathbf{p}_1 - \mathbf{p}_2)/2$ and reduced mass $m_r = m_1 m_2/(m_1 + m_2)$, their motion is determined by the Schrödinger equation

$$\left(\frac{\mathbf{p}^2}{2m_r} + V_0(\mathbf{r})\right)\psi_k(\mathbf{r}) = \epsilon_k\,\psi_k(\mathbf{r}), \tag{2.1}$$

at an incoming relative momentum k and energy $\epsilon_k = \hbar^2 k^2/2m_r$. Since an ultracold gas is so dilute that the typical atom-atom distance is several hundred times larger than the characteristic size of atoms, the scattering is completely characterized by the large distance behavior of the relative wave function,

$$\psi_k(\mathbf{r}) \sim e^{ikz} + f_k(\vartheta)\frac{e^{ikr}}{r},$$

where $f_k(\vartheta)$ denotes the scattering amplitude[4], and the direction of scattering is given in polar and azimuthal coordinates, φ and ϑ, respectively.[5] For a spherically symmetric interaction potential the relative angular momentum is conserved and the scattering states can be expanded in terms of their angular momentum channels, l. Importantly, scattering channels of non-zero angular momentum are typically frozen out in an ultracold gas. In these channels, the kinetic energy associated with the angular motion leads to a centrifugal energy barrier, typically in the range of 1 mK for alkali atoms. At temperatures below that, usually the lowest-angular-momentum scattering channel dominates: s-wave ($l = 0$) for bosons and different fermionic species, p-wave ($l = 1$) for identical fermions [39].

The scattering amplitudes can then be determined at ease by solving Eq. (2.1). We find that, at energies much lower than the centrifugal barrier the s-wave scattering amplitude takes on the simple form

$$f_k = -\frac{a}{1 + ika}, \tag{2.2}$$

[4]The scattering cross-section of the gas is related to the scattering amplitudes $f_k(\vartheta)$ as $\sigma_k = 2\pi \int_0^\pi d\vartheta\, \sin\vartheta\, |f_k(\vartheta)|^2$.

[5]Since the interaction potential is assumed to be spherically symmetric, the scattering amplitudes do not depend on φ.

characterized by the s-wave scattering length a, as a single parameter [39]. Although the scattering length is determined by the interaction potential $V_0(r)$, the microscopic details of this potential are unimportant from the point of view of describing interactions in an ultracold gas. In fact *any* sufficiently fast decaying interaction potential with the same value of a leads to the same many-body behavior [24]. Actually, the use of the interaction potential to describe interactions is rather impractical, since the scattering length depends sensitively on the microscopic details of this potential. $V_0(r)$ is generally unknown and it is rather hard to determine exactly. Then, a small uncertainty in the potential may result in large errors in the scattering length. In practice, a is measured experimentally, and represents the most relevant information about the interaction potential in terms of low energy collisions.

The exact interaction potential is also ill-suited to describe condensates in thermal equilibrium. $V_0(r)$ usually hosts a number of bound states, whose binding energy is on the range of $1\,\mathrm{eV} \sim 10^4\,\mathrm{K}$, whereas the typical temperatures of these gases are more than 10 orders of magnitude lower, below the millikelvin range. This clearly shows that ultracold gases are in a meta-stable state, and they would solidify in thermal equilibrium. Therefore, the methods of equilibrium quantum statistical mechanics would be unable to describe the long-lived metastable quantum phases of these ultracold gases. This is why even in exact quantum Monte Carlo calculations $V_0(r)$ is replaced by a hard-sphere potential [40].

2.6.2 Pseudopotential approximation

The key idea to circumvent the above difficulties is to use a simple potential that reproduces the appropriate scattering length, providing a useful mean-field treatment for weakly interacting gases. A model potential satisfying these requirement is the zero range Fermi pseudopotential, acting on a two-particle wave function $\psi(\mathbf{r})$ in the center of mass frame as

$$V(\mathbf{r})\psi(\mathbf{r}) = \frac{4\pi\hbar^2 a}{2m_r}\,\delta^{(3)}(\mathbf{r})\,\frac{\partial}{\partial r}\,(r\,\psi(\mathbf{r}))\,,$$

where $\mathbf{r}$ stands for the relative coordinate and the derivative term just provides regularization for the wave function. Indeed, when the wave function is regular for $r \to 0$, the regulator has no effect, and the pseudopotential can be merely viewed as a pure Dirac delta potential. However, for wave functions with a $1/r$ singularity, as is usually the case for scattering states and bound states of the pseudopotential, the derivative term simply removes the singular part of ψ.

The pseudopotential above reproduces the low energy scattering amplitudes Eq. (2.2) for all values of k. To see this, we reformulate the two-particle scattering problem at an incoming energy $\epsilon_k = \hbar^2 k^2/(2m_r)$ in Eq. (2.1) as

$$(\Delta + k^2)\psi_k(\mathbf{r}) = \frac{2m_r}{\hbar^2}\int d^3r'\,\delta^{(3)}(\mathbf{r}-\mathbf{r}')\,V(\mathbf{r}')\psi_k(\mathbf{r}'),$$

with the exact interaction potential substituted by the pseudopotential $V(\mathbf{r})$. One can find the solution of this equation by making use of the three-dimensional retarded Green's function

$$G^{3\mathrm{D}}_{\epsilon_k}(\mathbf{r},\mathbf{r}') = -\frac{1}{4\pi}\frac{e^{ik|\mathbf{r}-\mathbf{r}'|}}{|\mathbf{r}-\mathbf{r}'|}, \tag{2.3}$$

having the form of an outgoing spherical wave of momentum k. This Green's function satisfies the equation $(\Delta_{\mathbf{r}} + k^2)G^{3\mathrm{D}}_{\epsilon_k}(\mathbf{r},\mathbf{r}') = \delta^{(3)}(\mathbf{r}-\mathbf{r}')$, and thus through it, the solution of the two-particle scattering problem can be given in the self-consistent Lippmann–Schwinger form,

$$\psi_k(\mathbf{r}) = e^{i\mathbf{kr}} - \frac{2m_r}{4\pi\hbar^2}\int d^3r' \frac{e^{ik|\mathbf{r}-\mathbf{r}'|}}{|\mathbf{r}-\mathbf{r}'|}V(\mathbf{r}')\psi_k(\mathbf{r}'),$$

see also Chapter 3. In cases when the potential is weak, it is sufficient to iterate this equation to first order in V, and substitute the exact wave function in the integral simply with $e^{i\mathbf{kr}}$, leading to the Born approximation. This first order vertex gives a mean-field interaction parameter proportional to the scattering length a [24]. We thus see, that in case of weak interactions, the interaction of the gas is simply determined by the scattering amplitude, and it is thus attractive for $a < 0$ and repulsive for $a > 0$.

The two-particle scattering problem can, however, also be solved *exactly* within the pseudopotential approximation. Since the pseudopotential is concentrated to a single point, the integral in the Lippmann–Schwinger equation can be simply carried out yielding,

$$\psi_\epsilon(\mathbf{r}) = e^{i\mathbf{kr}} + f_k\frac{e^{ikr}}{r},$$

with the scattering amplitude given in Eq. (2.2). f_k has no angular dependence, since the pseudopotential scatters only in the s-wave channel, where it provides a full description of the low energy scattering properties of the gas.

2.6.3 Bound states of the pseudopotential

As we have discussed above, the true interaction potential V_0 has many bound states, irrespective of the sign of a. However, almost all of these bound states lie several orders of magnitude lower in energy than the energy scale of ultracold collisions. Thus, for the low energy scattering properties of the atoms, these bound states are irrelevant as long as no molecule formation occurs through three-body collisions. The scattering amplitude in this limit is only sensitive to bound states near zero energy, which show up as poles of the scattering amplitudes $f_{\mathbf{k}}$ in the upper complex half-plane $k = i\kappa$, with binding energy $\epsilon_B = \hbar^2\kappa^2/(2m_r)$ [41]. The pseudopotential, in particular, captures a single bound state for $\kappa = 1/a > 0$ in case of positive scattering lengths, with a binding energy $\epsilon_B = \hbar^2/(2m_r\, a^2)$. By solving the Schrödinger equation (2.1), we indeed find a bound state wave function corresponding to this pole

$$\psi_B(\mathbf{r}) = \frac{1}{\sqrt{2\pi a}}\frac{e^{-r/a}}{r}, \tag{2.4}$$

with a characteristic length related to the binding energy. When ϵ_B is close to the continuum threshold, i.e. in case of large positive scattering lengths, ϵ_B rather accurately corresponds to the energy of the highest lying bound state of the real two-particle interaction potential V_0 [39].

The existence of a bound state in a repulsive gas, and its absence for $a < 0$ is a rather counter-intuitive effect, related to the three-dimensional nature of the scattering problem. Here, a bound state near zero energy leads to negative phase shift of the scattered wave and thus to a positive scattering length [41]. The dimensionality of the system also plays an important role in the appearance of bound states. As we will show in Chapter 3 of this thesis, gases confined into two dimensions by a harmonic trapping potential host bound states both for positive and for negative values of the three-dimensional scattering length a.

2.6.4 Feshbach resonances

As we have demonstrated in the pseudopotential approximation, the scattering amplitude diverges as a bound state approaches the continuum threshold. This leads to increased interactions and scattering in the gas. In fact, the most direct way of reaching the strongly interacting limit in an ultracold gas is by increasing the scattering length beyond the average interparticle spacing via so-called Feshbach resonances [39, 42]. Such resonances generally appear when a bound state in a closed scattering channel is resonantly coupled to the scattering continuum in an open channel, as depicted in Fig. 2.3. This mechanism is similar to those found in accelerator experiments of high-energy physics, whereby the scattered particles are temporarily captured in the closed channel state and then decay into the continuum, so that the associated phase shift leads to a resonant increase of their interactions. The two channels may correspond for instance to two different hyperfine spin states of the colliding atoms, whose energy difference may be tunable through static magnetic fields, in case they have different magnetic moments. This magnetic tunability makes magnetic Feshbach resonances a particularly powerful tool in ultracold experiments [43, 44]. The many-body properties of the gas near the Feshbach resonance can still be described using the pseudopotential, with a diverging scattering length on resonance [39],

$$a(B) = a_{\mathrm{bg}} \left(1 - \frac{\Delta B}{B - B_0} \right).$$

Here a_{bg} denotes the background scattering length in the absence of coupling to the closed channel, whereas ΔB and B_0 describe the width and position of the resonance[6].

[6] Feshbach resonances can alternatively be induced by all-optical means, whereby the energy shift of the atomic levels is induced by laser shifts (see Sec. 2.5.1). However, these methods generally suffer from heating problems due to the spontaneous decay of atoms to the vacuum [45].

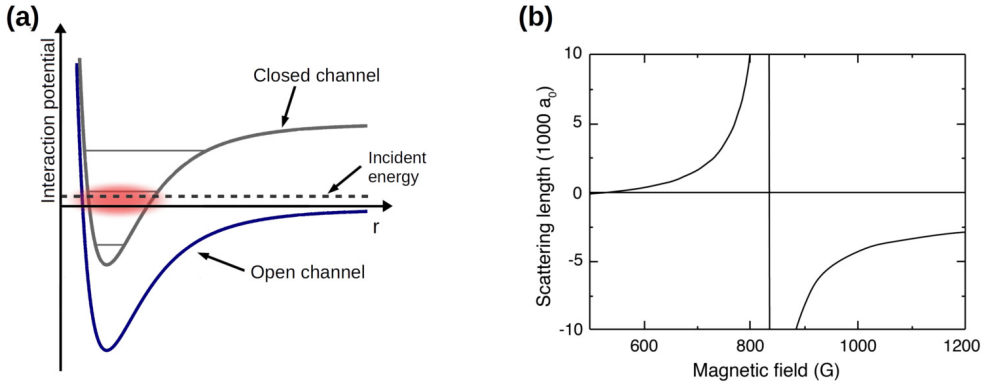

Figure 2.3: (**a**) Two-channel model for a Feshbach resonance. Incoming low energy atoms in the open channel resonantly couple to a bound state in the closed channel. The energy of this bound state can be varied using static magnetic fields B, and when it approaches the incident energy of the scattered atoms (close to the continuum threshold), we find an increased resonance in their interaction. (**b**) External magnetic field dependence of the scattering length a between the two lowest hyperfine levels of the fermionic species ^{6}Li, exhibiting a Feshbach resonance at $B_0 = 834\,\mathrm{G}$. Notably, this resonance has a zero-crossing at 534 G, where the gas is essentially non-interacting, and can be used to model single-particle physics. [Figure (**b**) is based on the results in Ref. [39].]

2.7 Optical lattices

Optical lattices, periodic potentials created by standing waves of far-detuned laser beams, are a versatile tool for confining atoms into strong periodic potentials, and thereby tuning their interaction. Through their use, quasi-one and quasi-two-dimensional condensates can be created. Furthermore, two- and three-dimensional optical lattices have been extensively used to mimic various crystal lattice configurations. As the kinetic energy of the atoms is suppressed by the lattice, their interaction becomes dominant – the system can thus be tuned into the strongly correlated regime simply by increasing the lattice potential. In this section, we briefly review the single-particle dynamics in an optical lattice, and then discuss the many-particle problem in terms of the Hubbard model, a paradigmatic model for several strongly correlated many-body phenomena in solid state physics. Importantly, optical lattices provide an experimental test grounds for emulating the intriguing many-body physics of the Hubbard model. As an important example relevant to this thesis, we will investigate the basic mechanisms behind the superfluid to Mott insulator transition in the bosonic Hubbard model, as well as its experimental characteristics.

2.7.1 Lattice Hamiltonian

A one dimensional optical lattice potential can be generated by a standing wave of a far off-resonant laser beam. The lattice has an intensity pattern of $\lambda/2$ periodicity, where λ denotes the laser wavelength[7]. As we discussed in Sec. 2.5, red-detuned lasers attract, whereas blue-detuned lasers repel atoms from intensity maxima, both configurations creating a periodic potential for atoms. Close to the center of a beam along the z axis, for distances much smaller than the beam waist, the optical potential can be written as

$$V_{\rm lat}^{\rm 1D}(\mathbf{r}) = V_0 \sin^2 kz,$$

with $k = 2\pi/\lambda$ denoting the laser's wavenumber. This potential creates quasi-two-dimensional pancake-like configurations of the gas, squeezed by the laser in the z direction, and confined much more weakly in the perpendicular direction either through additional magnetic fields, or optically, by the waist of the lattice laser beam[8]. For typical experimental parameters, the harmonic trapping frequencies in this direction are rather small (usually of the order of 100 Hz), whereas along the laser beam it is often as strong as 100 kHz. Thus, for sufficiently deep optical lattices, the atoms can move only axially along the pancakes, and one can thus study the physics of two-dimensional quantum systems. By crossing two standing waves along two perpendicular axes, one can confine the atoms along both of these directions. One can thus create tube-like configurations that allow for the study of strongly correlated gases in one dimensions.

A three-dimensional cubic lattice potential

$$V_{\rm lat}^{\rm 3D}(\mathbf{r}) = V_0 \left(\sin^2 kx + \sin^2 ky + \sin^2 kz\right),$$

can be similarly created by overlapping three orthogonal standing waves[9]. The shape of the optical potential can be further varied in multiple laser configurations or in different geometries. For instance, triangular, honeycomb and kagome lattices can be created [46], as well as superlattice configurations, produced by superimposing lattices of commensurate spacings [47]. Furthermore, the use of holographic imaging allows one to create complicated optical lattice configurations as well as to induce disorder in a simple way [48].

In order to address single-particle dynamics, we recall that, single-particle eigenstates in an infinite periodic potential form Bloch bands, similar to the ones in solid state systems. According to Bloch's theorem [49], the energy eigenstates can be characterized by their band index n and their quasi-momentum $\mathbf{q}$. Their wave

[7] More generally, by using a pair of phase-locked, non-collinear laser beams, their standing wave pattern produces an optical lattice potential of even larger periodicity.

[8] Red-detuned lasers attract the atoms towards the beam center, where the intensity of the optical lattice is maximal.

[9] To avoid cross-interference between the laser beams, slightly different laser wavelengths can be used in each directions.

functions can be written in terms of the lattice periodic Wannier functions $u^{(n)}$,

$$\psi_{\mathbf{q}}^{(n)}(\mathbf{r}) = \frac{1}{\sqrt{\mathcal{N}}} \sum_j e^{i\mathbf{q}\mathbf{R}_j}\, u^{(n)}(\mathbf{r} - \mathbf{R}_j),$$

with a the normalization constant $\mathcal{N}$ and with $\mathbf{R}_j$ denoting the position of the lattice site j. The Wannier functions can be chosen to be centered at individual lattice sites $\mathbf{R}_j$, and they form an orthonormal basis for all bands n and lattice sites $\mathbf{R}_j$. In cases when the typical energy scale of the system's dynamics is much lower than the first band gap, it is sufficient to consider the lowest Bloch band, $n = 0$. For deep cubic lattices, $V_0 \gg E_r$, the confinement on a single site is approximately harmonic with a trapping frequency $\hbar\omega_0 = 2E_r\sqrt{V_0/E_r}$, that is of the order of several recoil energies, $E_r = \hbar^2k^2/2m$. Thus, the atoms can only move to neighboring sites by quantum tunneling [39, 50], with a nearest-neighbor hopping coefficient

$$\begin{aligned} J &= -\int d^3r\, u^{(0)*}(\mathbf{r} - \mathbf{r}_j) \left(\frac{\hbar^2}{2m}\nabla^2 + V_{\text{lat}}^{\text{3D}}(\mathbf{r}) \right) u^{(0)}(\mathbf{r} - \mathbf{r}_i) \\ &\simeq \frac{4}{\sqrt{\pi}} E_r \left(\frac{V_0}{E_r} \right) e^{-2(V_0/E_r)^{1/2}}. \end{aligned}$$

The exponential dependence of the hopping on the lattice depth shows that this parameter can be easily increased or suppressed at will through changing the laser intensity.

In order to describe many-body dynamics, it is instructive to express the lattice system's Hamiltonian in terms of field operators

$$\Psi(\mathbf{r}) = \sum_j u^{(0)}(\mathbf{r} - \mathbf{R}_j)\, a_j,$$

where a_j denotes the annihilation operator removing an atom at site j, and the bosonic or fermionic nature of these operators has to be in accordance with the quantum statistics of the atomic species used. In a real experiments, the atoms are also subject to an additional slowly varying parabolic trapping potential $V_{\text{trap}}(\mathbf{r})$. Their many-body eigenstates can then be described to a very good approximation by the Hubbard–Hamiltonian

$$H = -J \sum_{\langle i,j \rangle} a_i^\dagger a_j - \sum_i \left(\mu_i n_i + \frac{U_0}{2} n_i(n_i - 1) \right) \tag{2.5}$$

with the spatially dependent chemical potential $\mu_i = \mu_0 - V_{\text{trap}}(\mathbf{R}_i)$, setting the particle density in the trap. Here, $n_i = a_i^\dagger a_i$ stands for the particle number operator for the lattice site i, and the first summation goes over nearest neighbor sites $\langle i, j \rangle$. The last term in Eq. (2.5) describes the on-site interaction of atoms,

$$U_0 = \frac{4\pi\hbar^2}{m} a \int d^3r\, |u^{(0)}(\mathbf{r})|^4.$$

When the trapping is strong enough, the overlap between Wannier functions on neighboring sites is negligible, and the interactions in the optical lattice are captured to a very good approximation by this single term. In the deep-lattice limit $V_0 \gg E_R$, we may substitute the exact Wannier function with the Gaussian ground state of the local oscillator potential, and obtain

$$U_0 \simeq \sqrt{\frac{8}{\pi}}\, E_R \left(\frac{V_0}{E_R}\right)^{3/4} ka.$$

The polynomial dependence of U_0 on the lattice depth, in contrast to the exponential dependence of the hopping J, means that their ratio can be flexibly tuned by modifying the laser intensity in an experiment. Thus, by suppressing the kinetic energy, the system can be brought into a strongly interacting state $U_0/J \gg 1$ at ease.

2.7.2 The superfluid to Mott insulator transition

In this subsection, we study bosonic atoms in a deep optical lattice, and review the basic mechanism of the quantum phase transition between the superfluid and Mott insulator phases in the bosonic version of the Hubbard model, the so-called Bose–Hubbard model. In Chapter 5, we will rely on the concepts discussed here. In order to simplify our discussion, we consider a spatially homogeneous system. The Bose–Hubbard model describes the competition between tunneling, whereby atoms can decrease their kinetic energy through spreading over the lattice, and the repulsive on-site interaction that disfavors configurations with more than one particles on a particular site. By measuring the energy in terms of the on-site interaction, one can clearly see that the competition of the different ground-states of the system depends only on the dimensionless parameters J/U_0 and μ/U_0. In the limit $J/U_0 \gg 1$, the tunneling term dominates the Hamiltonian, and the system is in the superfluid state. In the non-interacting limit $U_0 \to 0$, in particular, the independent particles occupy the lowest ($\mathbf{q} = 0$) Bloch state, spreading all over the lattice with equal weights. Thus, the ground-state of an N-particle system on a lattice of M sites is a simple Bose–Einstein condensate

$$|\Psi_{\mathrm{SF}}\rangle_{U\to 0} = \frac{1}{\sqrt{N!}} \left(\frac{1}{\sqrt{M}} \sum_{i=1}^{M} a_i^\dagger\right)^N |0\rangle\,,$$

with $|0\rangle$ denoting the vacuum. In the thermodynamic limit $N, M \to \infty$ with fixed density $\overline{n} = N/M$,[10] this wave function approaches a product of local coherent states with their phases locked [14],

$$|\Psi_{\mathrm{SF}}\rangle_{U\to 0} \sim \prod_i e^{\overline{n} a_i^\dagger} |0\rangle\,.$$

[10] N and M are of the order of $10^5 - 10^6$ in standard experiments

The BEC ground state, favoring atoms spreading all over the lattice thus leads to a significant probability of finding more than one atom at a given site. As the interaction is turned on, this is, however, disfavored by the interaction energy.

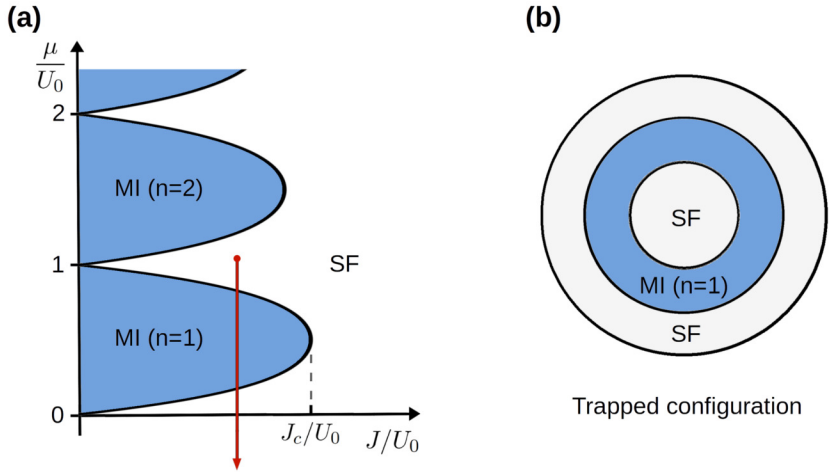

Figure 2.4: Phase diagram of the Bose–Hubbard model in terms of the hopping (J) and chemical potential (μ). (**a**) The incompressible Mott insulator phase occupies lobe-like structures, with increasing integer densities per site. This phase is surrounded by a superfluid phase with long-range phase coherence, and can take fractional values of the particle density. The red arrow denotes the variation of the chemical potential in a trapped ultracold atomic system, with the center of the trap being in the superfluid phase, with an average density $\overline{n} > 1$ particles per site. Towards the edges, the density is depleted, and the central superfluid core is surrounded by a series of Mott insulator and superfluid shells, in a wedding cake-like structure, (**b**).

In the opposite limit $J/U_0 \ll 1$, the interaction energy dominates the Hamiltonian, and, in the limit of zero hopping, the sites become independent. Since the on-site Hamiltonian is expressed in terms of the particle number operator, the on-site energy $\epsilon(n_i) = -\mu n_i + U_0\, n_i(n_i - 1)/2$ will be minimized if all sites are occupied by a fixed integer number n of bosons at all sites. For the chemical potential in the range $(n-1)U_0 < \mu < nU_0$, there will be exactly n particles at each site [51], and, the ground state takes on the form [14]

$$|\Psi_{\mathrm{MI}}\rangle|_{J\to 0} = \left(\prod_{i=0}^{M} \frac{a_i^{\dagger n}}{\sqrt{n!}}\right)|0\rangle\,,$$

with a well defined particle number at each site and a phase of maximal uncertainty. For small values of the hopping ($J \ll U_0$), the kinetic energy gain of a mobile particle excitation is exceeded by its cost in on-site energy in a large fraction of the phase diagram. Thus, density fluctuations in this region will be suppressed, representing

an insulating, incompressible state, a Mott insulator [51]. At larger values of the hopping, the energy gap for creating particles or holes decreases, leading to the appearance of these excitations, and creating non-zero conductance. In this regime, the system is in the superfliud phase, whose phase boundaries represent lobe-like structures, depicted in Fig. 2.4.

The superfluid phase is characterized by long-range phase coherence and an average particle density $\overline{n}$ that can take non-integer values as well. The superfluid to Mott insulator quantum phase transition was demonstrated first experimentally in an ultracold atomic system in Ref. [14], where the phase transition was identified through the onset of phase coherence. In an experimental system, the parabolic trapping potential leads to an ever decreasing value of the effective chemical potential towards the edges of the trap, indicated by the red arrow in the phase diagram in Fig. 2.4. If, for instance, the center of the trap is in the Mott phase with $n = 1$ particle per site, the density starts depleting at the point where the effective chemical potential reaches its critical value, leading to the onset of superfluidity. The central Mott core will thus be surrounded by a superfluid shell, see also Chapter 5.

2.8 Imaging techniques

Besides the wide use of optical systems to control and manipulate ultracold quantum gases, they constitute the basic tool physical measurements (see also Chapter 5). Since these gases are too fragile to be brought into contact with any macroscopic object, optical imaging is basically the only method through which useful information can be obtained from them. Probably the most basic measurement technique used in these experiments is absorption imaging, whereby a photographic image is taken of the cloud using a resonant laser. This enables one to detect the integrated in-trap density of the gas along one axis, through which the gas temperature can also be determined. Since the edges of the gas are usually dilute enough so that they can be considered weakly interacting, the density of these outer regions can be reliably calculated at the mean-field level. The gas temperature can thus be determined by fitting the theoretical curves to the measured density profiles of this region [39]. Absorption imaging has also been widely used in matter-wave interferometry experiments with Bose–Einstein condensates. Since the phase coherence of the condensates is conserved on the time scale of these experiments, one can detect interference patterns as density fringes when two parts of the condensate are brought into interference with each other [17].

Another widely used experimental method is the time-of-flight imaging technique, whereby the gas is first released from the trapping potentials and then imaged after some free expansion. This method has been used in a number of experiments to detect the superfluid to Mott insulator phase transition through the onset of phase correlations [14]. In case of an optical lattice system, if the lattice and the trapping potential is turned off abruptly, and interaction effects are negligible, a Bloch state with quasi-momentum $\mathbf{q}$ will become a superposition of plane waves with momenta

$\hbar(\mathbf{q}+\mathbf{G})$, where $\mathbf{G}$ denotes reciprocal lattice vectors. These plane waves propagate ballistically, and thus after long enough time of flight, the momentum distribution of the gas can be imaged using standard absorption imaging methods. In case of a non-interacting Bose–Einstein condensate that macroscopically populates the $\mathbf{q}=0$ Bloch wave, we find several interference maxima in the time-of-flight image. In general, in a deep optical lattice, the density distribution of the atomic cloud after an expansion of time t can be written as [39, 52]

$$\tilde{n}(\mathbf{r}) = \left(\frac{m}{\hbar\, t}\right)^3 \left| u^{(0)}\left(\mathbf{q}=\frac{m\,\mathbf{r}}{\hbar\, t}\right)\right|^2 C\left(\mathbf{q}=\frac{m\,\mathbf{r}}{\hbar\, t}\right), \tag{2.6}$$

where $u^{(0)}(\mathbf{q})$ denotes the Fourier transform of the Wannier function of the lowest band, providing an approximately Gaussian cut-off for large momenta, and

$$C(\mathbf{q}) = \sum_{i,j} \langle a_i^\dagger a_j \rangle\, e^{i\mathbf{q}(\mathbf{r}_i-\mathbf{r}_j)}$$

is the correlation function of the atoms in Fourier space, the central quantity of interest. The time of flight image is of course the integral of this density distribution along one axis, e.g. $\tilde{N}(x,y) = \int dz\, \tilde{n}(x,y,z)$. In case of a pure Bose–Einstein condensate the density $\tilde{n}$ exhibits a huge peak at the center of the first Brillouin zone $\mathbf{q}=0$, whereas we find several smaller peaks at the centers of the higher order Brillouin zones [14, 39]. In contrast, in the perfect Mott state, $J \to 0$, there are no long range correlations in the system, and the above sharp peaks in the time-of-flight image are absent. We thus only find a smeared out Gaussian profile, corresponding to the density of the lowest band Wannier function in momentum space, $|u^{(0)}(\mathbf{q})|^2$, whose size is on the order of that of the first Brillouin zone.

3

Confinement-induced molecules in bilayer gases

Two-dimensional quantum systems attract a significant attention in many areas of statistical physics, condensed matter and particle physics. Restriction of the particles into lower spatial dimensions leads to increased quantum and thermal fluctuations, as well as a stronger role of interactions [53]. Two-dimensionality gives rise to several exotic quantum phases, such as the Berezinskii–Kosterlitz–Thouless phase [15–18], quantum Hall phases [54–56] various spin liquid phases [57], it seems that two-dimensionality plays a determining role in high-temperature superconductivity as well [58]. Experiments with ultracold quantum gases provide in ideal setup to study these correlated low dimensional many-body phases, and many experiments have been carried in this direction in recent years. The possibility to confine the atoms into low dimensions by optical lattices and the tunability of many system parameters provide great opportunities to study these states in a flexible way. These optical systems also go beyond their condensed matter counterparts in that they allow for the creation of *multicomponent* fermionic and bosonic systems in restricted geometries, and thereby open the possibility of realizing new quantum states of matter [59–62], never observed before.

To realize these phases, however, one obviously needs to understand and control the interactions in the system. In this chapter, we shall thus study the interactions of a two-component ultracold gas confined into quasi-two dimensions by an optical potential. At sufficiently strong confinement, the perpendicular motion of the atoms is frozen, and the single-particle dynamics of the gas mimics that of a two-dimensional system. However, interactions get modified by the confinement in a very non-trivial way, leading to several counter-intuitive phenomena. While our theoretical understanding of interactions in one-component quasi-one- and quasi-two-dimensional sys-

tems is quite complete [63–66], two-component systems in two dimensions are much less explored, although they provide a particularly fruitful perspective to create analogues of interaction-driven condensed matter phases, such as excitonic Bose condensates [67, 68]. Furthermore, certain two-dimensional multicomponent systems, are predicted to exhibit exotic forms of the Berezinskii-Kosterlitz-Thouless transition due to the special structure of their topological excitations [69, 70].

In two-component systems, the *independent* control of interspecies interactions is of primary importance for the experimental study of their intriguing many-body phases and exotic quantum phase transitions. We will see in this chapter that, by separating the gases into a bilayer structure by the application of a perpendicular magnetic field gradient, their interactions can be tuned simply by changing the separation of the layers, and the two components can be made *strongly interacting* by actually separating them spatially. Although naive intuition suggests that the interaction shall vanish as the overlap between the atomic clouds diminishes, we discovered that the potential separating the layers actually leads to the emergence of (geometrically induced) interaction resonances at appropriate separations. These resonances originate from excition-like *interlayer* molecules, similar to the ones found in semiconductor quantum wells and one-dimensional ultracold gases [66–68, 71–73]. These giant molecules, both stable and unstable ones, are induced by the confining potential, and their spatial extent in the confined direction can be several times larger than the characteristic width of the individual clouds. Their existence leads to significant resonances of the interlayer atom-atom interaction through a similar mechanism that we find in accelerator experiments of high-energy physics. If the energy of two colliding atom approaches that of an unstable molecule, their interaction increases significantly due to a series of virtual processes, whereby they bind into the molecular state, and then decay into the continuum. Since the mechanism behind these geometrically induced resonances is similar to that of magnetic Feshbach resonances, we will occasionally refer to the resonances discussed here as "geometric Feshbach resonances". The resonant enhancement of interactions can be conveniently reached by tuning the layer separation, since the molecular binding energies depend sensitively on this parameter. This allows future experiments to control interspecies interactions independently from the other interaction parameters, and thereby discover a largely extended parameter range of two component condensates. Furthermore, the lifetime of the quasi-bound molecules vastly increases with growing layer separations that shall make them detectable in commonly used shaking experiments for the first time, as we demonstrate through detailed many-body calculations.

The results presented in this chapter are based on the following publication: M. Kanász-Nagy, E. A. Demler and G. Zaránd, *"Theory of confinement-induced interlayer molecular resonances"*, arXiv:1401.5798 (2014).

3.1 Interactions in exactly two dimensions

Let us first review the elastic scattering of a pair of atoms in the strictly two-dimensional case. Since the short-ranged interaction potential, $V_{\rm int}^{\rm 2D}(\boldsymbol{\rho}_1 - \boldsymbol{\rho}_2)$, depends only on the relative coordinates $\boldsymbol{\rho} = \boldsymbol{\rho}_1 - \boldsymbol{\rho}_2$ of particles, the scattering process can be entirely described in the center of mass frame. At large interparticle distances, the two-particle relative wave function asymptotically becomes the superposition of the incoming plane wave and a scattered wave,[1]

$$\psi^{\rm 2D}(\boldsymbol{\rho}) \simeq e^{i\mathbf{q}\cdot\boldsymbol{\rho}} - f^{\rm 2D}(\epsilon,\varphi)\sqrt{\frac{i}{8\pi q\rho}}e^{iq\rho},$$

determined by the scattering amplitude $f^{\rm 2D}(\epsilon,\varphi)$. Here $\epsilon = \hbar^2 q^2/m$ is the incoming energy at the relative momentum $\mathbf{q} = \mathbf{q}_1 - \mathbf{q}_2$ of particles, and φ is the angle of scattering. Similarly to the case of three-dimensional scattering discussed in Sec. 2.6, the low-energy scattering properties are determined by the s-wave contribution, and thus the scattering amplitudes become spatially isotropic at small energies, where the wavelength of the incident wave is much larger than the characteristic radius, $R_{\rm int}$, of the interaction potential [65].

Following Ref. [65], the scattering amplitudes can be obtained from the large distance behavior of the scattering states of the two-dimensional (relative) Schrödinger equation

$$\left(-\frac{\hbar^2}{m}\Delta_{\boldsymbol{\rho}} + V_{\rm int}^{\rm 2D}(\boldsymbol{\rho})\right)\psi^{\rm 2D}(\boldsymbol{\rho}) = \epsilon\,\psi^{\rm 2D}(\boldsymbol{\rho}).$$

At short distances, but outside of the effective range of the interaction potential, $R_{\rm int} \ll \rho \ll 1/q$, the energy of the incoming wave can be neglected, and the scattered wave is given by the $q \to 0$ solution of the Scrödinger equation,

$$\psi^{\rm 2D}(\boldsymbol{\rho}) \propto \log(\rho/d),$$

exhibiting a logarithmic singularity that is characteristic to two-dimensional scattering, with the length scale $d > 0$ determined by the exact form of the interaction potential. Comparing this with the large distance limit of the wave function $\psi^{\rm 2D}$, we can determine the scattering amplitudes as

$$f^{\rm 2D}(\epsilon) = -\frac{4\pi}{\log(\epsilon_+/E_B^{\rm 2D})} = -\frac{4\pi}{\log(|\epsilon/E_B^{\rm 2D}|) + i\pi\Theta(\epsilon)}, \tag{3.1}$$

characterized by the binding energy, $E_B^{\rm 2D} = -\hbar^2/(md^2) < 0$, that determines the characteristic energy scale of the scattering process, whereas $\Theta(\epsilon)$ denotes the Heaviside function, that originates from the analytic cut of the logarithm at positive energies. The correct analytic form of the scattering amplitude along the branch cut is determined by the infinitesimal imaginary part of the incoming energy, $\epsilon_+ = \epsilon + i0^+$.

[1] The $1/\sqrt{8\pi q}$ normalizing factor has been introduced for later convenience.

At the binding energy $\epsilon = E_B^{2D} < 0$, the denominator of Eq. (3.1) vanishes, and the scattering amplitude exhibits a pole, corresponding to a bound molecular state [39, 65]. Indeed, the wave function of this bound state can be obtained simply by solving the free Schrödinger equation at the binding energy, leading to

$$\psi_B^{2D} \propto K_0\left(\sqrt{\frac{m}{\hbar^2}E_B^{2D} + i0^+}\cdot\rho\right),$$

with K_0 denoting the modified Bessel function [2]. Furthermore, the logarithmic structure of the scattering amplitude Eq. (3.1) also implies the emergence of a logarithmically broad resonance at positive energies, $\epsilon = |E_B^{2D}|$, which is characteristic to two-dimensional scattering.

In the limit of low energy collisions, $\epsilon \ll |E_B^{2D}|$, the imaginary part of the denominator in Eq. (3.1) is negligible, and the scattering amplitude becomes real and *positive* at all energies. Since the scattering amplitude $f^{2D}(\epsilon)$ can be viewed as the effective interaction between the colliding atoms, a dilute Bose of Fermi gas can characterized by an effective mean-field coupling constant $g_{\rm eff}^{2D}$, that is proportional to the thermal average of the scattering amplitudes at its temperature T [65],

$$g_{\rm eff}^{2D} \propto f^{2D}(\epsilon \approx k_B T).$$

We thus see that at small temperatures $k_B T \ll E_B^{2D}$, the interaction in a dilute, purely two-dimensional gas is always repulsive, an artefact of the two dimensional geometry.[3]

3.2 Two-particle scattering in bilayer gases

Let us now turn to the real experimental situation, where the ultracold gas is confined into quasi-two dimensions using harmonic confinement. As has been shown in the seminal works of Refs. [63–65] studying single layer systems, confinement radically modifies interactions as compared to the three-dimensional case, and the scattering properties of the confined system resemble in many respect to those of an exactly two-dimensional gas; in particular, confinement leads to the emergence of a bound molecular state of energy $\epsilon = -E_B$ for *all* values of the three-dimensional scattering length, a, in sharp contrast to three-dimensional gases, where bound states are only present in case of repulsive gases, $a > 0$ (see Section 2.6). Due to the two-dimensional nature of low energy scattering, we also find a logarithmically broad scattering resonance at positive collision energies approximately at $\epsilon \sim |E_B|$, leading to a repulsive interaction of low energy particles, as shown in the previous section.

[2] The modified Bessel function K_0 is related to the more customarily used Hankel functions, $H_0^{(1)}$, as $K_0(x) = \frac{i\pi}{2} H_0^{(1)}(x)$, for $-\pi < Arg(x) \leq \pi/2$.

[3] Similarly, in case of a weakly interacting quantum degenerate Bose gas, the mean-field interaction energy is dominated by two-particle interactions at the energy of relative motion $\epsilon = 2\mu$, where μ is the chemical potential [65]. In this case, the mean-field coupling constant for the purely two-dimensional condensate can be approximated given by $g_{\rm eff}^{2D} \propto f^{2D}(2\mu)$.

The case of two component gases, confined into a bilayer geometry, is even more complex, and exhibits a number of counter-intuitive quantum effects. We will discuss this setting in the rest of this chapter.[4] To be specific, we shall consider atoms of two hyperfine species, $\alpha = \uparrow, \downarrow$, confined into quasi-two dimensions that provides parabolic confinement in the z spatial direction. Due to their different magnetic moments, the components can be separated by the application of a perpendicular magnetic field gradient, thus forming a bilayer geometry. In this setup, the distance $d_{\uparrow\downarrow}$ of the layers, and thus the overlap of the clouds, can be varied at ease by tuning the strength of the magnetic field gradient, as depicted in Fig. 3.1 (a). This additional freedom provides flexible means of tuning interspecies interactions, through the use of interaction resonances, as we show below. To outline the basic mechanisms behind these geometric Feshbach resonances, we shall study the scattering of two particles on each other, and determine the two-particle scattering states analytically.

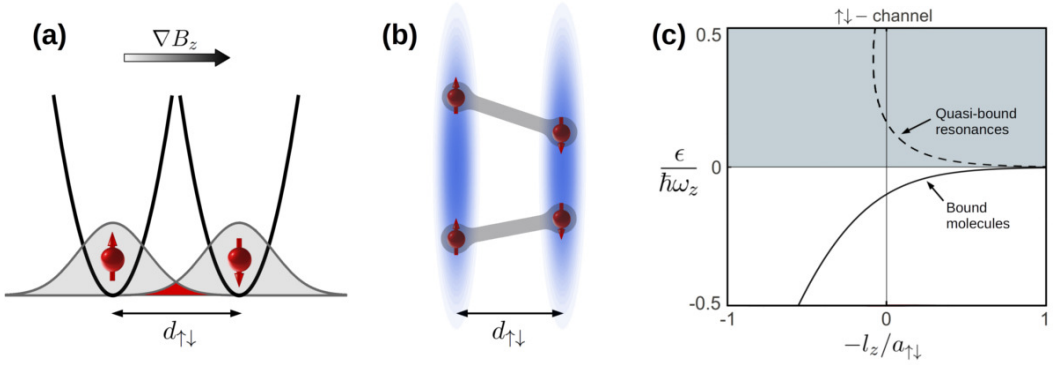

Figure 3.1: (**a**) Experimental setup. A two-component gas is confined into a plane using a deep optical lattice potential in the z direction. Due to their different magnetic moments, the components can be separated into a bilayer structure by the application of a perpendicular magnetic field gradient. (**b**) Schematic picture of the two ultracold clouds with opposite spin. The confining potential fosters the emergence of bound and quasi-bound molecular states, extending over both clouds simultaneously, that can lead to resonances in the interspecies interactions. (**c**) Energy of the bound molecule (solid line) between atoms of opposite spin, in terms of the scattering length $a_{\uparrow\downarrow}$, in the vicinity of a three-dimensional Feshbach resonance. The corresponding quasi-bound molecules (dashed line) at positive energies, are unstable to decaying into the two-particle continuum, and create finite-width resonances in the interparticle interaction. The binding energies, measured in terms of the oscillator energy $\hbar\omega_z$, depend only on the dimensionless ratio of the scattering length to the oscillator length, $l_z = \sqrt{\hbar/m\omega_z}$.

Assuming parabolic confinement, the motion of individual particles in layer α

[4]Single layer gases can be considered a special case of this setting.

can be described by the single particle Hamiltonian[5]

$$\mathcal{H}_\alpha = \frac{\mathbf{p}^2}{2m} + \frac{m\,\omega_z^2}{2}\, z_\alpha^2\,, \tag{3.2}$$

where the z coordinates $z_\alpha \equiv z - z_\alpha^0$ are measured from the centers of the layers, z_α^0, and the layer separation is given by[6] $d_{\uparrow\downarrow} \equiv z_\downarrow^0 - z_\uparrow^0$. Individual particle states in the two layers can then be classified by their momentum $\mathbf{q}_\alpha$ within the (x, y) plane and a harmonic oscillator quantum number n_α, referring to their motion along the z direction. The particles interact through the short-ranged interaction potential $V_{\alpha\beta}$ characterized by the three-dimensional s-wave scattering lengths $a_{\uparrow\uparrow}$, $a_{\uparrow\downarrow}$ and $a_{\downarrow\downarrow}$.[7] Due to the Pauli principle, identical fermionic atoms are non-interacting in the s-wave channel, and thus $a_{\uparrow\uparrow} = a_{\downarrow\downarrow} = 0$, whereas bosons generally have non-zero scattering lengths between all species [39]. With this restriction, our discussion of two-particle scattering applies both for Bose and Fermi particles.

The scattering process of particles in layers α and β, governed by the Hamiltonian $\mathcal{H}_{\alpha\beta} = \mathcal{H}_\alpha + \mathcal{H}_\beta + V_{\alpha\beta}$, can be vastly simplified by transforming into relative and center of mass coordinates,

$$\begin{aligned} \mathrm{z} &\equiv z_\alpha - z_\beta, & \boldsymbol{\rho} &\equiv \boldsymbol{\rho}_\alpha - \boldsymbol{\rho}_\beta, \\ \mathrm{Z} &\equiv \tfrac{z_\alpha + z_\beta}{2}, & \mathbf{R} &\equiv \frac{\boldsymbol{\rho}_\alpha + \boldsymbol{\rho}_\beta}{2}, \end{aligned}$$

where $\boldsymbol{\rho}_\alpha$ denotes the in-plane coordinates in layer α, in the laboratory frame. Due to parabolic confinement, and since the interaction depends only on the relative coordinates, the center of mass and relative motions decouple completely. Indeed, the two-particle Hamiltonian takes on the simple form, $\mathcal{H}_{\alpha\beta} = \mathcal{H}_{\mathrm{rel}} + \mathcal{H}_{\mathrm{COM}}$, with the Hamiltonians of the relative and center of mass motion defined as[8]

$$\begin{aligned} \mathcal{H}_{\mathrm{rel}} &= \frac{\mathbf{p}_{\boldsymbol{\rho}}^2 + p_{\mathrm{z}}^2}{m} + \frac{m\omega_z^2}{4}\,\mathrm{z}^2 + V_{\alpha\beta}(\boldsymbol{\rho},\, \mathrm{z} - d_{\alpha\beta}), \\ \mathcal{H}_{\mathrm{COM}} &= \frac{\mathbf{p}_{\mathbf{R}}^2 + p_{\mathrm{Z}}^2}{4\,m} + m\omega_z^2\,\mathrm{Z}^2. \end{aligned}$$

[5] We neglect the trapping potential in the (x, y) plane that is usually of several orders of magnitude smaller energy than the transverse trapping.

[6] For identical species, the separation is, of course, zero, $d_{\uparrow\uparrow} = d_{\downarrow\downarrow} = 0$.

[7] Treating the interaction as point-like – i.e. neglecting its spatial structure and characterizing it only through its s-wave scattering length – is justified, whenever the trapping potential is approximately constant within the effective range of interactions, R_{int} [39,65]. Then, R_{int} is required to be small compared to the oscillator length, $l_z \equiv \sqrt{\hbar/(m\omega_z)}$. Furthermore, the layer separation is also restricted to the range $d_{\uparrow\downarrow} \ll l_z^2/R_{\mathrm{int}}$ in order that the change of the potential be small to quadratic order. Since $R_{\mathrm{int}} \sim 1 - 10\,\mathrm{nm}$ for most atoms [24, 65], these requirements are very well satisfied in standard experiments. For standard trapping frequencies $1 - 100\,\mathrm{kHz}$, our approximations are valid up to rather large layer separations, $d_{\uparrow\downarrow}/l_z \sim 3 - 10$ (depending also on the atomic species used). For the treatment of extremely strong trapping frequencies where the oscillator length is on the order of R_{int}, see Refs. [74] and [75].

[8] Shifting the z coordinate also shifts the argument of the interaction in the z direction $\delta(z - z') = \delta(z_\alpha - z_{\alpha'} - d_{\alpha\alpha'})$.

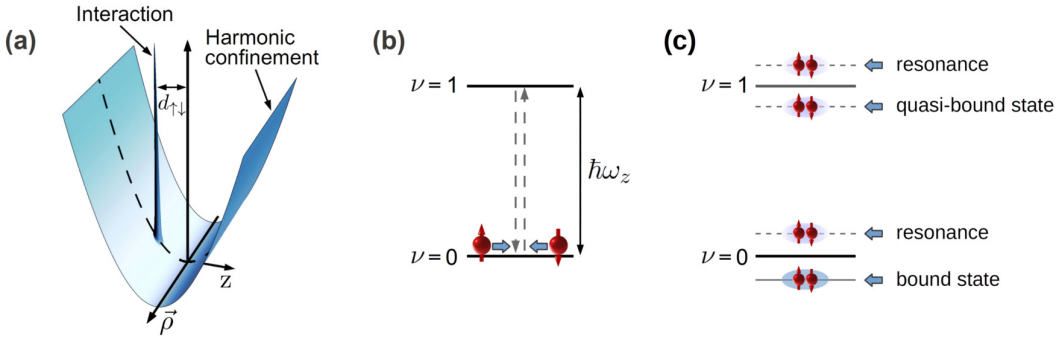

Figure 3.2: (**a**) Harmonic trapping potential and interaction potential between particles of opposite spin, governing the scattering problem in relative coordinates. (**b**) Interaction between the colliding particles creates real and virtual transitions to other relative harmonic oscillator channels ν, creating logarithmically broad scattering resonances around the edges of the channels, $\epsilon \sim \nu\hbar\omega_z$. (**c**) In case of negative scattering lengths, these resonances lead, at positive energies, to the emergence of pairs of quasi-bound molecular states (dashed levels), below each harmonic oscillator edge, as well as to the emergence of a bound state (solid level) at negative energy $\epsilon < 0$. Furthermore, due to the logarithmic nature of the scattering amplitudes, we also find the corresponding scattering resonances (dashed levels) above the edge of each harmonic oscillator channel.

Whereas $\mathcal{H}_{\rm COM}$ describes trivial harmonic motion, $\mathcal{H}_{\rm rel}$ contains the full interaction term $V_{\alpha\beta}$, and describes a particle of reduced mass $m/2$, confined into quasi-two dimensions by a parabolic potential, and scattered by the interaction potential shown in Fig. 3.2 (a). In the absence of interactions the two particles' wave function in the z direction can be expressed in terms of $\tilde{\Psi} \sim \varphi_N(\sqrt{2}\mathrm{Z}/l_z)\,\varphi_\nu\left(\mathrm{Z}/(\sqrt{2}l_z)\right)$, where φ_n denotes the usual harmonic oscillator wave functions,[9] with the natural length scale given by the oscillator length $l_z \equiv \sqrt{\hbar/(m\omega_z)}$, and N and ν are the center of mass and relative harmonic oscillator quantum numbers, respectively. Even if interactions are turned on, the scattering process mixes only the relative transverse channels, whereas the center of mass motion, being trivial, merely shifts the energy of the particles by an energy $E_{\rm COM} = \mathbf{Q}^2/4m + N\hbar\omega_z$, with the center of mass momentum $\mathbf{Q} = \mathbf{q}_\alpha + \mathbf{q}_\beta$. Thus, the two-particle eigenstates can still be decoupled in the form

$$\tilde{\Psi} \sim \varphi_N(\sqrt{2}\mathrm{Z}/l_z)\, e^{i\mathbf{QR}} \cdot \Psi_{\rm rel}(\boldsymbol{\rho},\, \mathrm{z}),$$

where $\Psi_{\rm rel}$ stands for the eigenstates of the Hamiltonian $\mathcal{H}_{\rm rel}$.

Since the center of mass motion of the atoms decouples, we can focus on their non-trivial relative motion by going into the center of mass frame. Let us thus consider a particle pair of opposite incoming momenta $\pm\mathbf{q}$ in the relative harmonic oscillator channel ν. Their interactions can then create transitions to other relative

[9] $\varphi_n(x) = e^{-x^2/2} H_n(x)/\sqrt{2^n\, n!\, \sqrt{\pi}}$, where H_n denotes the n-th Hermite polynomial.

harmonic oscillator channels $\nu \to \nu'$, at the cost of their kinetic energy. Note therefore that only those channels are 'open' to these scattering events, whose harmonic oscillator energy $\nu' \hbar\omega_z$ is less than that of the incoming energy $\epsilon = \hbar^2\mathbf{q}^2/m + \nu\,\hbar\omega_z$. These scattering processes are characterized by the two-dimensional scattering amplitudes, $f^{\nu\nu'}_{\alpha\beta}$, describing the large distance ($\rho \gg l_z$) behavior of the scattering states $\Psi^{\nu\epsilon}_{\alpha\beta}$ of the relative Hamiltonian [65],

$$\Psi^{\nu,\epsilon}_{\alpha\beta}(\mathbf{r}) \simeq \phi_\nu(\mathrm{z})e^{i\mathbf{q}\boldsymbol{\rho}} - \sum_{\nu'} f^{\nu\nu'}_{\alpha\beta}(\epsilon)\sqrt{\frac{i}{8\pi q_{\nu'}\rho}}\, e^{iq_{\nu'}\rho}\phi_{\nu'}(\mathrm{z}), \tag{3.3}$$

where $q_{\nu'} = \sqrt{m\,(\epsilon_+ - \nu'\hbar\omega_z)}/\hbar$ denotes the momenta in the outgoing channels, and $\phi_\nu(\mathrm{z})$ stands for the relative harmonic oscillator wave function $\phi_\nu(\mathrm{z}) = \varphi_\nu(\mathrm{z}/\sqrt{2})/(\sqrt{2}\,l_z)^{1/2}$. Besides the incoming energy, ϵ, the scattering amplitudes are determined by the three-dimensional scattering lengths, $a_{\alpha\beta}$, as well as by the layer separation. However, due to the natural energy and length scales imposed by the trapping frequency and the oscillator length, they depend only on the dimensionless, geometrically tunable ratios $\epsilon/\hbar\omega_z$, $d_{\alpha\beta}/l_z$ and $a_{\alpha\beta}/l_z$, as shown later in this section.

In order to calculate the scattering amplitudes, we determine analytically the two-particle scattering states, classified according to their incoming energy and transverse harmonic channel, ϵ and ν. We first rewrite the scattering problem determined by $\mathcal{H}_{\mathrm{rel}}$ in the self-consistent Lippmann–Schwinger form,

$$\Psi^{\nu,\epsilon}_{\alpha\beta}(\mathbf{r}) = \phi_\nu(\mathrm{z})e^{i\mathbf{q}\boldsymbol{\rho}} - \frac{m}{\hbar^2}\int d^3r'\, G^{(0)}_\epsilon(\mathbf{r},\mathbf{r}')V_{\alpha\beta}(\mathbf{r}')\Psi^{\nu,\epsilon}_{\alpha\beta}(\mathbf{r}'), \tag{3.4}$$

with the second term on the right hand side describing the scattered part of the wave function. Here $\mathbf{r} = (\boldsymbol{\rho}, \mathrm{z})$, and $G^{(0)}_\epsilon$ is the retarded Green's function of the confined system, satisfying $(\mathcal{H}_{\mathrm{rel}}(\mathbf{r}) - V_{\alpha\beta}(\mathbf{r}) - \epsilon)\, G^{(0)}_\epsilon(\mathbf{r},\mathbf{r}') = -\delta^{(3)}(\mathbf{r}-\mathbf{r}')$, and expressed through the modified Bessel functions K_0, as

$$G^{(0)}_\epsilon(\mathbf{r},\mathbf{r}') = \sum_{\nu=0}^{\infty}\phi_\nu(\mathrm{z})\phi_\nu(\mathrm{z}')\frac{K_0(-iq_\nu|\boldsymbol{\rho}-\boldsymbol{\rho}'|)}{2\pi}. \tag{3.5}$$

Since the interaction potential is concentrated to a single point, the integral in Eq. (3.4) can be determined exactly, and the scattered wave becomes

$$\delta\Psi^{\nu,\epsilon}_{\alpha\beta}(\mathbf{r}) = A^{\nu,\epsilon}_{\alpha\beta}\, G^{(0)}_\epsilon(\mathbf{r}, d_{\alpha\beta}\,\hat{\mathbf{z}}),$$

with an unknown proportionality constant, to be determined later from the short distance asymptotics of the scattering state. Thus, the retarded propagator describes the overall behavior of the two-particle scattering states outside the range of the interaction potential. At short distances around the point of interaction, $\delta r = |\mathbf{r} - d_{\alpha\beta}\,\hat{\mathbf{z}}| \ll l_z$, the relative propagation of the particles is not influenced by the axial confinement, and $G^{(0)}_\epsilon$ exhibits the well-known $1/\delta r$ singularity of three-dimensional free propagator in Eq. (2.3),

$$G^{(0)}_\epsilon(\mathbf{r}, d_{\alpha\beta}\hat{\mathbf{z}}) \simeq \frac{1}{4\pi}\left(\frac{1}{\delta r} + \frac{w_{\alpha\beta}(\epsilon/\hbar\omega_z)}{\sqrt{2\pi}l_z} + \dots\right), \tag{3.6}$$

together with an energy and separation dependent constant, $w_{\alpha\beta}(\epsilon/\hbar\omega_z)$ [65]. Whereas the singular term in the propagator originates from the locally three-dimensional geometry, $w_{\alpha\beta}$ accounts for the confinement effects, and, as we show below, it determines the position and the strength of the interaction resonances in the scattering amplitudes. The rather technical derivation of this important constant is given in Appendix A.1, and leads to

$$w_{\alpha\beta}(\epsilon/\hbar\omega_z) = \lim_{\bar{\nu}\to\infty}\left[c_{\bar{\nu}} - \sum_{\nu'=0}^{2\bar{\nu}-1}\sqrt{2\pi}l_z\,\phi^2_{\nu'}(d_{\alpha\beta})\log\left(\frac{\nu'\hbar\omega_z-\epsilon_+}{2\hbar\omega_z}\right)\right], \tag{3.7}$$

with $c_\nu \equiv 2\sqrt{\frac{\nu}{\pi}}\log\frac{\nu}{e^2}$. Notice that $w_{\alpha\beta}$ only depends on the dimensionless ratios $\epsilon/(\hbar\omega_z)$ and $d_{\alpha\beta}/l_z$. The logarithmic terms here incorporate the effects of virtual transitions to other harmonic oscillator channels throughout the scattering process (see Fig. 3.2 (b)), whereas the prefactors $\phi^2_\nu(d_{\alpha\beta})$ appear since the two particles must stay at the same position to interact through the potential in Fig. 3.2 (a). Thus the scattering amplitude in the $\uparrow\downarrow$-channel depends sensitively on the layer separation $d_{\uparrow\downarrow}$ through these prefactors.

The amplitude of the scattered wave can now be easily determined by observing that at short distances $\delta r \ll l_z$, the trapping potential does not modify the form of the scattered wave. Therefore, beyond the effective range of the interaction potential[10] the scattering state must have the same asymptotics as in three dimensions[11]

$$\Psi^{\rm 3D}_{\alpha\beta} \sim 1 - \frac{a_{\alpha\beta}}{\delta r} + \mathcal{O}(\delta r). \tag{3.8}$$

By comparing the asymptotic forms in Eqs. (3.6) and (3.8), we can determine the amplitude $A^{\nu,\epsilon}_{\alpha\beta}$ at ease, and obtain the *exact* form of the two-particle scattering states

$$\Psi^{\nu,\epsilon}_{\alpha\beta}(\mathbf{r}) = e^{i\mathbf{q}\boldsymbol{\rho}}\phi_\nu(\mathrm{z}) - \frac{4\pi\, a_{\alpha\beta}\,\phi_\nu(d_{\alpha\beta})}{1+\frac{a_{\alpha\beta}}{\sqrt{2\pi}\,l_z}\,w_{\alpha\beta}(\epsilon/\hbar\omega_z)}\,G^{(0)}_\epsilon(\mathbf{r},d_{\alpha\beta}). \tag{3.9}$$

3.2.1 Scattering amplitudes and molecular bound states

The analytic form of the scattering states entirely describes the two-particle scattering process. Most importantly, by investigating their large distance behavior,[12] $\rho \gg l_z$, and comparing it with the usual asymptotic expansion of the scattering states in Eq. (3.3), we can determine the scattering amplitudes in the open channels, $\epsilon > \nu'\hbar\omega_z$,

$$f^{\nu\nu'}_{\alpha\beta}(\epsilon) = \frac{4\pi a_{\alpha\beta}\,\phi_\nu(d_{\alpha\beta})\phi_{\nu'}(d_{\alpha\beta})}{1+\frac{a_{\alpha\beta}}{\sqrt{2\pi}\,l_z}\,w_{\alpha\beta}(\epsilon/\hbar\omega_z)} \tag{3.10}$$

[10] A few tens of the Bohr radius for most atoms [65].

[11] At short distances $\delta r \ll 1/q$, the form of the three-dimensional scattered wave is not influenced by the incoming energy, and thus all such states take on the same asymptotic form as of the bound state in Eq. (2.4).

[12] The long distance behavior of the propagator $G^{(0)}_\epsilon$ can be inferred from Eq. (3.5), by making use of the $x \gg 1$ limit of the modified Bessel functions, $K_0(-ix)/(2\pi) \sim \Theta(x^2)\,\exp(ix)/\sqrt{-8\pi i\, x}$. Here, Θ denotes the Heaviside function.

characterizing the interactions of a dilute ultracold gas. The nominator of this expression reflects the naive expectation that, to leading order, the scattering amplitudes shall be proportional to the first order matrix element of the interaction with harmonic oscillator eigenstates of the incoming and outgoing channels.

Throughout their propagation, however, the particles go through several virtual transitions to higher harmonic oscillator levels that can have significant effect on the scattering amplitudes, especially in the vicinity of the energy threshold of these energy levels, $\epsilon \sim \hat{\nu}\hbar\omega_z$, where the particles can resonantly couple to the given channel $\hat{\nu}$. These virtual processes are incorporated in the denominator by the $w_{\alpha\beta}$ function, and appear as logarithmic peaks, shown in Eq. (3.7). Importantly, these processes can give rise to interaction resonances, whenever the real part of the denominator in Eq. (3.10) becomes zero. The energy and width (i.e. the lifetime) of these resonances are determined by the function $w_{\alpha\beta}$. Since in the $\uparrow\downarrow$-channel, $f_{\uparrow\downarrow}$ depends sensitively on the layer separation through the relative harmonic wave functions $\phi_\nu^2(d_{\uparrow\downarrow})$ in Eq. (3.7), the position and width of these resonances can be tuned at wish, and, at appropriate separations, the gas can even be made strongly interacting.

At negative energies, the scattering amplitudes exhibit a pole, corresponding to molecular bound states at a binding energy $\epsilon = E^B_{\alpha\beta} < 0$ [39,41], for *all* values of the three-dimensional scattering lengths $a_{\alpha\beta}$. Indeed, at small energies $\epsilon/\hbar\omega_z \simeq 0$, the virtual processes in the $\nu = 0$ channel give rise to a logarithmic singularity in $w_{\alpha\beta}$ that takes on the form $w_{\alpha\beta} \sim \sqrt{2\pi} l_z\, \phi_0^2(d_{\alpha\beta}) \left(-\log\left|\frac{\epsilon}{\hbar\omega_z}\right| + i\pi\Theta(x)\right) + \gamma_{\alpha\beta}$. Here, the separation dependent prefactor, $\gamma_{\alpha\beta}$, of order 1, originates from the contributions of $\nu \neq 0$ channels. Thus, at low energies the scattering amplitude takes on the simple logarithmic form

$$f^{00}_{\alpha\beta}(\epsilon) \simeq \frac{4\pi}{\log(\epsilon_+/E^B_{\alpha\beta})}, \tag{3.11}$$

characteristic to the scattering amplitudes of an exactly two-dimensional system. As we discussed in the previous section, this logarithmic form necessarily leads to the emergence of a bound state, whose energy is determined by the scattering lengths and layer separations. In particular, for small negative scattering lengths, $a_{\alpha\beta} < 0$, the bound state energy shows a non-analytic, exponential dependence on these parameters

$$E^B_{\alpha\beta} \propto -\hbar\,\omega_z\; e^{-1/\left(|a_{\alpha\beta}|\phi_0^2(d_{\alpha\beta})\right)}. \tag{3.12}$$

The appearance of these bound states on the attractive side of the three-dimensional Feshbach resonance is specific to two-dimensional scattering [65]. The (relative) wave function of the bound molecule can be easily obtained by solving the Schrödinger equation $\mathcal{H}_{\rm rel}\,\Psi^B_{\alpha\beta} = E^B_{\alpha\beta}\,\Psi^B_{\alpha\beta}$, leading to the simple form

$$\Psi^B_{\alpha\beta}(\mathbf{r}) = G^{(0)}_{E^B_{\alpha\beta}}(\mathbf{r},\, d_{\alpha\beta}\hat{\mathbf{z}})$$

The bound states are visualized in Fig. 3.3, showing the bound state wave function in relative coordinates, as well as their density in the laboratory frame, clearly

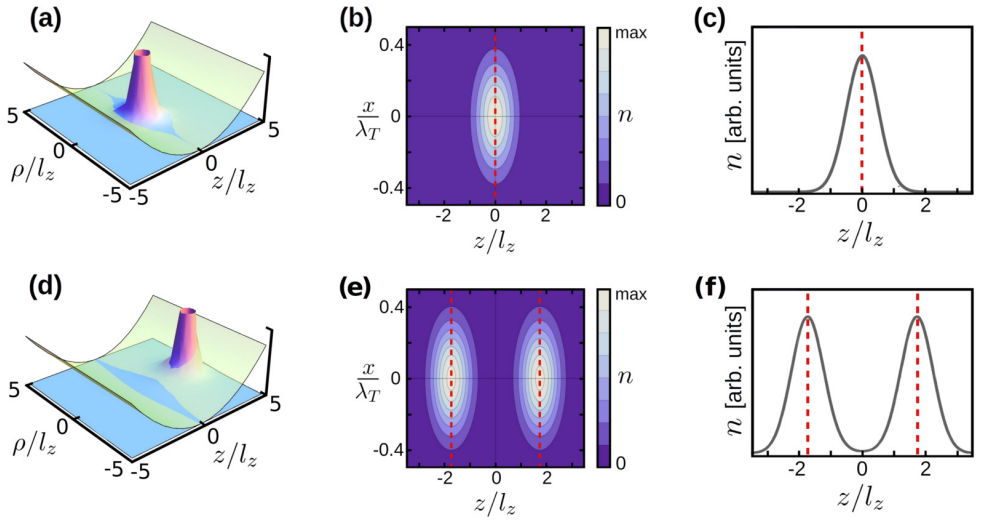

Figure 3.3: Visualization of the intralayer (upper row) and interlayer bound states (lower row) at a separation $d_{\uparrow\downarrow}/l_z = 3.5$. (**a**),(**d**) Bound state wave function $\Psi^B_{\alpha\beta}$, in relative coordinates of the atoms, displaying the well-known $1/(4\pi\,\delta r)$ singularity of unconfined three-dimensional bound states at the point of interaction (see Eq. (2.4)). The harmonic confining potential is also shown. (**b**),(**e**) Real space density $n_{\alpha\beta}(\mathbf{r}) = \int d^3\mathbf{r}'\,\|\tilde{\Psi}_{\alpha\beta}(\mathbf{r},\mathbf{r}')\|^2$ of the two-particle bound state $\tilde{\Psi}_{\alpha\beta}(\mathbf{r},\mathbf{r}')$ in the (x,z) plane of the laboratory frame. In the intralayer channel, the density clearly splits, with only a tiny part of the wave function tunneling through the intermediate region. The center of mass part of the wave function is described by an in-plane thermal Gaussian wave packet at a temperature $k_BT = 0.1\,\hbar\omega_z$. (**c**),(**f**) One dimensional cut of the densities in (**b**) and (**e**), respectively, along the $x = 0$ axis. [Interactions are equal and repulsive, $a_{\uparrow\uparrow} = a_{\uparrow\downarrow} = 0.6\,l_z$, leading to the bound state energies $E^B_{\uparrow\uparrow} = -3.26\,\hbar\omega_z$, $E^B_{\uparrow\downarrow} = -0.22\,\hbar\omega_z$.]

displaying a double-peak feature at non-zero separation, in consistence with our naive expectations.

3.2.2 Interaction resonances and quasi-bound molecules

At positive energies, $\epsilon > 0$, no molecular bound state can exist, as the constituent atoms are free to decay into the two-particle continuum. Mathematically, this is reflected in the fact that $w_{\alpha\beta}$ has a finite imaginary part, thus the scattering amplitudes exhibit finite-width interaction resonances, each time the real part of the denominator in Eq. (3.10) crosses zero. These resonances are attributed to *unstable* quasi-bound molecular states, with decay rates proportional to the imaginary part of $w_{\alpha\beta}$. In physical terms, the interaction resonances between the colliding particles is caused by virtual processes, whereby they form an unstable molecular pair, and then decay into the continuum. At small energies, $\epsilon/\hbar\omega_z \simeq 0$, the simple logarithmic

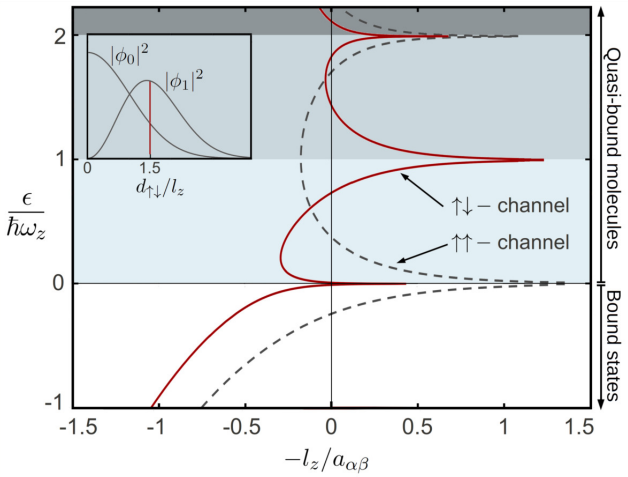

Figure 3.4: Binding energies of molecular states between identical (dashed line) and opposite (full line) spins at a layer separation $d_{\uparrow\downarrow}/l_z = 1.5$, shown in terms of the scattering length $a_{\alpha\beta}$ in the vicinity of a three dimensional Feshbach resonance. The molecules are bound at negative energies, $\epsilon < 0$, whereas the ones at positive energies, $\epsilon > 0$, acquire a finite lifetime through decay processes into the two-particle continuum, and are therefore only quasi-bound. Close to the edge of the $\nu = 1$ channel, novel interspecies quasi-bound states appear that are forbidden due to symmetry for identical species. At even greater layer separations, the energy spectrum is pushed even further towards the positive side of the Feshbach resonance, where novel quasi-bound states appear even at moderate values of $a_{\uparrow\downarrow} > 0$ (see Fig. 3.6 (b)-(e)). The spectrum is plotted at zero center of mass motion ($N = 0$ and $\mathbf{Q} = 0$), whereas for $N \neq 0$ it is shifted by $N\hbar\omega_z$ to higher energies. [Inset: dependence of the harmonic oscillator coefficients $\phi_0^2(d_{\uparrow\downarrow})$ and $\phi_1^2(d_{\uparrow\downarrow})$ on the layer separation, determining the lifetimes of quasi-bound molecules, as well as the exponential dependence of their energies on the scattering lengths close to $\epsilon \sim \nu\hbar\omega_z$.]

form of the scattering amplitudes in Eq. (3.11) gives rise to a logarithmically broad quasi-bound resonance at energies $\epsilon \sim |E^B_{\alpha\beta}| > 0$. At this point, $|f^{00}_{\alpha\beta}|^2$ reaches its maximal possible value, leading to intense scattering in the gas. At higher energies, the scattering amplitude exhibits further resonances, whose energies are displayed in Fig. 3.4 for some typical confinement parameters as a function of $l_z/a_{\alpha\beta}$ in the vicinity of a three-dimensional magnetic Feshbach resonance.[13] Notably, the interlayer scattering (solid line) displays features completely absent in intralayer scattering (dashed line), exhibiting novel quasi-bound molecules close to the $\hbar\omega_z$ edge of the $\nu = 1$ channel, similarly to the one near the $\epsilon \sim 0$ threshold. The emergence of these quasi-bound states can be understood on symmetry grounds as follows: in intralayer scattering, $\nu = 0 \to 1$ transitions are forbidden by reflection symmetry, (and also

[13]Close to the Feshbach resonance, the scattering length approaches infinity (shown in Fig. 2.3), thus the parameter $l_z/a_{\alpha\beta}$ goes to zero.

by Bose statistics in case of bosons), due to the even and odd parity of the ϕ_0 and ϕ_1 states, respectively. Since the colliding particles cannot make virtual transitions to the odd ν channels, the ϕ_ν^2 coefficients of the associated logarithmic singularities in $w_{\alpha\beta}$ are zero for odd values of ν. However, such interlayer processes are allowed once $d_{\uparrow\downarrow} \neq 0$, and they result in the emergence of new quasi-bound molecular states. In the vicinity of the $\hbar\omega_z$ threshold we find two novel quasi-bound molecular states (resonances) for negative scattering lengths, whose energies can be written as

$$E^1_{\uparrow\downarrow} - \hbar\,\omega_z \;\propto\; \pm\hbar\,\omega_z\, e^{-1/\left(|a_{\uparrow\downarrow}|\phi_1^2(d_{\uparrow\downarrow})\right)}, \tag{3.13}$$

when $a_{\uparrow\downarrow} > 0$ is small. Importantly, while the weight and energy of these resonances are determined by $\phi_1^2(d_{\uparrow\downarrow})$, their decay rates are given by $\mathrm{Im}\, w_{\uparrow\downarrow} \propto \phi_0^2(d_{\uparrow\downarrow}) + \Theta(\epsilon - \hbar\omega_z)\phi_1^2(d_{\uparrow\downarrow})$. Notice that the decay rate of the quasi-bound state below the $\hbar\omega_z$ edge is always smaller, since it cannot decay into the $\nu = 1$ channel due to energy conservation. Since the decay rate of this state decreases exponentially with increasing layer separations, $\hat{\Gamma} \propto \phi_0^2(d_{\uparrow\downarrow}) \propto e^{-d^2_{\uparrow\downarrow}/l_z^2}$, one can make the quasi-bound state sharper and sharper by increasing the layer separation – at the cost of somewhat decreasing its weight and binding energy. Similar interlayer quasi-bound states of energy $E^\nu_{\uparrow\downarrow}$ appear close to every threshold, $\epsilon \simeq \nu\hbar\omega_z$, and can turn into narrow resonances as one increases the layer separation $d_{\uparrow\downarrow}$. This increased stability of the quasi-bound molecules opens up a route to detect them in a modulation experiment, as we propose in Sec. 3.5.

The molecular states shown in Fig. 3.4 have zero center of mass momentum. The total energy of two particles is, however, increased by their center of mass motion, $E_{\mathrm{COM}} = N\hbar\omega_z + \mathbf{Q}^2/4m$, and accordingly, the bound state spectrum in Fig. 3.4 gets shifted by an energy $\epsilon \to \epsilon + N\,\hbar\omega_z$, in the $N \neq 0$ channels, corresponding to excited molecular bound states with an oscillating center of mass in the perpendicular direction. Thus, we can find molecular bound states in the $N \neq 0$ channels even at positive total energies.

3.3 Many-body T-matrix

To characterize interactions in a thermal ultracold gas, one needs to go beyond the simple two-particle picture, and consider the effects of the cloud on the interactions as well. In order to account for many-body corrections, let us return to the laboratory frame of the thermal cloud, and describe the gas in terms of the second quantized Hamiltonian, $H = H_{\mathrm{kin}} + H_{\mathrm{int}}$ described by the kinetic and interaction terms

$$H_{\mathrm{kin}} \;=\; \sum_\alpha \int \mathrm{d}^3\mathbf{r}\; \psi^\dagger_\alpha(\mathbf{r})(\mathcal{H}_\alpha(\mathbf{r}) - \mu_\alpha)\psi_\alpha(\mathbf{r}), \tag{3.14}$$

$$H_{\mathrm{int}} \;=\; \sum_{\alpha,\beta} \int \mathrm{d}^3\mathbf{r}\; \frac{g^{\mathrm{3D}}_{\alpha\beta}}{2}\, \psi^\dagger_\alpha(\mathbf{r})\psi^\dagger_\beta(\mathbf{r})\psi_\beta(\mathbf{r})\psi_\alpha(\mathbf{r}). \tag{3.15}$$

Here, the chemical potentials $\mu_\alpha < 0$ set the densities of the gas, and the interaction parameters $g^{\rm 3D}_{\alpha\beta}$ are related to the three-dimensional scattering lengths through appropriate renormalization [76], to be discussed in Appendix A.2. The field operators ψ_α annihilate particles of species α, and obey the commutation (anti-commutation) relations

$$\left[\psi_\alpha(\mathbf{r}), \psi^\dagger_\beta(\mathbf{r}')\right]_\mp = \delta_{\alpha\beta}\,\delta^{(3)}(\mathbf{r}-\mathbf{r}')$$

in case of bosonic (fermionic) atoms. In the confined system, free particles are characterized by their momentum $\mathbf{q}$, their transverse harmonic oscillator channel n and their hyperfine species α. In order to describe particle scattering, we thus separate the motional degrees of freedom in the parallel and perpendicular directions, and expand the fields as

$$\psi_\alpha(\mathbf{r}) = \sum_{n=0}^{\infty} \int \frac{d^2q}{(2\pi)^2} e^{i\mathbf{q}\rho}\,\varphi_n(z-z^0_\alpha)\,a_{\alpha n}(\mathbf{q}). \tag{3.16}$$

In this basis, the kinetic and interaction terms of the Hamiltonian read

$$\begin{aligned} H_{\rm kin} &= \sum_{\alpha=\uparrow,\downarrow}\sum_{n=0}^{\infty}\int \frac{d^2q}{(2\pi)^2}\,\xi_{\alpha n\mathbf{q}}\,a^\dagger_{\alpha n}(\mathbf{q})\,a_{\alpha n}(\mathbf{q}) \\ H_{\rm int} &= \sum_{\alpha,\beta=\uparrow,\downarrow}\sum_{\mathbf{n},\mathbf{n}'}\int \frac{d^2k}{(2\pi)^2}\frac{d^2k'}{(2\pi)^2}\frac{d^2q}{(2\pi)^2} \\ &\quad \frac{t^{\mathbf{nn}'}_{\alpha\beta}}{2}\,a^\dagger_{\alpha n_1}(\mathbf{k}+\mathbf{q})a^\dagger_{\beta n_2}(\mathbf{k}'-\mathbf{q})a_{\beta n'_1}(\mathbf{k}')a_{\alpha n'_2}(\mathbf{k}) \end{aligned} \tag{3.17}$$

where $\xi_{\mathbf{q},n,\alpha} = \frac{q^2}{2m} + n\hbar\omega_z - \mu_\alpha$, denotes the single particle energies measured from the chemical potentials. In Eq. (3.17) we have introduced the bare T-matrix (vertex) of interactions

$$\mathbf{t}^{\mathbf{nn}'}_{\alpha\beta} = g^{\rm 3D}_{\alpha\beta}\,\langle\mathbf{n}|\,\delta^{(1)}(z_1-z_2-d_{\alpha\beta})\,|\mathbf{n}'\rangle$$

defined using the incoming and outgoing harmonic oscillator states of the scattered particles $|\mathbf{n}\rangle = |n_1,n_2\rangle = \varphi_{n_1}(z_1)\,\varphi_{n_2}(z_2)$. This quantity characterizes the bare (first order) interaction between the atoms.

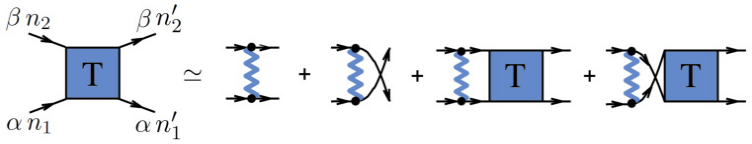

Figure 3.5: Bethe-Salpeter equation determining the many-body T-matrix (interaction vertex) in the ladder diagram approximation in a thermal gas. Full lines indicate bare propagators, whereas dashed lines refer to the bare coupling $g^{\rm 3D}_{\alpha\beta}$. In the vacuum (i.e. in the absence of other gas atoms), the ladder series accounts for all non-zero diagrams, and the T-matrix becomes exact.

In the confined system, however, the particles go through several virtual transitions between the different harmonic oscillator channels, as well as they interact with the thermal cloud throughout their propagation. Thus, in order to sum up these contributions to the two-particle interaction, we determine the *dressed* many-body T-matrix within the "ladder diagram approximation" of Fig. 3.5. The corresponding self-consistent Bethe-Salpeter equation [76, 77], continued to real frequencies, reads

$$\mathbf{T}^{\mathbf{nn}'}_{\alpha\beta}(\Omega,\mathbf{Q}) = \mathbf{t}^{\mathbf{nn}'}_{\alpha\beta} + \sum_{\mathbf{n}''} \mathbf{t}^{\mathbf{nn}''}_{\alpha\beta}\, \Pi^{\mathbf{n}''}_{\alpha\beta}(\Omega,\mathbf{Q})\, \mathbf{T}^{\mathbf{n}''\mathbf{n}'}_{\alpha\beta}(\Omega,\mathbf{Q}) \tag{3.18}$$

with the retarded two-particle propagator (polarization operator) $\Pi^{\mathbf{n}}_{\alpha\beta}$. Although in principle the T-matrix depends on the frequencies (energies) and momenta of all the incoming and outgoing particles,[14] in the ladder diagram approximation it simply becomes the function of the total energy $\hbar\Omega = \hbar\omega_1 + \hbar\omega_2$ and center of mass momentum of incoming particles $\mathbf{Q} = \mathbf{q}_1 + \mathbf{q}_2$. The polarization operator $\Pi^{\mathbf{n}}_{\alpha\beta} = \Pi^{(0),\mathbf{n}}_{\alpha\beta} + \delta\Pi^{\mathrm{th},\mathbf{n}}_{\alpha\beta}$ is given by vacuum contributions, characterizing two-particle scattering in the absence of other gas atoms,

$$\Pi^{(0),\mathbf{n}}_{\alpha\beta} = \int \frac{d^2q}{(2\pi)^2}\, \frac{e^{i\mathbf{q}\boldsymbol{\rho}}}{\left(\hbar\Omega_+ - \frac{\hbar^2Q^2}{4m} + (n_\alpha + n_\beta)\hbar\omega_z\right) - \epsilon(q)}, \tag{3.19}$$

and many-body thermal corrections

$$\delta\Pi^{\mathrm{th},\mathbf{n}}_{\alpha\beta} = \zeta_{\mathrm{B/F}} \int \frac{d^2q}{(2\pi)^2}\, \frac{n_{\mathrm{B/F}}\left(\xi_{\mathbf{q}+\mathbf{Q}/2,n_1,\alpha}\right) + n_{\mathrm{B/F}}\left(\xi_{\mathbf{q}-\mathbf{Q}/2,n_2,\alpha}\right)}{\left(\hbar\Omega_+ - \frac{\hbar^2Q^2}{4m} + (n_\alpha + n_\beta)\hbar\omega_z\right) - \epsilon(q)}, \tag{3.20}$$

where $\Omega_+ = \Omega + i0^+$, and $\epsilon(q) = \hbar^2\mathbf{q}^2/m$ denotes the energy of the particles' relative motion. In the thermal part, $n_{\mathrm{B/F}}$ denotes the Bose/Fermi distribution function, whereas $\zeta_{\mathrm{B/F}} = \pm 1$ for bosons/fermions, respectively. The small auxiliary parameter $\boldsymbol{\rho}$ in the vacuum term provides regularization for the polarization operator at large momenta, and will be taken to zero after the T-matrix is expressed in terms of experimentally measurable scattering lengths $a_{\alpha\beta}$, instead of the bare interaction term $g^{\mathrm{3D}}_{\alpha\beta}$,[15] as we show in Appendix A.2.

3.3.1 Vacuum scattering

In case when many-body corrections are negligible, the Bethe-Salpeter equations characterize the vacuum scattering of particles *exactly*, since the ladder series contains all non-zero diagrams in this case. To find the vacuum T-matrix, $\mathbf{T}^{(0)}$, let us

[14] Up to energy and momentum conservation.

[15] Notice that since we assumed a zero-range interaction potential Eq. (3.15), the Bethe-Salpeter equation is actually singular, and requires a large-momentum cut-off. However, the nature of the energy cut-off is unimportant in terms of low energy scattering, and it shall be safely removable after the T-matrix is expressed in terms of physically measurable quantities.

first rewrite Eq. (3.18) in the matrix form[16]

$$\hat{\mathbf{T}}_{\alpha\beta} = \hat{\mathbf{t}}_{\alpha\beta} + \hat{\mathbf{t}}_{\alpha\beta} \cdot \hat{\Pi}_{\alpha\beta} \cdot \hat{\mathbf{T}}_{\alpha\beta}. \tag{3.21}$$

Facilitating the insights from the previous section, we transform the equation into the basis of center of mass and relative motion of the particles in the transverse direction $|\mathbf{n}\rangle = \sum_{N,\nu} C^{\mathbf{n}}_{N,\nu} |N,\nu\rangle$, with the "Clebsch-Gordan" coefficients arising from the change of basis given by $C^{\mathbf{n}}_{N,\nu} = \langle N,\nu|\mathbf{n}\rangle$. In this basis, matrices in Eq. (3.21) take on the particularly simple form

$$\langle N,\nu|\, \hat{\mathbf{t}}_{\alpha\beta}\, |N',\nu'\rangle = \delta_{NN'}\, g^{\mathrm{3D}}_{\alpha\beta}\, \phi^*_\nu(d_{\alpha\beta})\phi_{\nu'}(d_{\alpha\beta}). \tag{3.22}$$

$$\langle N,\nu|\, \hat{\Pi}^{(0)}_{\alpha\beta}\, |N',\nu'\rangle = \delta_{NN'}\, \delta_{\nu\nu'}\, \Pi^{(0);\,N\nu}_{\alpha\beta} \tag{3.23}$$

$$\langle N,\nu|\, \hat{\mathbf{T}}_{\alpha\beta}\, |N',\nu'\rangle = \mathbf{T}^{NN';\nu\nu'}_{\alpha\beta} \tag{3.24}$$

Furthermore, energy conservation requires that the Clebsch-Gordan coefficients be zero unless $n_1 + n_2 = N + \nu$. Since the vacuum polarization operator in Eq. (3.19) depends on the total harmonic oscillator energy $(n_1 + n_2)\hbar\omega_z$, the center of mass energy $E_{\mathrm{COM}} = \hbar^2 Q^2/(4m) + N\hbar\omega_z$ can be completely separated from that of the relative motion, and the polarization can be written as[17]

$$\Pi^{(0);\,N\nu}_{\alpha\beta}(\Omega, \mathbf{Q}) = \Pi^{(0)}(\Omega - \nu\omega_z - E_{\mathrm{COM}}/\hbar). \tag{3.25}$$

The structure of the matrix elements in Eqs. (3.22, 3.23) suggest that the T-matrix can be also found by decoupling the center of mass and relative quantum numbers [76]. Indeed, we find that it can be cast into the simple form

$$\mathbf{T}^{(0);NN',\nu\nu'}_{\alpha\beta}(\Omega, \mathbf{Q}) = \sqrt{2\pi} l_z\, \delta_{NN'}\, \phi^*_\nu(d_{\alpha\beta})\phi_{\nu'}(d_{\alpha\beta})\, \mathcal{T}^{(0)}(\Omega - E_{\mathrm{COM}}/\hbar), \tag{3.26}$$

with the auxiliary function

$$\mathcal{T}^{(0)}(\Omega) = \frac{1}{\sqrt{2\pi} l_z}\, \frac{1}{\frac{1}{g^{\mathrm{3D}}_{\alpha\beta}} - \sum_{\nu=0}^{\infty} \phi^2_\nu(d_{\alpha\beta})\, \Pi^{(0)}\,(\Omega - \nu\omega_z)}. \tag{3.27}$$

Thus, in accordance with our expectations, since the interaction potential only depends on the relative position of the particles, the center of mass motion plays no role in two-particle scattering, and E_{COM} merely shifts the total energy of colliding particles. Furthermore, after appropriate renormalization of the bare interaction term $g^{\mathrm{3D}}_{\alpha\beta}$, presented in Appendix A.2, we can see that the vacuum T-matrix is proportional to the scattering amplitudes Eq. (3.10)

$$\mathbf{T}^{(0);\,NN',\nu\nu'}_{\alpha\beta}(\Omega, \mathbf{Q}) = \delta_{NN'} \frac{\hbar^2}{m}\, f^{\nu\nu'}_{\alpha\beta}\,(\hbar\Omega - E_{\mathrm{COM}}). \tag{3.28}$$

[16] The matrices are defined such that they give the appropriate matrix elements with the incoming and outgoing fields, i.e. $\langle \mathbf{n}|\, \hat{\Pi}_{\alpha\beta}\, |\mathbf{n}'\rangle = \delta_{\mathbf{nn}'}\, \Pi^{\mathbf{n}}_{\alpha\beta}$, $\langle \mathbf{n}|\, \hat{\mathbf{T}}_{\alpha\beta}\, |\mathbf{n}'\rangle = \mathbf{T}^{\mathbf{nn}'}_{\alpha\beta}$, and $\langle \mathbf{n}|\, \hat{\mathbf{t}}_{\alpha\beta}\, |\mathbf{n}'\rangle = \mathbf{t}^{\mathbf{nn}'}_{\alpha\beta}$.

[17] If we consider $\boldsymbol{\rho}$ formally as the relative coordinate between the scattered atoms, we find that $\Pi^{(0)}$ is given by the two-dimensional retarded Green's function of their relative motion, $\Pi^{(0)}(\Omega) = \int \frac{d^2q}{(2\pi)^2} \frac{e^{i\mathbf{q}\boldsymbol{\rho}}}{\hbar\Omega_+ - \epsilon(q)} = -\frac{m}{2\pi\hbar^2} K_0\left(-i\, \frac{\rho}{l_z} \sqrt{\frac{\Omega}{\omega_z}}\right)$.

3.3.2 Thermal corrections

The interaction effects between the thermal gas and the colliding particles are taken into account by the many-body corrections to the polarization operator $\delta\Pi^{\rm th}_{\alpha\beta}$. Due to these interactions with other atoms, the center of mass motion of the particles will not decouple completely from the scattering process, and the solution of the Bethe-Salpeter equation requires a more general treatment [76]. However, in a strongly confined thermal gas ($|\mu|, k_BT \ll \hbar\omega_z$), where the $n \neq 0$ levels are essentially unpopulated, the thermal correction $\delta\Pi^{{\rm th},N\nu}_{\alpha\beta}$ takes on non-zero values only in the $N = \nu = 0$ channel. Therefore, similarly to the case of vacuum scattering, the Bethe-Salpeter equations conserve the center of mass oscillator quantum number N, and the T-matrix becomes diagonal in this index $\mathbf{T}^{NN';\nu,\nu'}_{\alpha\beta} \simeq \delta_{NN'}\mathbf{T}^{N;\nu,\nu'}_{\alpha\beta}$. Through a straightforward calculation, similar to the one in the vacuum case, it can be shown to take on the simple form

$$\mathbf{T}^{N;\nu,\nu'}_{\alpha\beta}(\Omega,\mathbf{Q}) \approx \frac{\hbar^2}{m}\,\frac{4\pi a_{\alpha\beta}\,\phi^*_\nu(d_{\alpha\beta})\phi_{\nu'}(d_{\alpha\beta})}{1+\frac{a_{\alpha\beta}}{\sqrt{2\pi}l_z}\mathcal{W}^N_{\alpha\beta}(\Omega,\mathbf{Q})}, \tag{3.29}$$

with the many-body counterpart $\mathcal{W}^N_{\alpha\beta}$ of the function $w_{\alpha\beta}$, also accounting for thermal corrections in the $N = 0$ channel,

$$\mathcal{W}^N_{\alpha\beta}(\Omega,\mathbf{Q}) = w_{\alpha\beta}\left(\frac{\hbar\Omega - E_{\rm COM}}{\hbar\omega_z}\right) + \delta_{N0}\,\delta w^{\rm th}_{\alpha\beta}(\Omega,\mathbf{Q}).$$

The second term in $\mathcal{W}$ accounts for many-body interactions with the thermal condensate,

$$\delta w^{\rm th}_{\alpha\beta}(\Omega,\mathbf{Q}) = -\frac{4\pi\hbar^2}{m}\,\sqrt{2\pi}l_z|\phi_0(d_{\alpha\beta})|^2\,\delta\Pi^{{\rm th},00}_{\alpha\beta}(\Omega,\mathbf{Q}),$$

and it is proportional to the density (see Eq. (3.20)). One can show, however, that in case of a strongly confined dilute Bose or Fermi gas, the many-body corrections captured in $\delta w^{\rm th}_{\alpha\beta}$ are numerically small as compared to the quantum effects in $w_{\alpha\beta}$, and they mostly lead to screening.[18]

3.4 Geometric tuning of interactions

We have seen in Eq. (3.28), how the scattering amplitudes in a confined gas characterize the two-particle interaction vertex, determining the energy of interactions. In this section, we show how resonances in the scattering amplitude can be exploited to tune a strongly confined gas into the strongly interacting regime. Indeed, mean-field interactions of a strongly confined thermal or quantum degenerate gas[19] are

[18] For many-body effects in a single layer degenerate Fermi gas see Refs. [76, 78].

[19] Strong confinement means that the typical energy scale of the gas is much lower than the confinement energy $\hbar\omega_z$. In case of thermal gases, this requires temperatures $k_BT \ll \hbar\omega_z$, whereas in case in quantum degenerate Bose or Fermi gases, the typical energy is set by the chemical potential μ and the Fermi energy ϵ_F, respectively, therefore $|\mu|, \epsilon_F \ll k_BT$ is needed. Typically in deep optical lattices the confinement energy is in the range of $10 - 100\,$kHz, i.e. in the micro-kelvin range, which is well above the temperature range of experiments today.

governed by the scattering amplitudes in the $\nu = \nu' = 0$ channel, similarly to the case of exactly two-dimensional gases discussed in Subsection 3.1.

The emergent interlayer quasi-bound resonances provide a simple, geometrical way to control these parameters. The low energy $0 < \epsilon \ll \omega_z$ scattering amplitude in the $\uparrow\downarrow$-channel is shown in Fig. 3.6 (a) as a function of the layer separation. Conforming our naive expectation, the interaction initially decreases with increasing separation for the parameters chosen, due to the diminishing overlap between the atomic clouds of the layers. However, as the energy of the negative energy bound state eventually approaches zero (shown in Figs. 3.6 (b)-(e)), a sharp Feshbach-like resonance emerges in the interaction between the two species. As we cross the resonance, the effective interaction turns from repulsive to attractive, and on resonance it reaches a purely imaginary, universal value, $f^{00}_{\uparrow\downarrow} = -4i$. At this point of strong interactions, $|f^{00}_{\uparrow\downarrow}|^2$ takes on its maximal possible value.

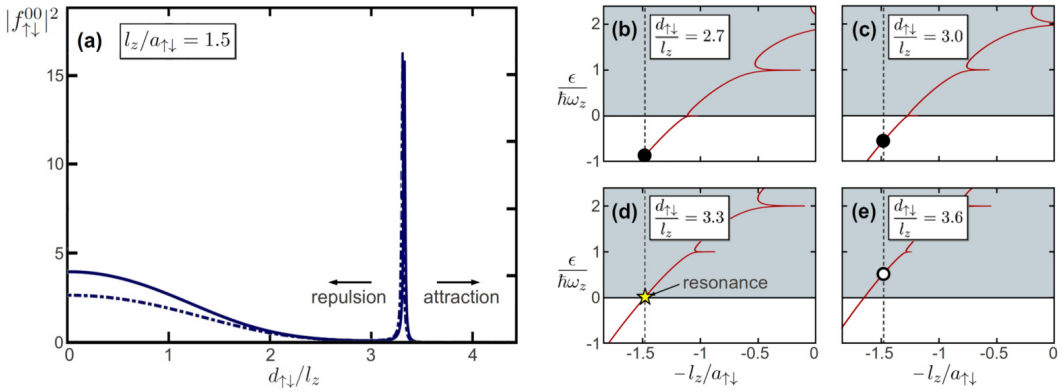

Figure 3.6: Geometrical tuning of interspecies interactions for $l_z/a_{\uparrow\downarrow} = 1.5$. (**a**) Resonant behavior of the interspecies scattering amplitude $f^{00}_{\uparrow\downarrow}$, in terms of the layer separation. At a separation $d_{\uparrow\downarrow}/l_z \approx 3.3$, a sharp Feshbach resonance-like structure emerges, as the energy of a quasi-bound molecular approaches that of the scattered particles, $\epsilon/\hbar\omega_z = 0.01$ (dashed) and 0.05 (full line). (**b**)-(**e**) Energy of the bound (full circle) and quasi-bound molecules (open circle) at increasing layer separations $d_{\uparrow\downarrow}/l_z = 2.7$, 3.0, 3.3 and 3.6. The interaction resonance shown in (**a**) corresponds to the separation, where the quasi-bound molecule appears at zero energy, shown in (**d**). [Dashed lines in (**b**)-(**e**) indicate the value of the interspecies scattering length.]

Importantly, in contrast to single layer systems exhibiting interaction resonances only on the negative side of the three-dimensional magnetic Feshbach resonance [65], interlayer resonances appear for *all* values of the scattering amplitude, being actually much sharper in the repulsive case, $a_{\uparrow\downarrow} > 0$. Furthermore, as the layer separation is increased, the position of the resonances shifts to smaller and smaller values of the scattering length $a_{\uparrow\downarrow} > 0$, as indicated in Figs. 3.4 (b)-(e), and therefore, confinement-induced resonances appear also at relatively small values of the scattering lengths, $a_{\uparrow\downarrow} \lesssim l_z$. This opens up a way to reach strong interactions in systems

where only moderate values of the scattering length are available, e.g. due to the lack of appropriate interspecies magnetic Feshbach resonances.

An intuitive way to think about the emergence of these resonances is as follows: In the case of an unconfined gas, weak repulsive scattering lengths correspond to a bound state at relatively large binding energies $E^B_{\uparrow\downarrow} \sim \hbar^2/(m a^2_{\uparrow\downarrow})$. This binding energy is weakened in the bilayer system, if the constituent atoms are separated well enough from each other. At sufficiently large separations, the binding energy becomes exponentially close to zero, and, due to the peculiar properties of two-dimensional scattering, a corresponding quasi-bound molecule appears at small positive energies $\epsilon \sim |E^B_{\uparrow\downarrow}| \sim 0$, leading to the resonance in interspecies interactions (see Fig. 3.6).

At large enough separations $d_{\uparrow\downarrow}/l_z \gtrsim 1$, the interaction resonances become especially sharp in energy, due to the increased lifetime of the corresponding molecular state. Then, the tiny spatial overlap of the ground state harmonic oscillator wave functions leads to an almost negligible effect of the $\nu = 0$ scattering channel on the scattering amplitudes, whereas the more extended $\nu = 1$ level can still have non-negligible overlap, and thus a significant contribution to $f^{00}_{\alpha\beta}$. In this regime, $\phi^2_0(d_{\uparrow\downarrow}) \approx 0$, and thus the function $w_{\uparrow\downarrow}$ in Eq. (3.7) can be approximated at small energies as, $w_{\uparrow\downarrow} \simeq -\phi^2_1(d_{\uparrow\downarrow}) \log|\epsilon/(\hbar\omega_z) - 1| + \phi^2_0(d_{\uparrow\downarrow})\, i\pi\Theta(\epsilon) + \tilde{\gamma}_{\alpha\beta}$ with the auxiliary constant $\tilde{\gamma}_{\alpha\beta}$ of order 1. $w_{\uparrow\downarrow}$ thus exhibits only a tiny imaginary part proportional to $\phi^2_0(d_{\uparrow\downarrow})$, and, at large separations, the scattering amplitude takes on the simple form

$$f^{00}_{\uparrow\downarrow}(\epsilon \approx 0)\Big|_{d_{\uparrow\downarrow}/l_z \gtrsim 1} \;\approx\; \frac{4\pi}{\frac{\phi^2_1(d_{\uparrow\downarrow})}{\phi^2_0(d_{\uparrow\downarrow})} \cdot \frac{\epsilon - E^1_{\uparrow\downarrow}}{\hbar\omega_z} + i\pi\Theta(\epsilon)},$$

which reflects a resonant behavior of the scattered particles with a long-lived molecular state of energy $E^1_{\uparrow\downarrow}$, indicated by the open circle in Fig. 3.6 (e). Indeed, at large separations, the quasi-bound states below the edge of the $\nu = 1$ channel gain an exponentially increased lifetime, and they correspondingly lead to narrow resonances, when $E^1_{\uparrow\downarrow} \sim 0$.

As shown in Fig. 3.7 one can also create similar strong resonances in the interaction, by only a slight tuning of the scattering length, with the layer separation kept fixed.[20] Notice that this kind of interaction tuning can be also applied in intraspecies channels, ($\uparrow\uparrow$ and $\downarrow\downarrow$). A further possibility — applied previously in one-component gases to control intraspecies interactions and to realize thereby the strongly interacting Tonks–Girardeau gas [79–81] — is to modify the trapping potential ω_z by varying the depth of the optical lattice potential. These methods together offer an *independent* control of interaction parameters of a two-component gas.

[20] This corresponds to moving 'horizontally' in Fig. 3.4, and can be facilitated by the use of an interlayer magnetic Feshbach resonance.

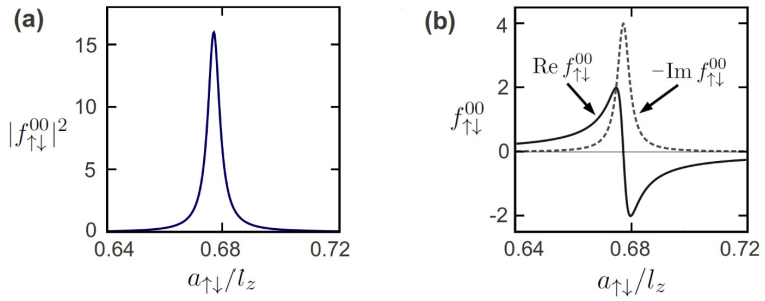

Figure 3.7: Resonant behavior of the interspecies scattering amplitude $f^{00}_{\uparrow\downarrow}$, as the scattering length, $a_{\uparrow\downarrow}$, is varied through the resonance shown in Fig. 3.6 (a), now with the layer separation kept fixed at $d_{\uparrow\downarrow} = 3.3\, l_z$. (**a**) We find a strong peak in the scattering amplitude, as $a_{\uparrow\downarrow}$ is tuned across the Feshbach-like resonance at $l_z/a_{\uparrow\downarrow} \approx 1.5$. (**b**) Crossing the resonance, the interaction turn from repulsive to attractive, and, due to the finite lifetime of the resonant molecule, it exhibits a large imaginary part on resonance.

3.5 Detection of quasi-bound molecules in a shaking experiment

In the past decade, the existence of confinement-induced *bound* molecules has been demonstrated in a number of spectroscopy experiments with single layer gases [82–84]. Nevertheless, *quasi-bound* molecules at positive energy remained elusive, due to their very short lifetimes. As we demonstrated in the previous section, their decay rates can be vastly suppressed in bilayer gases by simply increasing the separation of the layers, offering a new opportunity to detect and investigate these states for the first time. In this section, we show how these states can be identified in the *shaking spectrum* of a strongly confined dilute Bose gas ($k_B T \ll \hbar\omega_z$). In an experiment, shaking can be induced by periodically modulating the magnetic field that separates the layers, thereby shaking them in opposite direction. The effect of the modulation field δB_z of frequency ω can be described by the time-dependent single-particle Hamiltonian $\mathcal{H}_\alpha$,

$$\delta\mathcal{H}_\alpha(t) = -h_\alpha \cos(\omega t)\, z_\alpha/l_z \tag{3.30}$$

on the single-particle level. For simplicity, let us assume in the following an equal coupling of the magnetic field gradient to the spin components. Thus the fields h_α characterizing the amplitudes of shaking are equal, $h_\uparrow = -h_\downarrow = h_0 \sim \mu_B(\nabla\delta B_z)$. In the many-body, basis introduced in Eq. (3.16), the shaking Hamiltonian takes on the form $\delta H_\alpha = \mp h_0 \cos(\omega t)\, \Xi_\alpha$, with Ξ_α, corresponding to the z_α/l_z term, given by

$$\Xi_\alpha = \sum_{n=0}^{\infty} \int \frac{d^2q}{(2\pi)^2} \sqrt{\frac{n+1}{2}} \left(a^\dagger_{\alpha\, n+1}(\mathbf{q})\, a_{\alpha\, n}(\mathbf{q}) + \text{h.c.} \right). \tag{3.31}$$

We thus see that, due to the selection rules imposed by harmonic confinement, to leading order, the magnetic field gradient couples only neighboring harmonic levels

$n \leftrightarrow (n+1)$ in both layers. Hence, in a strongly confined gas with essentially no population of the $n \neq 0$ levels, dominantly $n = 0 \to 1$ transitions will be excited in each layer. Considering two atoms in the cloud, we can decompose their single-particle excitations, $|\mathbf{n}\rangle_{\rm exc} = |0,1\rangle$ and $|1,0\rangle$, in terms of their center of mass and relative coordinates,

$$|\mathbf{n}\rangle_{\rm exc} = \Big(|N=1,\nu=0\rangle \pm |N=0,\nu=1\rangle\Big)/\sqrt{2},$$

corresponding to pair excitations $(N,\nu) = (0,0) \to (1,0)$ and $(0,0) \to (0,1)$. Therefore shaking not only allows to excite single particles to higher bands, but also, through the excitation of pairs of atoms to higher N and ν quantum numbers, to excite bound and quasi-bound molecular states as well. If the shaking frequency approaches the energy of these molecules, the excited particles experience increased scattering with other atoms in the gas that leads to an increased heating rate. In particular, $(N,\nu) = (0,0) \to (0,1)$ transitions excite the $\uparrow\downarrow$ interlayer quasi-bound molecule of energy $E^1_{\uparrow\downarrow}$, close to the $\hbar\omega_z$ threshold (open circle in Fig. 3.9 (b)). In contrast, the center of mass transitions $(N,\nu) = (0,0) \to (1,0)$ excite the particle pair to the *bound* molecular state in the $\uparrow\uparrow$ and $\downarrow\downarrow$-channels, shifted to positive energy due to their non-zero center of mass motion, $E^B_{\uparrow\uparrow} \to E^B_{\uparrow\uparrow} + \hbar\omega_z$ (and $E^B_{\downarrow\downarrow} + \hbar\omega_z$).[21] We therefore expect peaks in the absorption spectrum at all these energies.

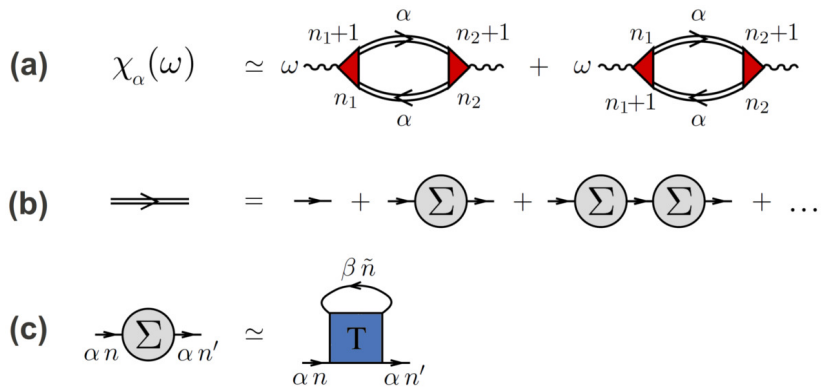

Figure 3.8: Feynman diagrams used to determine the absorption spectrum of the modulation experiment. (**a**) Bubble diagrams describing the shaking susceptibility in linear response theory, and neglecting vertex corrections. The triangular vertices denote the matrix elements of the operators in Eq. (3.31), at a frequency ω, whereas double lines denote propagators dressed by self-energy corrections, with the corresponding Dyson equation shown in (**b**). (**c**) Self-energy Σ, within the T-matrix approximation, corresponding to the interaction of the propagating particle with thermally excited atoms.

[21] Although there is a bound state in the $\uparrow\downarrow$-channel as well, its energy and weight is exponentially suppressed at the parameters chosen in Fig. 3.9, and they are thus not visible in the spectrum.

The energy absorption rate of the gas in layer α

$$\dot{\epsilon}_\alpha(\omega) = h_\alpha^2 \, \frac{\omega \, \chi_\alpha''(\omega)}{2}$$

is determined by imaginary part of the shaking susceptibility, χ_α, which is given in linear response theory by the Kubo formula

$$\chi_\alpha(t) = i\Theta(t) \left\langle [\Xi_\alpha(t), \, \Xi_\alpha(0)] \right\rangle.$$

In the diagrammatic approach, and with the vertex corrections neglected, this formula is equivalent to the bubble diagrams shown in Fig. 3.8 (a). In these diagrams, the triangular vertices correspond to the modulation operator Ξ_α, whereas the double lines indicate dressed retarded single particle propagators

$$(G_R^{-1})_\alpha^{nn'}(\omega, \mathbf{q}) = \omega + i0^+ + \frac{\hbar q^2}{2m} + n\omega_z \, \delta_{nn'} + \frac{1}{\hbar}\Sigma_\alpha^{nn'}(\omega, \mathbf{q}),$$

with the self-energy, Σ_α, incorporated through the Dyson series in Fig. 3.8 (b) [85]. The self-energy corrections originate from the interactions of the propagating particle with other atoms in the thermal gas, see Fig. 3.8 (c), mixing the harmonic oscillator channels $n \to n'$.

We assume a dilute thermal gas, and correspondingly, we keep terms in the self-energy, $\Sigma_\alpha^{nn'}$, only up to linear order in the density, and throw away thermal corrections to the many-body T-matrix as well. After the summation of the Matsubara series and analytic continuation to real frequencies we get

$$\Sigma_\alpha^{nn'}(\omega, \mathbf{q}) \simeq \sum_{\beta=\uparrow,\downarrow} \sum_{\tilde{n}=0}^{\infty} \int \frac{d^2k}{(2\pi)^2} \, n_B \left(\frac{\hbar^2 \mathbf{k}^2}{2m} + \tilde{n}\hbar\omega_z - \mu_\beta \right) \mathbf{T}_{\alpha\beta}^{n\tilde{n},n'\tilde{n}} \left(\omega + \frac{\hbar \, k^2}{2m} + \tilde{n}\omega_z, \mathbf{k} + \mathbf{q} \right).$$

Within the "bubble diagram" approximation, we can express the shaking susceptibility of the gas in terms of the single particle spectral functions, $\rho_\alpha^{nn'}(\omega, \mathbf{q}) = -\mathrm{Im}(G_R)_\alpha^{nn'}(\omega, \mathbf{q})/\pi$ (see Fig. 3.8 a). In the strongly confined gas the $n > 0$ levels are essentially unpopulated, and only the lowest level $n = 0 \to 1$ transitions give dominant contributions. The susceptibility over unit area is then given in the bubble diagram approximation by

$$\chi_\alpha(\omega) \simeq \int d\tilde{\omega} \int \frac{d^2\tilde{q}}{(2\pi)^2} \, n_B(\tilde{\omega} - \mu_\alpha) \left[\rho_\alpha^{00}(\tilde{\omega}, \tilde{q}) \, \rho_\alpha^{11}(\tilde{\omega} - \omega, \tilde{q})/2 + \rho_\alpha^{01}(\tilde{\omega}, \tilde{q}) \, \rho_\alpha^{01}(\tilde{\omega} - \omega, \tilde{q}) + \{\omega \leftrightarrow -\omega\} \right].$$

The numerically computed absorption spectrum is shown in Fig. 3.9 (a) for equal, repulsive scattering lengths in all three channels $a_{\alpha\beta} \equiv a$. The separation and the

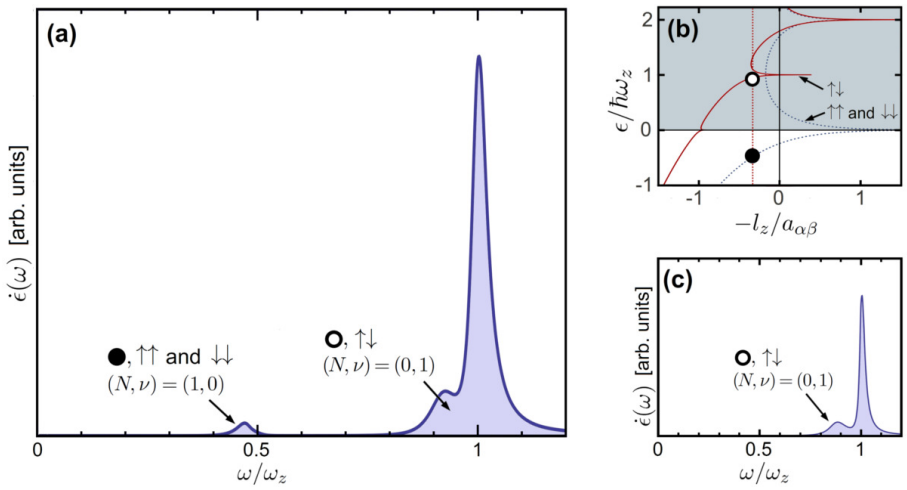

Figure 3.9: Detection of quasi-bound molecular states with shaking spectroscopy. (**a**) Absorption spectrum of a dilute Bose gas at a layer separation $d_{\uparrow\downarrow}/l_z = 2.5$, and at equal interactions in all channels, $a_{\uparrow\uparrow} = a_{\uparrow\downarrow} = a_{\downarrow\downarrow} = 3l_z$. Beside the large single-particle peak at $\omega \sim \omega_z$, we find two smaller peaks corresponding to interlayer ($\uparrow\downarrow$-channel) and intralayer molecules ($\uparrow\uparrow$ and $\downarrow\downarrow$), whose center of mass and relative oscillator quantum numbers are also shown. The energy of the corresponding bound intralayer (full circle) and quasi-bound interlayer molecule (open circle) are shown in (**b**). [Physical parameters: $k_BT/(\hbar\omega_z) = 0.03$, $|\mu_\uparrow| = |\mu_\downarrow| = k_BT/3$.] (**c**) In the absence of intraspecies interactions, $a_{\uparrow\uparrow} = a_{\downarrow\downarrow} = 0$, the bound states in these channels disappear, and the corresponding peak vanishes from the modulation spectrum. [Parameters: $a_{\uparrow\downarrow}/l_z = 2.6$, $k_BT/(\hbar\omega_z) = 0.06$, $|\mu_\uparrow| = |\mu_\downarrow| = k_BT/3$.]

scattering lengths are chosen large enough ($d_{\uparrow\downarrow}/l_z \sim a/l_z \sim 3$) so that the lifetime and the weight of the interlayer quasi-bound state (open circle in Fig. 3.9 (b)) be observable. We find three separate peaks in the spectrum. The largest one at an energy $\omega \sim \omega_z$ corresponds to single-particle intrawell excitations – the peak weight is therefore proportional to the boson density. We also observe, however, two clearly distinguishable smaller peaks, originating from resonances with bound and quasi-bound molecular states. Due to their two-particle nature, their intensities are proportional to the *square* of the density of the gas. These peaks are therefore expected to become more pronounced at higher densities, as the system is driven towards quantum degeneracy. The peak close to the single-particle excitation peak at $\omega \sim \omega_z$ originates from the interlayer quasi-bound molecule (open circle in Fig. 3.9 (b)). The other two-particle peak at smaller frequencies has a different origin: it corresponds to resonances with molecular bound states in the $\uparrow\uparrow$ and $\downarrow\downarrow$-channels, pushed to positive frequencies by their oscillating center of mass motion. Excitation into this state is made possible by the center of mass excitations of particle pairs, due to shaking. Note that in case of non-equal scattering amplitudes, $a_{\uparrow\uparrow} \neq a_{\downarrow\downarrow}$, this peak is expected to split up, whereas if the interaction

between identical particles is negligible, $a_{\uparrow\uparrow}, a_{\downarrow\downarrow} \to 0$, they vanish from the shaking spectrum (see Fig. 3.9 (c)).

3.6 Experimental realization

In order to observe confinement-induced molecules and interaction resonances in an experiment, one needs to go into the parameter range where the effects of confinement and interaction are roughly of the same order, $a_{\alpha\beta} \sim l_z$. To reach this regime, a rather simple approach is to decrease the oscillator length $l_z = \sqrt{\hbar/(m\omega_z)}$ by choosing heavy atoms (such as ^{87}Rb and ^{137}Rb) and using extremely strong trapping frequencies.[22] On the other hand, in systems where sufficiently broad interspecies Feshbach resonances are available, it is sufficient to apply only standard trapping frequencies, $\omega_z \sim 10 - 100$ kHz.[23] Such resonances are common and widely used in case of fermionic species (such as ^{6}Li and ^{40}K) [83,86–88]. Fermionic atoms are thus ideal candidates for detecting interlayer quasi-bound molecules in a modulation experiment,[24] and the results presented in this chapter also provide a way for the geometric tuning of their interactions. Furthermore, many-body effects in quantum-degenerate Fermi gases can be taken into account using methods similar to those presented in Section 3.3 and in Ref. [76], and they can lead to several exotic phenomena, such as exciton condensation [67,68], and interaction resonances [76,86].

In case of bosonic atoms, wide Feshbach resonances between hyperfine components of the same isotope are relatively rare [88,89]. However, those between different atomic elements are much more common, and they have been used in a number of bosonic mixtures, e.g. ^{7}Li–^{87}Rb, ^{39}K–^{87}Rb and ^{41}K–^{87}Rb systems [88, 90–93]. Importantly, the calculations presented in this chapter apply with only slight modifications to the case of bosonic mixtures, if the trapping frequencies for the two atomic components are equal. This can be easily achieved by using a separate, appropriately tuned laser for trapping each component.[25] Thus, the experimental

[22] In case of extreme trapping, $\omega_z \gg 100$ kHz, the interaction potential may not be considered point-like, since the variation of the trapping potential can be non-negligible within its effective range, $R_{\rm int}$. In this case, the interaction potential used in this chapter may require energy dependent corrections [74, 75]. However, this is expected to lead to only slight modifications of the overall scattering behavior in the confined system.

[23] We note, in case of very narrow Feshbach resonances the spatial inhomogeneity of the external magnetic field could lead to inhomogeneous interactions across the layers. The variation of the magnetic field is, however, usually very small. In particular, the magnetic field gradients required to reach separations $d_{\uparrow\downarrow} \sim l_z$ are rather weak, $\nabla B_z \sim 0.01 - 1$ G/mm, and they lead to a weak magnetic field difference between the centers of the layers, in the range of $\Delta B \sim 10 - 100$ mG, invalidating our results only in case of some very narrow Feshbach resonances, whose widths are comparable to ΔB.

[24] The shaking spectrum in the previous section has been presented to the case of a dilute Bose gas, however, the calculations can be straightforwardly carried through to the fermionic case as well, and are expected to give similar results.

[25] For instance, in case of scattering of particles of mass m_α and m_β in the vacuum, one simply needs to introduce the center of masses $M_{\alpha\beta} = m_\alpha + m_\beta$, the reduced masses $\mathrm{m}_{\alpha\beta} = m_\alpha m_\beta/(m_\alpha + m_\beta)$ and the corresponding channel-dependent oscillator lengths, and rewrite the results for the

proposals presented in this chapter shall be appropriate for bosonic mixtures as well.

3.7 Summary

In this chapter, we studied the effects of the confining potential on the interactions of a two-component gas in a bilayer geometry. We found, that confinement leads to exciton-like interlayer bound and quasi-bound molecules, appearing for *both* positive and negative scattering lengths. Interestingly, the spatial extent of these molecules can several times exceed the interspecies scattering lengths, and become several hundred times larger than the actual size of the constituent atoms. Increasing the layer separation, the lifetime of these molecules increases exponentially, that makes them observable in commonly used shaking experiment, as we demonstrated through detailed many-body calculations.

Furthermore, the emergence of these quasi-bound molecules also leads to *'geometrical Feshbach resonances'* in the interspecies interactions (scattering amplitudes). The rather sensitive dependence of their binding energies on the layer separation allows one to control interspecies interactions in a purely geometrical way. As the layers are separated from each other, the energy of the molecule eventually approaches zero, and the low energy interactions in the gas get resonantly enhanced. Thus, rather counterintuitively, one can induce *strong interaction* in the $\uparrow\downarrow$-channel by spatially separating the two layers. In contrast to the shallow interaction resonances found in single layer systems, these resonances appear to be significantly sharper, and they are also present on the repulsive side of the three-dimensional Feshbach resonance, and even at moderate values of the scattering length. Thus, together with traditionally used magnetic Feshbach resonances, used previously to control intra-species interactions (i.e. in channels $\uparrow\uparrow$ and $\downarrow\downarrow$), the hereby proposed "separation-tuning" enables a significantly wider, purely geometrical control of interacting, low-dimensional multicomponent systems.

scattering amplitudes appropriately.

4

Exotic superconducting phases of a three-component fermion mixture

Superconductivity pervades physics in many different appearances and at very different energy scales. Most importantly, it characterizes the low temperature phase diagram of many metallic elements, but protons and neutrons in nuclei are also proposed to condense very similarly into a superconducting (SC) state [94], not to mention quarks, forming a large variety of color-superconducting phases that are proposed to fill the interior of certain neutron stars [95]. It is rather striking how far-reaching the idea of the Bardeen–Cooper–Schrieffer (BCS) theory is: a weak effective attraction between fermionic particles leads to a collective pairing mechanism that opens up a gap around the Fermi level, whose half-width, Δ becomes the single dominant energy scale characterizing the low-energy behavior of the material, irrespective of the details of the underlying microscopic physics [96]. This collective quantum behavior is widely exploited today in scientific, industrial and medical applications [96, 97]. Interestingly, despite the enormous successes of BCS theory, one of the greatest unsolved problems of condensed matter physics today is related to high-temperature (high-Tc) superconductors. Although these superconducting materials are the ones most frequently used in practical applications, the microscopic origin of their superconductivity is still unknown [58].

Systems of ultracold atoms offer a number of unique viewpoints on superconductivity. The tunability of both the number of fermionic species involved in pairing and the interaction strength allows one to study a significantly larger parameter range than in traditional materials. This has led to the experimental discovery of a number of novel superconducting phenomena, and has sprung several experimental proposals for exotic superconducting phases. One of the most interesting achievements of the field has been the experimental study of the so-called BEC-BCS transition of

a strongly attractive two-component Fermi gas, tuned across a Feshbach resonance, whereby the system goes through a crossover from superconducting state consisting of loosely bound Cooper pairs to a Bose–Einstein condensate of bound molecular pairs [39,98–100]. Ultracold atoms also offer the prospect of a deeper understanding of the mysterious superconducting phases of high-Tc cuprate materials. In particular, the low temperature phase diagram of the two-dimensional fermionic Hubbard model, realizable using optical lattices in the cold atomic setting, is expected to show similar characteristics to those of high-Tc cuprates. Another exciting aspect of ultracold gas experiments, is the possibility to use multicomponent species and fermionic mixtures of atoms with very different masses. This has opened up the opportunity to investigate such exciting SC phases as the Sarma phase, in which superconducting pairs form in the interior of the Fermi sphere [101, 102], and to study analogues of color superconductivity [103] and "baryon" formation [104, 105], two fundamental concepts of quantum chromodynamics, the theory of quarks.

In this chapter, we shall uncover the phase diagram of a weakly attractive three-component fermionic mixture, and study its low temperature superconducting phases in the presence of an $SU(3)$ symmetric interaction. This system exhibits a number of exotic phenomena, such as the coupling of magnetization and superconducting order, leading to a ferromagnetic polarization of the gas at the onset of superconductivity [104–107], forbidden by symmetry in traditional two-component (electron) systems. Furthermore, we will see that the nature of superconducting to normal phase transition is significantly different from those in traditional electron materials. We shall discuss the complete phase diagram of the three-component mixture in terms of chemical potential differences and temperature. Despite the increased earlier theoretical interest in three component mixtures in the past ten years [103, 106], such a phase diagram had not been studied in detail before the work that forms the basis of this chapter: M. Kanász-Nagy and G. Zaránd, *"Global superfluid phase diagram of a three-component fermion mixture with magnetic ordering"*, Phys. Rev. B **86**, 064519 (2012).

4.1 SC to normal transition due to the Zeeman effect

As a first step towards understanding the rich physics of a three-component mixture, let us first discuss the simpler phase diagram of a *two-component* mixture. A key difference between ultracold atoms and electrons in a metal is that the former have no electric charge. Thus, even in an external magnetic field, the Meissner effect does not come into play, and the traditional decay mechanism of superconductivity, through the coupling of the magnetic field to the superconducting flow of Cooper pairs, is also absent[1]. Instead, chemical potential imbalances between the components play the primary role in ultracold gases by suppressing superconductivity due to the Zee-

[1] Although artificial magnetic fields have indeed been produced for neutral atoms, their creation requires additional efforts (e.g. rotating the condensates [39], or shaken optical lattices [108–110]), and we thus do not touch upon them in this thesis.

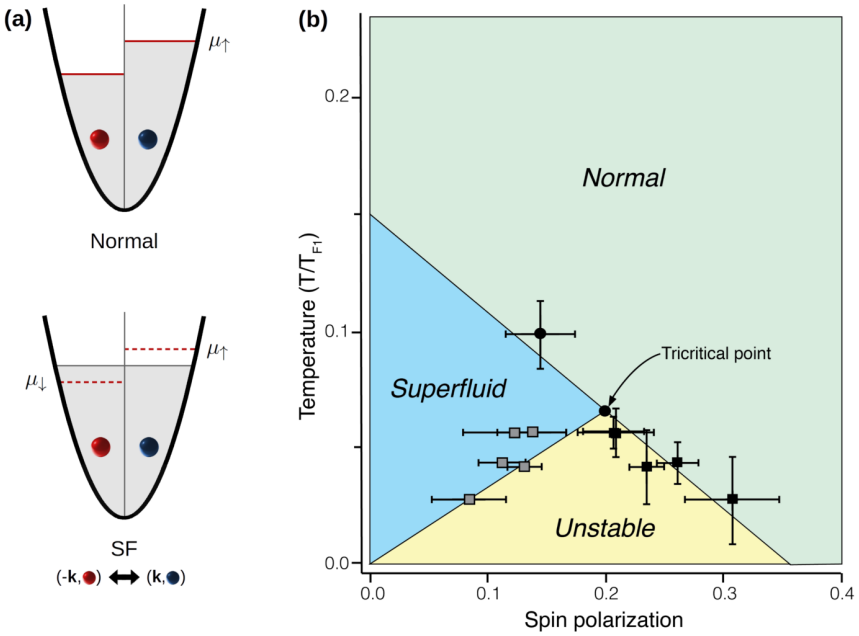

Figure 4.1: Mechanism of the SC-normal transition in a two-component Fermi mixture. (**a**) In the normal phase (top), a chemical potential imbalance leads to a shift in the Fermi energies of the components, whereas in the superconducting phase they are held together by the Cooper pairing mechanism. If the chemical potential imbalance becomes too large, the system goes into the normal phase. (**b**) Figure based on the experimentally measured phase diagram of Ref. [111], in terms of the temperature and spin polarization $(\tilde{n}_{11} - \tilde{n}_{22})/(\tilde{n}_{11} + \tilde{n}_{22})$ of the gas, as given by the densities, $\tilde{n}_{11}$ and $\tilde{n}_{22}$, of the two components. At low enough temperatures, an unstable region forms, indicating that the SC-normal transition becomes of first order in terms of the chemical potentials.

man effect. The underlying mechanism is perhaps most easily demonstrated in case of a two-component Fermi gas. In the superconducting phase at zero temperature, Cooper pairs are formed by atoms in different hyperfine states and in opposite momentum states $\mathbf{k}$ and $-\mathbf{k}$, near the Fermi surface. Thus, superconductivity requires the Fermi surfaces of the two components to remain at the same energy[2], as shown in Fig. 4.1 (a). If the chemical potentials of the two components $\tilde{\mu}_1$ and $\tilde{\mu}_2$, are not equal, then the energy cost of keeping the Fermi surfaces at an equal energy is proportional to the chemical potential imbalance, $\delta E_{\mathrm{kin}} \propto \tilde{\mu}_x = (\tilde{\mu}_1 - \tilde{\mu}_2)/\sqrt{2}$.

[2]This requirement may not hold in more exotic superconducting phases, such as the Fulde-Ferrell-Larkin-Ovchinnikov (FFLO) phase with spatially varying order parameter [112–114]. However, since previous works on two-component mixtures indicate that this phase appears only in a tiny region of the phase diagram [115, 116], here we restrict our investigation to spatially homogeneous phases. We shall neither consider Breached Pair (BP) or Sarma phases [101, 102, 117], since these would require fermions of very different masses.

At small imbalances, this energy cost is still smaller than the condensation energy gain of the superconductor, $\delta E_{\rm cond} \propto \tilde{\Delta}$, being proportional to the superconducting order parameter $\tilde{\Delta}$, and the system retains its superconducting state. However, at large enough imbalances, the kinetic energy favors the normal state, and the superconductivity vanishes through a Zeeman field induced phase transition. As has been pointed out early by Sarma [117], the transition is continuous at high temperatures, whereas it becomes of first order below the so-called Sarma temperature $T^{\rm Sarma}$, and above the chemical potential difference $\tilde{\mu}_x^{\rm Sarma}$. Sarma also determined the mean-field values of this critical point (Sarma point), and obtained

$$\tilde{T}^{\rm Sarma} = 0.58\,\tilde{T}_c\,, \qquad \tilde{\mu}_x^{\rm Sarma} = 1.5\,k_B\tilde{T}_c\,, \tag{4.1}$$

with $\tilde{T}_c$ being the critical temperature at $\tilde{\mu}_x = 0$. He also determined the critical chemical potential difference at zero temperature, known as the Clogston limit [118],

$$\tilde{\mu}_x^{\rm Clog} = \tilde{\Delta}(T=0) = 1.764\,k_B\tilde{T}_c. \tag{4.2}$$

Fig. 4.1 (b) shows the experimentally measured phase diagram of a two-component Fermi gas in terms of temperature and the spin polarization of the condensate. The unstable region at temperatures below $T^{\rm Sarma}$, where neither a spatially uniform superconducting, nor a normal phase can be stable, indicates that the SC-normal transition becomes of first order in terms of the chemical potentials [111].

4.2 Superconductivity in three-component mixtures

In the remaining parts of this chapter, we shall focus on a homogeneous system of three interacting fermion species, with weak $SU(3)$ symmetric attraction, described by the Hamiltonian

$$\begin{aligned} H &= \sum_\alpha \int \mathrm{d}^3 r\, \Psi_\alpha^\dagger(\mathbf{r})\,(\mathcal{H}_0 - \mu_\alpha)\,\Psi_\alpha(\mathbf{r}) \\ &- \sum_{\alpha\neq\beta} \frac{g_{\alpha\beta}}{2} \int \mathrm{d}^3 r\, \Psi_\alpha^\dagger(\mathbf{r})\Psi_\beta^\dagger(\mathbf{r})\Psi_\beta(\mathbf{r})\Psi_\alpha(\mathbf{r})\,, \end{aligned} \tag{4.3}$$

and study how the phase diagram of Sec. 4.1 gets modified by the presence of the third component. Here, the field operator $\Psi_\alpha(\mathbf{r})$ annihilates a fermion in a hyperfine state $\alpha = 1, 2, 3$, and for simplicity, the chemical potentials μ_α are considered uniform in space. We assume a simplified form of the single particle Hamiltonian $\mathcal{H}_0$. This enters the mean-field calculations only through the corresponding single particle density of states (DOS) near the Fermi surface, and its particular form is not very important. We assume the simple form for the DOS, $\rho(\epsilon) = \rho_0\,(1 + \eta\,\epsilon)$ with a cut-off at $\epsilon = \pm\Lambda$. Keeping the linear term $\rho_0\eta\,\epsilon$ is of primary importance since this term, characterizing in some sense the particle-hole symmetry breaking, is the primary source of the coupling between ferromagnetic and superconducting order parameters (see Section 4.3.3). In the weak coupling regime, however, higher order

derivatives of the density of states are expected to have only negligible effect on the phase diagram.[3]

The interaction parameter $g_{\alpha\beta}$ in Eq. (4.3) is related to the scattering lengths $a_{\alpha\beta}$ through appropriate renormalization,[4] and it is assumed to be $SU(3)$ symmetric, $g_{\alpha\beta} = g > 0$ for $\alpha \neq \beta$. This assumption is certainly justified for atoms with closed external s-shells, like Yb, Er and Dy, having thus perfectly $SU(N)$ symmetric s-wave interactions [119, 120]. Furthermore, it is also a well justified approximation for the widely used ^{6}Li atoms in the high magnetic field limit [121], whose scattering lengths can be made equal up to $\sim 0.1\%$ accuracy through the use of external radio frequency and microwave fields [122].

4.3 Mean-field calculations

We shall construct the global phase diagram of the three-component mixture in a mean-field analysis. Even this, however, is not entirely trivial. In earlier works [106, 123], the simultaneous treatment of SC and ferromagnetic ordering made use of a Hubbard–Stratonovich transformation, whereby one decouples the interaction partly in the ferromagnetic and partly in the superconducting channel. This approach, however, suffers from a certain degree of arbitrariness, since one needs to separate the interaction energy between the two competing orders 'by hand'.[5] Treating the SC and magnetic channels at an equal footing therefore requires care. Furthermore, similar to two-component systems discussed in Sec. 4.1, the SC-normal transition becomes of first order at low temperatures, and the free energy thus develops multiple local minima [117], leading to further complications in the mean-field treatment.

To analyze the full phase diagram, we employ two complementary approaches. At temperatures near the critical temperature T_c^0 at the $SU(3)$ symmetric point of the phase diagram ($\mu_\alpha \equiv \mu$),[6] we apply a self-consistent method based on 'equations of motion' (EOM) of mean-field propagators, in which vertex corrections are systematically neglected. These equations, however, exhibit multiple solutions at low temperatures, as the SC-normal transition becomes of first order. We thus employ another, Gaussian variational approach to describe this regime. The latter technique is based on finding the best mean-field approximation to the free energy of the interacting system. Both approaches are *exempt* from the arbitrariness of the Hubbard-Stratonovich transformation, and account reliably for the interplay between ferromagnetic and superconducting order. Remarkably, they are entirely

[3] Importantly, the interactions renormalize the chemical potentials, and therefore the position of the renormalized Fermi energy, ϵ_F, and the corresponding single particle density of states, ρ_F need to be determined self consistently.

[4] Similar to the case in Chapter 3, the interaction parameter can be approximated by requiring that the vacuum T-matrix of the system at zero energy gives $\mathbf{T}^{\mathrm{3D}}_{\alpha\beta}(\Omega \to 0-, \mathbf{Q} = 0) = 4\pi\hbar^2\, a_{\alpha\beta}/m$, (see Eq. (A4)).

[5] Two-component mixtures are, of course, exempt from this kind of arbitrariness, since there simultaneous SC and magnetic ordering is forbidden on symmetry grounds.

[6] Throughout this chapter, we shall refer to the critical temperature at the $SU(3)$ symmetric point, where all chemical potentials are equal, as T_c^0 (see also Sec. 4.4).

consistent with each other: the EOM self-consistency equations actually correspond to the saddle point equations of the mean-field free energy (see Section 4.3.2). However, the Gaussian variational approach goes beyond the EOM method in that it provides a mean-field estimate for the free energy, and thus allows us to distinguish between the non-equivalent local minima, and choose the physically relevant solutions.

4.3.1 Equation of motion technique

In this subsection, we introduce the imaginary time equations of motion of the system's propagators, and derive the self-consistent EOM equations for the SC and magnetic order parameters. In order to simplify our notations, let us first introduce the six component Nambu spinor field

$$\Phi(x) = \Big(\Psi(x), \Psi^\dagger(x)\Big)^{\mathrm{T}} , \tag{4.4}$$

with the combined notation for the space and imaginary time coordinates, $x = (\mathbf{r}, \tau)$. Assuming spatial homogeneity, the corresponding 6×6 (imaginary time ordered) propagator matrix $\mathbf{G}(x_1, x_2) \equiv -\langle T_\tau\, \Phi(x_1) \circ \Phi^\dagger(x_2)\rangle$ only depends on relative space and time coordinates, $\mathbf{G}(x_1, x_2) = \mathbf{G}(x_1 - x_2)$. This propagator provides a compact notation for the equations of motion of all relevant propagators, since it simultaneously contains the normal and the anomalous Green's functions of the fields $\Psi_\alpha(x)$. By inserting the equations of motion of the fields

$$\partial_\tau \Psi_\alpha(x) = [H, \Psi_\alpha(x)] .$$

into these Green's functions (such as $-\langle \mathrm{T}_\tau \Psi_\alpha(x_1)\Psi^\dagger_\beta(x_2)\rangle$), we can derive EOM equations for the propagators, such as

$$\begin{aligned}(\partial_{\tau_1} + \mathcal{H}_0(\mathbf{r}_1) - \mu_\alpha)\ \langle \mathrm{T}_\tau \Psi_\alpha(x_1)\Psi^\dagger_\beta(x_2)\rangle &= \delta_{\alpha\beta}\ \delta^{(4)}(x_1 - x_2) \\ &+ \sum_\gamma g_{\alpha\gamma}\, \langle \mathrm{T}_\tau\, \Psi^\dagger_\gamma(x_1)\, \Psi_\gamma(x_1)\Psi_\alpha(x_1)\, \Psi^\dagger_\beta(x_2)\rangle,\end{aligned} \tag{4.5}$$

with $\delta^{(4)}(x)$ denoting the four dimensional Dirac-delta function. We find similar equations in case of the anomalous propagators, $-\langle \mathrm{T}_\tau \Psi_\alpha(x_1)\Psi_\beta(x_2)\rangle$ as well. In order to obtain the required mean-field self-consistency equations, we simply decouple the four-point functions on the right hand side of Eq. (4.5) and neglect vertex corrections, as shown in Fig. 4.2. This leads to a generalization of the standard Bogoliubov–de Gennes (BdG) equations, which allows for the simultaneous treatment of magnetic and superconducting ordering in an unbiased way, through the normal and anomalous propagators, respectively. Furthermore, even in the simpler two-component case, it also incorporates, e.g., the renormalization of the Pauli susceptibility at the mean- field level (see Sec. 4.4.3), that is neglected in the traditional BdG treatment.

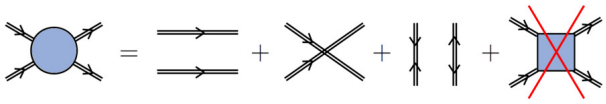

Figure 4.2: Decoupling of the four-point functions (left) in the equations of motion of the propagators, Eq. (4.5), through the omission of vertex corrections (square). Heavy lines denote dressed propagators.

The resulting mean-field equations take on the following simple form in the form of Nambu propagators in frequency and momentum space,

$$\mathbf{G}(i\omega_n, \mathbf{k})^{-1} = i\hbar\omega_n - \mathbf{\Xi}(\epsilon_\mathbf{k}), \tag{4.6}$$

with $\hbar\omega_n = (2n+1)\pi\, k_B T$ denoting the (fermionic) Matsubara frequencies and the matrix $\mathbf{\Xi}(\epsilon)$ being defined as

$$\mathbf{\Xi}(\epsilon) \equiv \begin{pmatrix} \epsilon - \mathbf{M} & \mathbf{\Delta} \\ \mathbf{\Delta}^+ & -(\epsilon - \mathbf{M})^* \end{pmatrix}. \tag{4.7}$$

Here, the SC order parameter, $\mathbf{\Delta}$, and the matrix of renormalized chemical potentials, $\mathbf{M}$, are given as

$$\Delta_{\alpha\beta} \equiv g_{\alpha\beta}\, d_{\alpha\beta}, \tag{4.8}$$

$$M_{\alpha\beta} \equiv \mu_\alpha \delta_{\alpha\beta} + \left(\delta_{\alpha\beta} \sum_\gamma g_{\alpha\gamma} n_{\gamma\gamma} - g_{\alpha\beta} n^*_{\alpha\beta} \right), \tag{4.9}$$

and are defined in terms of the matrix of densities and anomalous densities,

$$n_{\alpha\beta} \equiv \langle \Psi^\dagger_\alpha(x_1)\Psi_\beta(x_1)\rangle, \tag{4.10}$$

$$d_{\alpha\beta} \equiv \langle \Psi_\alpha(x_1)\Psi_\beta(x_1)\rangle, \tag{4.11}$$

respectively. Although the matrices $\mathbf{n}$ and $\mathbf{d}$ give a perfect characterization of the SC and ferromagnetic ordering, it is more natural to use $\mathbf{M}$ and $\mathbf{\Delta}$ as order parameters in our mean-field equations. While $\mathbf{\Delta}$ is the straightforward generalization of the SC order parameter of two-component BCS theory [96], the renormalized chemical potentials simply account for ferromagnetic ordering, since a shift in the densities of the components leads to a simultaneous shift in $M_{\alpha\beta}$ through Eq. (4.9).

Through Eqs. (4.10) and (4.11), the densities and anomalous densities are given by the appropriate elements of the Nambu propagators at equal times and equal positions,

$$\mathbf{G}(x=0) = k_B T \sum_{\omega_n} \int d^3k\, \mathbf{G}(i\omega_n, \mathbf{k}). \tag{4.12}$$

Performing the Matsubara summation of the inverse of Eq. (4.6) we find that this propagator is given by

$$\mathbf{G}(x=0) = \begin{pmatrix} \mathbf{n}^* & -\mathbf{d} \\ -\mathbf{d}^+ & -\mathbf{n} + \int \mathrm{d}\epsilon\, \rho(\epsilon) \end{pmatrix} = \int_{-\Lambda}^{\Lambda} \mathrm{d}\epsilon\, \rho(\epsilon)\, n_\mathrm{F}\left(\mathbf{\Xi}(\epsilon)\right), \tag{4.13}$$

with n_{F} denoting the Fermi function.[7] This equation, together with the definition of the order parameters in Eqs. (4.7-4.9) thus provides a system of self-consistent equations, that constitute the EOM method. By solving these equations through numerical iterations, we were able to uncover the phase diagram at temperatures near T_c^0, and at arbitrary chemical potential differences (see Sec. 4.4). We note that the matrix $\mathbf{\Xi}(\epsilon)$ in Eq. (4.7) has a symplectic symmetry,

$$\begin{pmatrix} \mathbf{0} & \mathbf{1} \\ \mathbf{1} & \mathbf{0} \end{pmatrix} \cdot \mathbf{\Xi}\,(\epsilon) \cdot \begin{pmatrix} \mathbf{0} & \mathbf{1} \\ \mathbf{1} & \mathbf{0} \end{pmatrix} = -\,\mathbf{\Xi}^{\mathrm{T}}\,(\epsilon)\,, \tag{4.14}$$

due to the skew- and Hermitian symmetry of the order parameters $\mathbf{\Delta}$ and $\mathbf{M}$, respectively. This makes the eigenvalues of $\mathbf{\Xi}(\epsilon)$ come in $(\lambda, -\lambda)$ pairs, which is responsible for the special structure of the equal time, equal position propagator in Eq. (4.13).

4.3.2 Mean-field free energy

In order to investigate the low temperature region of the phase diagram, where the EOM method breaks down, we employ a Gaussian variational method, that consists of finding the best quadratic approximation to the free energy $F = -k_B T \log \mathcal{Z}$ of the interacting system. Here the grand canonical partition function $\mathcal{Z}$ is given by the functional integral

$$\mathcal{Z} = \int \mathfrak{D}\overline{\psi}\,\mathfrak{D}\psi\, e^{-S[\overline{\psi},\psi]}, \tag{4.15}$$

with the action $S = S_0 + S_{\mathrm{int}}$, written in terms of a non-interacting part and the interaction term,

$$S_0 = -\frac{1}{2}\int \mathrm{d}1\,\mathrm{d}2\;\overline{\phi}(1)\,\mathcal{G}_0^{-1}(1,2)\,\phi(2), \tag{4.16}$$

$$S_{\mathrm{int}} = -\sum_{\alpha\beta}\frac{g_{\alpha\beta}}{2}\int \mathrm{d}x\;\overline{\psi}_\alpha(x)\overline{\psi}_\beta(x)\psi_\beta(x)\psi_\alpha(x), \tag{4.17}$$

the former defined in terms of the Nambu spinor fields, $\phi = \left(\psi, \overline{\psi}\right)^{\mathrm{T}}$. To simplify our notations, we introduced the multiple index variables $''1'' = (\mathbf{r}_1, \tau_1, \nu_1)$. Thus, $\int \mathrm{d}1 \ldots$, denotes integration over imaginary time and space variables, as well as summation over Nambu indices ($\nu_1 = 1, \ldots, 6$) in a compact way. The inverse propagator

$$-\mathcal{G}_0^{-1} = \delta^{(4)}(x_1 - x_2)\,\left(\partial_{\tau_2} + \begin{pmatrix} \mathcal{H}_0 - \hat{\mu} & 0 \\ 0 & -(\mathcal{H}_0 - \hat{\mu}) \end{pmatrix}\right), \tag{4.18}$$

contains the single particle Hamiltonian, $\mathcal{H}_0$, of the free fields in Eq. (4.3), whereas $\hat{\mu}_{\alpha\beta} = \mu_\alpha\,\delta_{\alpha\beta}$ denotes the 3×3 diagonal matrix of the (bare) chemical potentials.

[7] Since $n_{\mathrm{F}}\,(\mathbf{\Xi}(\epsilon))$ is a matrix function, its evaluation requires numerical diagonalization of $\mathbf{\Xi}(\epsilon)$ for each value of ϵ. The evaluation of Eq. 4.13 is numerically rather costly, and we thus needed to introduce a number of elaborate numerical methods to speed up our algorithm.

We proceed by invoking a standard inequality due to Feynman [124],

$$F \leq F_{\mathrm{G}}[\mathcal{G}] \equiv -k_B T \, \log \mathcal{Z}_{\mathcal{G}} + k_B T \, \langle S - S_{\mathcal{G}} \rangle_{\mathcal{G}} \, , \tag{4.19}$$

that holds for any Gaussian action

$$S_{\mathcal{G}} \equiv -\frac{1}{2} \int \mathrm{d}1 \, \mathrm{d}2 \, \overline{\phi}(1) \, \mathcal{G}^{-1}(1,2) \, \phi(2) \, , \tag{4.20}$$

with the partition function $\mathcal{Z}_{\mathcal{G}}$ and the thermal average $\langle \dots \rangle_{\mathcal{G}}$ given by

$$\mathcal{Z}_{\mathcal{G}} \equiv \int \mathfrak{D}\overline{\psi} \, \mathfrak{D}\psi \, e^{-S_{\mathcal{G}}[\overline{\psi},\psi]} \, , \tag{4.21}$$

$$\langle \dots \rangle_{\mathcal{G}} \equiv \frac{1}{\mathcal{Z}_G} \int \mathfrak{D}\overline{\psi} \, \mathfrak{D}\psi \, \dots \, e^{-S_{\mathcal{G}}[\overline{\psi},\psi]} \, . \tag{4.22}$$

Notice that, at this point, we consider the most general quadratic action, Eq. (4.20), and we do not even require the locality of $S_{\mathcal{G}}$. Since $S_{\mathcal{G}}$ is quadratic, the Nambu propagator matrix can be simply written as

$$\langle \phi(1) \, \overline{\phi}(2) \rangle_{\mathcal{G}} = -\mathcal{G}(1,2) \, , \tag{4.23}$$

and expectation values can be evaluated using Wick's theorem.[8]

We can thus find the best Gaussian approximation to the full free energy of the system by minimizing the functional $F_{\mathrm{G}}[\mathcal{G}]$, and the resulting propagator provides the best mean-field description of the full interacting system. In its local minima, $F_{\mathrm{G}}[\mathcal{G}]$ satisfies the saddle point equation

$$\frac{\delta F_{\mathrm{G}}}{\delta \mathcal{G}(1,2)} = 0. \tag{4.24}$$

As we discuss in Appendix B.3, this equation is equivalent to the self-consistent EOM equations, Eqs. (4.7, 4.8, 4.9), and (4.13). In particular, the saddle point equation requires $\mathcal{G}^{-1}$ to be local

$$\mathcal{G}^{-1}(1,2) = \delta^{(4)}(x_1 - x_2) \, \mathbf{G}^{-1}(x_2), \tag{4.25}$$

with the matrix $\mathbf{G}^{-1}$ being just the inverse propagator Eq. (4.6) in real space,

$$-\mathbf{G}^{-1} = \partial_{\tau_2} + \begin{pmatrix} \mathcal{H}_0(\mathbf{r}_2) - \mathbf{M} & \boldsymbol{\Delta} \\ \boldsymbol{\Delta}^{+} & -(\mathcal{H}_0(\mathbf{r}_2) - \mathbf{M})^{*} \end{pmatrix}. \tag{4.26}$$

Furthermore, the order parameters $\mathbf{M}$ and $\boldsymbol{\Delta}$ are determined by the former equations of the EOM method, Eqs. (4.8,4.9). We thus find, that the Gaussian variational approach is *entirely consistent* with the EOM method.

[8] The choice (4.23) automatically fixes a certain ambiguity in the definition of $\mathcal{G}^{-1}$, as we discuss in Appendix B.3.

Since in the minima of the Gaussian free energy functional, it is sufficient to consider only local actions $S_{\mathcal{G}}$, we can express the Gaussian free energy in terms of a quadratic Hamiltonian

$$H_{\mathcal{G}}(\mathbf{M},\boldsymbol{\Delta}) \equiv \frac{1}{2}\int \mathrm{d}^3 r \; : \Phi^\dagger \begin{pmatrix} \mathcal{H}_0 - \mathbf{M} & \boldsymbol{\Delta} \\ \boldsymbol{\Delta}^+ & -(\mathcal{H}_0 - \mathbf{M})^* \end{pmatrix} \Phi : , \tag{4.27}$$

expressed in terms of the Nambu fields in Eq. (4.4) and with the semi-colons denoting normal ordering.[9] In terms of the Hamiltonian, Eq. (4.27), the free energy functional takes on the simple form

$$F_{\mathrm{G}}(\mathbf{M},\boldsymbol{\Delta}) = -k_B T \, \log \mathcal{Z}_{\mathcal{G}} + \langle H - H_{\mathcal{G}} \rangle_{\mathcal{G}} \; , \tag{4.28}$$

where H denotes the full Hamiltonian of the system, Eq. (4.3), and the partition function and thermal averages are given by

$$\begin{aligned} \mathcal{Z}_{\mathcal{G}} &= \mathrm{Tr}\, e^{-\beta H_{\mathcal{G}}}, \\ \langle \ldots \rangle_{\mathcal{G}} &= \mathrm{Tr}\, \left(\ldots e^{-\beta H_{\mathcal{G}}} \right) / \mathcal{Z}_{\mathcal{G}} \, , \end{aligned}$$

with the inverse temperature $\beta = 1/(k_B T)$. This Hamiltonian approach allows us to simply evaluate Eq. (4.28) using Wick's theorem (see Appendix B.4), and we find that the free energy density is given by

$$\begin{aligned} f_{\mathrm{G}}(\mathbf{M},\boldsymbol{\Delta}) = & \frac{1}{2}\int \mathrm{d}\epsilon \, \rho(\epsilon) \Big[\mathrm{Tr}(\epsilon - \mathbf{M}) - k_B T \, \mathrm{Tr} \log\Big(2\cosh\left(\beta \, \boldsymbol{\Xi}(\epsilon)/2\right)\Big)\Big] \\ & + \sum_{\alpha\beta} \Big[(M_{\alpha\beta} - \mu_\alpha \delta_{\alpha\beta}) n_{\alpha\beta} + \frac{g_{\alpha\beta}}{2} \left(|n_{\alpha\beta}|^2 - n_{\alpha\alpha} n_{\beta\beta} \right) \Big] \\ & + \sum_{\alpha\beta} \frac{1}{2} \Big[\Delta_{\alpha\beta} d^*_{\alpha\beta} + \Delta^*_{\alpha\beta} d_{\alpha\beta} - g_{\alpha\beta} |d_{\alpha\beta}|^2 \Big], \end{aligned} \tag{4.29}$$

where the densities $\mathbf{n}$ and $\mathbf{d}$ are determined by Eq. (4.13), and the matrix $\boldsymbol{\Xi}(\epsilon)$ is defined in Eq. (4.7). Despite its complicated looking structure, the mean-field free energy provides a useful way to analyze the low energy phase diagram numerically. Although in the local minima of the free energy functional f_{G}, the order parameters $\mathbf{M}$ and $\boldsymbol{\Delta}$ fulfill the EOM self-consistency equations, we did not enforce this constraint in our numerical calculations.[10] Instead, we performed a Monte Carlo method (simulated annealing) to find the absolute minimum of $f_{\mathrm{G}}(\mathbf{M}, \boldsymbol{\Delta})$ in the 15 dimensional parameter space of the order parameters $\mathbf{M}$ and $\boldsymbol{\Delta}$.[11]

[9] Since the functional integral is, by definition, normal ordered, the Hamiltonian $H_{\mathcal{G}}$ also needs to be normal ordered. We verified that this normal ordering indeed provides the correct densities at the free energy minima.

[10] We have nevertheless checked numerically, that the order parameters at these minima indeed satisfy the EOM self-consistency equations.

[11] Both the numerical evaluation routines of Eq. (4.29) and the Monte Carlo program were written by the author, and both required extensive numerical optimization to achieve the required speed and accuracy.

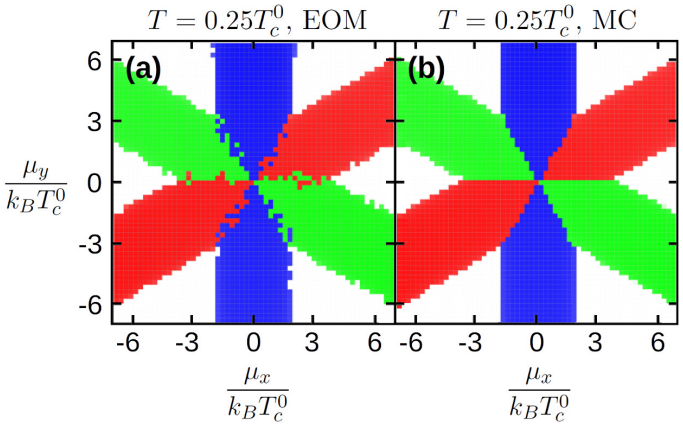

Figure 4.3: Comparison of the EOM (**a**) and the Gaussian variational methods (**b**) at low temperatures, where the SC-normal transition is of first order. Here, the EOM equations exhibit multiple solutions and thus becomes unreliable close to the phase boundaries, whereas Monte Carlo minimization of the free energy accurately finds the physically relevant phases. [Parameters at the $SU(3)$ symmetric point ($\mu_1 = \mu_2 = \mu_3$): $g\,\rho_F = 0.224$, $\eta\,\Lambda = 0.5$, $k_B T_c^0/\Lambda = 0.011, \epsilon_F/\Lambda = 0.24$ (half-filling).]

Fig. 4.3 compares the results of the EOM method with those of the Monte Carlo minimization. At low temperatures, the EOM solutions get stuck in metastable local minima of the free energy near the first order SC-normal phase boundaries, whereas the Monte Carlo routine accurately identifies the physically relevant solutions by converging into the absolute minima of the free energy.

4.3.3 Order parameter symmetries

The $SU(3)$ invariance of the interaction ($g_{\alpha\beta} = g$ for $\alpha \neq \beta$) leads to important consequences for the structure of the phase diagram, and it also determines the nature of the coupling of the superconducting and magnetic order (see Secs. 4.5 and 4.6). In the special case when all chemical potentials are equal (the $SU(3)$ symmetric point of the phase diagram), the Hamiltonian is invariant under global $SU(3)$ rotations, $\Psi_\alpha(x) \mapsto \sum_\beta U_{\alpha\beta}\Psi_\beta(x)$, and a global U(1) gauge transformation, $\Psi_\alpha(x) \mapsto e^{i\varphi}\,\Psi_\alpha(x)$. The transformation properties of the fields also determine those of the order parameters. The densities $\mathbf{n}$ and matrix of renormalized chemical potentials (ferromagnetic order parameter) $\mathbf{M}$ are Hermitian, and they are both invariant to $U(1)$ phase shifts, whereas they transform under $SU(3)$ rotations according to the adjoint representation

$$\mathbf{n}^{\mathrm{T}} \to \mathbf{U}\,\mathbf{n}^{\mathrm{T}}\mathbf{U}^\dagger, \qquad \mathbf{M} \to \mathbf{U}\,\mathbf{M}\mathbf{U}^\dagger, \tag{4.30}$$

after removing the trivial trace. The anomalous densities $\mathbf{d}$ and the SC order parameter $\mathbf{\Delta}$ are, on the other hand, skew-symmetric, and they transform under $U(1)$

phase shifts as $\mathbf{d} \mapsto e^{2i\varphi}\,\mathbf{d}$ and $\mathbf{\Delta} \mapsto e^{2i\varphi}\,\mathbf{\Delta}$. As can be seen from their definitions in Eqs. (4.8,4.11), global $SU(3)$ rotations transform them as

$$\mathbf{d} \to \mathbf{U}\,\mathbf{d}\mathbf{U}^{\mathrm{T}}, \qquad \mathbf{\Delta} \to \mathbf{U}\,\mathbf{\Delta}\mathbf{U}^{\mathrm{T}}, \tag{4.31}$$

corresponding to the conjugate representation of $SU(3)$. Indeed, by introducing the three-component vectors $\underline{d}_\alpha = \frac{1}{2}\sum_{\beta\gamma}\epsilon_{\alpha\beta\gamma}d_{\beta\gamma}$ and $\underline{\Delta} = \frac{1}{2}\sum_{\beta\gamma}\epsilon_{\alpha\beta\gamma}\Delta_{\beta\gamma}$ using the completely antisymmetric Levi-Civita symbol $\epsilon_{\alpha\beta\gamma}$, we can rewrite Eq. (4.31) as

$$\underline{\mathbf{d}} \mapsto\ \mathbf{U}^*\underline{\mathbf{d}}, \qquad \underline{\mathbf{\Delta}} \mapsto \mathbf{U}^*\underline{\mathbf{\Delta}}\ .$$

At the $SU(3)$ symmetric point, the system's Ginzburg-Landau functional must be invariant under the above transformations, Eqs. (4.30, (4.31)), and the U(1) phase rotations. As we discuss in Sec. 4.6, this puts significant restrictions on the possible coupling terms between superconductivity and magnetism, and on their coupling to chemical potential differences. At the onset of superconductivity, the above $SU(3)\otimes U(1)$ symmetry spontaneously breaks down to $SU(2)\otimes U(1)$, leading to the emergence of five Goldstone modes [123].

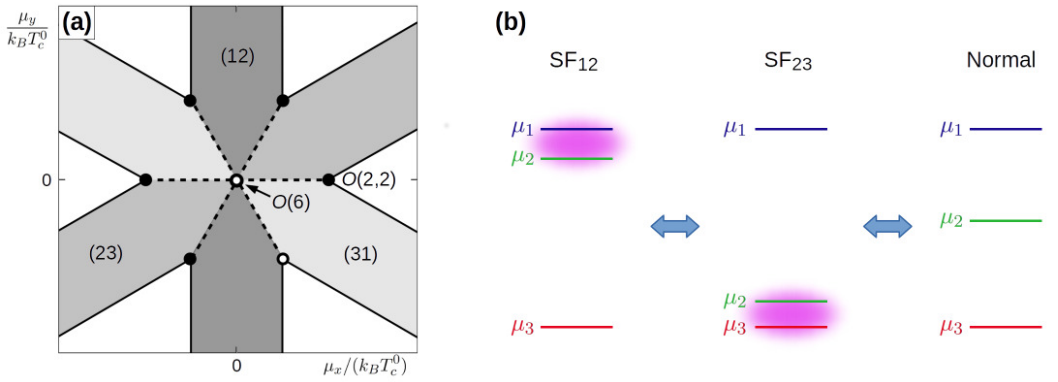

Figure 4.4: Schematic phase diagram at particle-hole symmetry: constant density of states ($\eta = 0$) and half-filling ($\mu_1 + \mu_2 + \mu_3 = 0$). (**a**) SC order always forms in one of the three channels (12), (23) or (31) (gray regions), separated by first order phase boundaries (dashed lines). Large enough chemical potential differences drive system into the normal phase (white), through the SC-normal phase transition (full line), that is of second order at temperatures $T \lesssim T_c^0$, whereas it becomes of first order at low temperatures. At the $SU(3)$ symmetric point, $\mu_x = \mu_y = 0$, (full circle) the transition is described by an $O(6)$ critical theory, whereas the phase boundaries between different SC phases terminate in second order critical points with special $O(2,2)$ symmetry (empty circles), as discussed in Sec. 4.4.1. (**b**) Mechanism of the phase transitions. SC order is formed between species with the closest chemical potentials, whereas higher imbalances drive the system into the normal state (N).

4.4 Mean-field phase diagram

Before analyzing our mean-field results of the global phase diagram, let us first sketch the phase diagram of the three-component mixture based on some simple physical considerations. Similar to the BCS theory of two-component superconductivity, one finds that the critical temperature at the $SU(3)$ symmetric point ($\mu_1 = \mu_2 = \mu_3$) is given by

$$k_B T_c^0 \approx \frac{2e^{\gamma_E}}{\pi} \Lambda \, e^{-1/(g\rho_F)} \ll \Lambda, \tag{4.32}$$

with $\gamma_E \approx 0.577$ denoting Euler's constant [96]. In the weakly coupled regime, the phase diagram is expected to become universal in case of $SU(3)$ symmetrical interactions, and depend only on the dimensionless temperature, T/T_c^0, the dimensionless chemical potential shifts, $\delta\mu_\alpha/(k_B T_c^0)$, and the dimensionless particle-hole symmetry breaking parameter[12], $\eta \, k_B T_c^0$.

The corresponding schematic phase diagram in case of a particle-hole symmetric situation, $\eta = 0$, is shown in Fig. 4.4 (a), as a function of the chemical potential differences,

$$\begin{aligned} \mu_x &\equiv (\mu_1 - \mu_2)/\sqrt{2} \, , \\ \mu_y &\equiv (\mu_1 + \mu_2 - 2\mu_3)/\sqrt{6} \, , \end{aligned}$$

for a fixed temperature $T < T_c^0$. Pairing in the three-component mixture is similar to that of two-component SC (see Ref. [117]): to enable Cooper pair formation, the Fermi surfaces of the two paired species must be aligned. Pairing results in a condensation energy gain, whereas the shift of the Fermi surfaces results in a kinetic energy loss, which is minimal if components with the smallest chemical potential difference pair up, as indicated in Fig. 4.4 (b). This leads to the characteristic ray-like structure of the phase diagram. In the various gray regions two species of the smallest chemical potential difference pair up to form a SC state, while the third species remains gapless. Furthermore, as we discuss in Section 4.5, the high ("hexagonal") symmetry of the figure is a direct fingerprint of the $SU(3)$ symmetrical interaction, and a discrete particle hole symmetry. Similar to the case of a two-component mixture, discussed in the previous section, the superconducting state is destroyed once all chemical potential differences become large compared to the condensation energy, and the system goes into the normal phase (white region). Close to T_c^0 these SC-normal transitions are of second order (black lines). However, at lower temperatures, they become of first order, just like in case of a two component mixture [117]. However, the transition between *different* SC phases, along the lines

[12] Although, strictly speaking, the mean-field equations in the $\eta = 0$ case are particle-hole symmetric only at half-filling, it holds as an approximate symmetry in a wide range of equal chemical potentials, $\mu_\alpha \equiv \bar{\mu}$, as long as the critical temperature T_c^0, determining the energy range of BCS pairing, is much smaller than the bandwidth, Λ (see Sec. 4.5). Thus, the average of the chemical potentials $\bar{\mu} \equiv (\mu_1 + \mu_2 + \mu_3)/3$ does not have a considerable effect on the phase diagram, which is solely determined by the chemical potential differences. On the other hand, by introducing a non-zero slope of the density of states, $\eta \neq 0$, this approximate particle-hole symmetry is broken.

where the chemical potential differences between two different pairs of fermions become equal, is of first order at all temperatures.

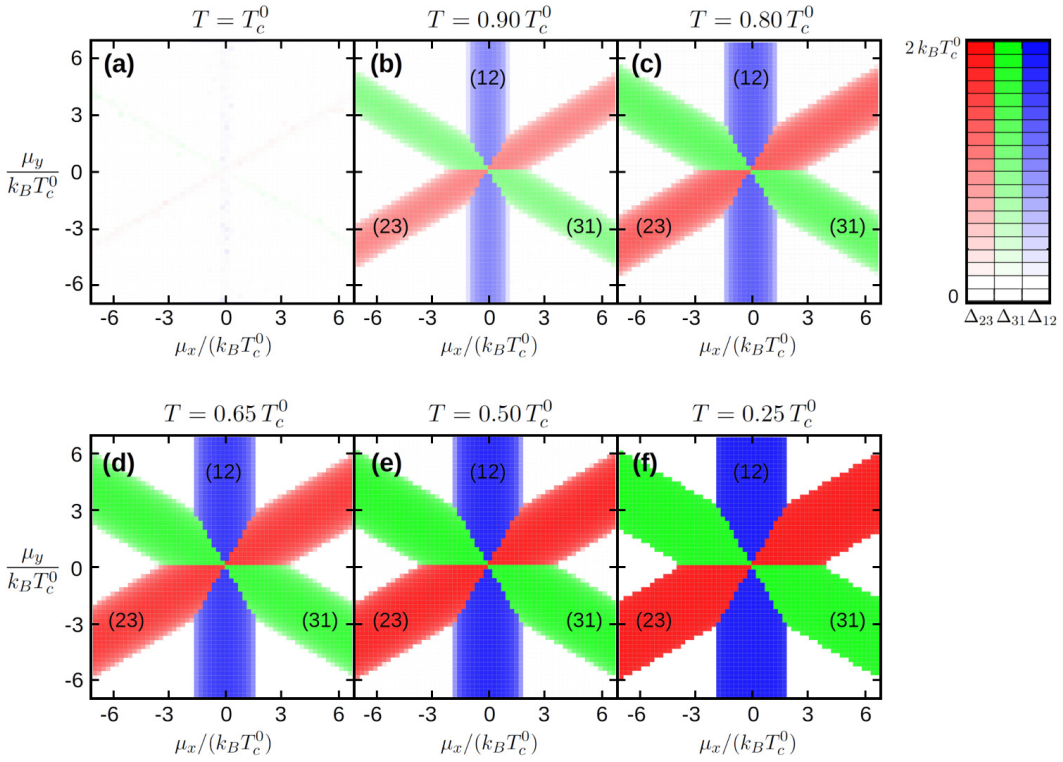

Figure 4.5: Phase diagrams at particle-hole symmetry. At $T = 0.25\,T_c^0$ the SC-normal transition is of first order, whereas it is of second order above the Sarma temperature, Eq. (4.33). The SC-SC boundaries are of first order at all temperatures. The color code (right) indicates the absolute values of the SC order parameters. [Parameters: identical to those in Fig. 4.6.]

The numerically obtained phase diagrams at particle-hole symmetry ($\eta = 0$) are shown in Fig. 4.5 at a series of temperatures, exhibiting sixfold rotational symmetry and a similar structure to the schematic phase diagram Fig. 4.4. The chemical potential driven SC-normal transition is indeed found to be of second order above the Sarma temperature,

$$T^{\mathrm{Sarma}} \approx 0.48\,T_c^0, \tag{4.33}$$

whereas it becomes of first order at lower temperatures (see Sec. 4.4.3).

The numerically computed SC-normal phase boundaries are shown in Fig. 4.6. The volume below the dome-like structures are occupied by SC phases, with the different colors indicating the different SC channels (12), (23) and (31). The horizontal dashed lines indicate the Sarma temperatures.

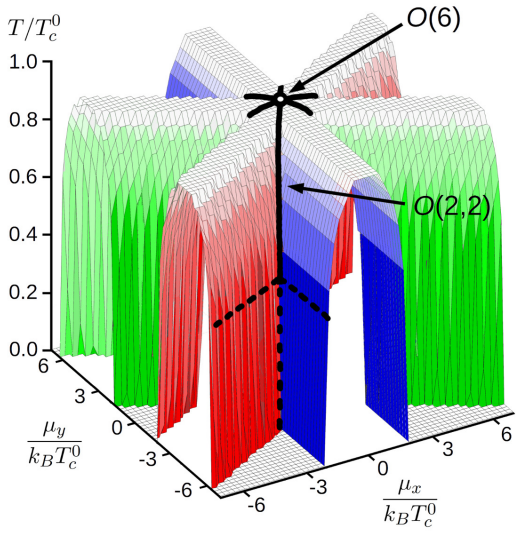

Figure 4.6: Critical temperatures of the SC-normal transition. The Sarma temperatures, below which the transition is of first order, are denoted by the horizontal dashed lines. Full lines indicate points with special $O(2,2)$ universality class, whereas the $SU(3)$ symmetrical point is described by an $O(6)$ critical theory (see Sec. 4.4.1). [Parameters: $g\,\rho_F = 0.2$, and $\eta = \epsilon_F = 0$, corresponding to $k_B T_c^0/\Lambda = 0.0076$.]

4.4.1 Special points in the phase diagram

Although we focus on the mean-field aspects of the three-component system in the body of this chapter, we note in passing that the phase diagram in Figs. 4.4 (a) and 4.6 exhibit interesting critical points with special symmetry. In the vicinity of these points, thermal fluctuations not only suppress the transition temperatures somewhat, but they also modify the SC-normal phase boundaries, and determine the critical exponents associated with the phase transitions. In superfluids and superconductors traditionally studied in condensed matter systems, such fluctuation effects are typically hard to investigate experimentally, whereas this non-trivial behavior may be observable in ultracold experiments [17].

In particular, at the $\mu_x = \mu_y = 0$ point, the Hamiltonian is $SU(3)$ symmetrical, and correspondingly, the phase transition at $T = T_c^0$ is described by an $O(6)$ critical theory, where the six components of the order parameter correspond to the real and imaginary parts of the SC order parameters. In three dimensions, this symmetry is spontaneously broken for $T < T_c^0$, leading to a number of Goldstone modes [123, 125]. In two spatial dimensions, thermal fluctuations in this special point completely destroy the SC order, whereas the rest of the SC phases exhibits Berezinskii–Kosterlitz–Thouless-type behavior [126].

The special point at the ends of the first order SC-SC phase boundaries, indicated by white circles in Fig. 4.4, is even more interesting. Here, the fluctuations of the two competing superconducting order parameters most likely leads to an

$O(2,2) = (O(2) \times O(2)) \rtimes \mathbb{Z}_2$ critical theory. Although this model has been studied extensively [127], even up to six-loop ε-expansion and various other techniques, the stability of its various fixed points is still debated [128–132]. However, since the nature of the fixed point determines the shape of the SC-normal phase boundaries in the vicinity of the critical point, future ultracold atomic experiments may provide a way to determine the stability problems of these fixed points through an experiment [133].

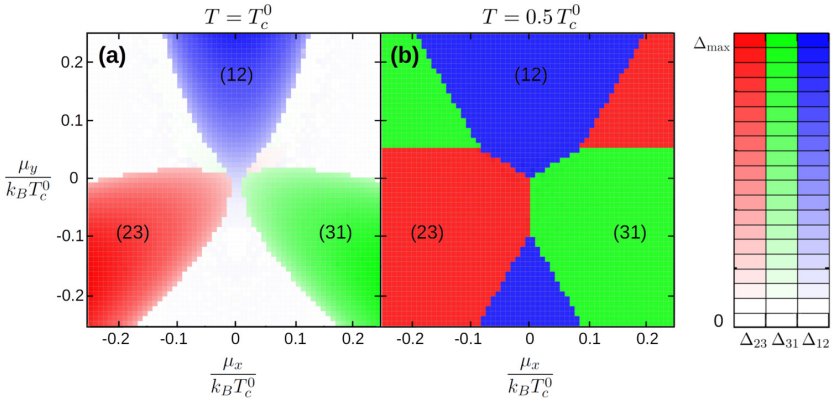

Figure 4.7: Central region of the SC phase diagram in case of particle-hole asymmetry ($\eta \neq 0$), at temperatures (**a**) $T = T_c^0$ and (**b**) $T = 0.5\,T_c^0$. The slope of the DOS leads to a new pairing mechanism near the $SU(3)$ symmetric point, and breaks the hexagonal symmetry of the phase diagram in Fig. 4.4, to a threefold symmetry. Values of $|\Delta_{\alpha\beta}|$ are indicated by the color code on the right, with $\Delta_{\max} = 0.14\,k_B T_c^0$ and $\Delta_{\max} = 2\,k_B T_c^0$, in case of (**a**) and (**b**), respectively. [Parameters: identical to those in Fig. 4.3.]

4.4.2 Effects of particle-hole symmetry breaking

Particle-hole symmetry breaking,[13] $\eta \neq 0$, leads to further complications of the rich SC phase diagram. Although on a large scale, the phase diagram appears to be rather similar to the one of the particle-hole symmetric case, shown in Fig. 4.4, a closer look at the vicinity of the $SU(3)$ symmetric point reveals significant differences, presented in Fig. 4.7, showing the central region of the phase diagram at temperatures $T = T_c^0$ and $T = 0.5\,T_c^0$. Apparently, particle-hole symmetry breaking reduces the hexagonal symmetry of the phase diagram to a 'trigonal' symmetry, associated with the permutation symmetry of the particle species ($1 \leftrightarrow 2 \leftrightarrow 3$), due to the $SU(3)$ symmetry of the interaction [106]. In simple physical terms, the change in the phase diagram can be understood as follows: since the superconducting gap,

[13] Particle-hole symmetry can be broken in many other ways, too (e.g. by introducing an asymmetrical cut-off, $\hbar\omega_{D\pm}$). However, in the weak coupling regime, the non-vanishing slope of the DOS seems to have the largest impact.

and thus the gain in condensation energy depends sensitively[14] on the value of the DOS at the Fermi energy [96], Cooper pairs may not necessarily form in channels of the smallest chemical potential difference, but between those species, that have higher density of states. In particular, the diagram at $T = T_c^0$ clearly represents that the ciritcal temperature can indeed be increased by shifting the Fermi energy to higher DOS. One can thus induce superconductivity even at temperatures above T_c^0 by creating an appropriate chemical potential imbalance, see Fig. 4.9.

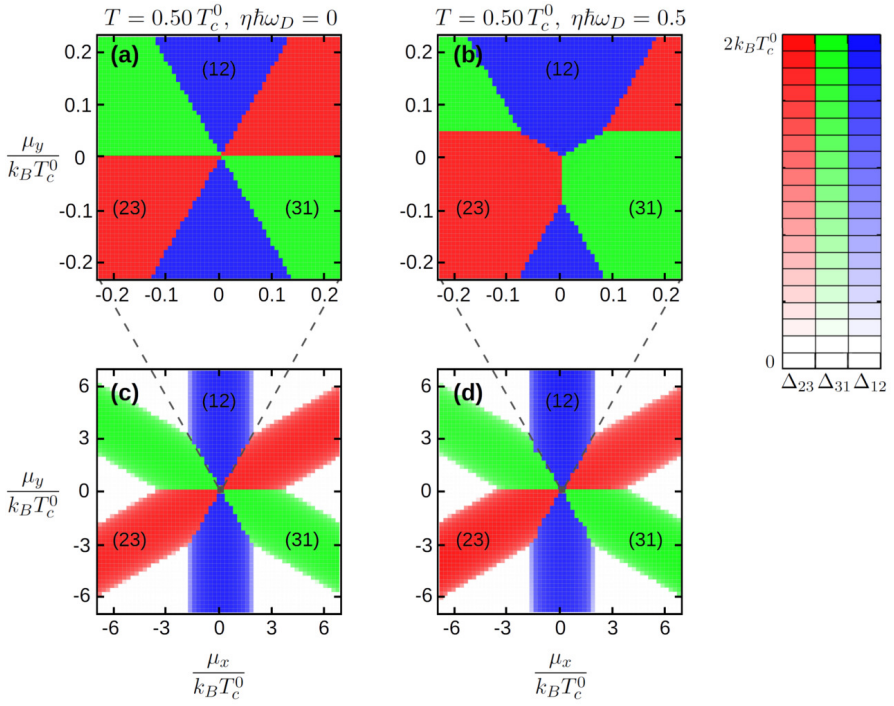

Figure 4.8: Comparison of the particle-hole symmetric (**a**, **c**) and asymmetric case (**b**, **d**) at temperatures $T = 0.5\,T_c^0$. Whereas the large scale phase diagrams (**c**, **d**) are identical at first sight, a closer look reveals qualitative differences near the $SU(3)$ symmetric point (**a**, **b**). The color code (right) indicates the absolute values of the SC order parameters. [Parameters at the $SU(3)$ symmetric point: $(g\,\rho_F,\ k_BT_c^0/\Lambda,\ \eta\,\Lambda, \epsilon_F/\Lambda) = (0.2, 0.0076, 0, 0)$ in (**a**, **c**) and $(0.224, 0.011, 0.5, 0.24)$ in (**b**, **d**).

It is important to note, however, that this central region of the phase diagram, affected by even a large particle-hole asymmetry is typically small compared to the rest of the phase diagram in the weak coupling regime $k_BT_c^0 \ll \Lambda$ (see Fig. 4.8). Based on our numerical simulations at higher interaction strengths [133] the relative size of this threefold symmetric region seems to scale roughly as $\sim \sqrt{\eta\,(k_BT_c^0)}$, and

[14] The standard BCS approximation for T_c^0 in the weak coupling regime can be simply generalized to the case linear DOS $k_B\ T_c^0\ \approx\ 1.13\ \sqrt{\Lambda^2 - \epsilon_F^2}\ e^{-1/(g\rho_F)}\ e^{-(\rho_F-\rho_0)/\rho_F}$.

it is thus expected to become more extended in the strongly interacting regime.

Fig. 4.9 shows the numerically computed phase diagram at the critical temperature at the $SU(3)$ symmetric point, $T = T_c^0$. Since the species forming the SC can increase their condensation energy in certain directions in the phase diagram, where they can gain a higher DOS at their Fermi energies, superconductivity appears in small regions near these lines, even at $T = T_c^0$.

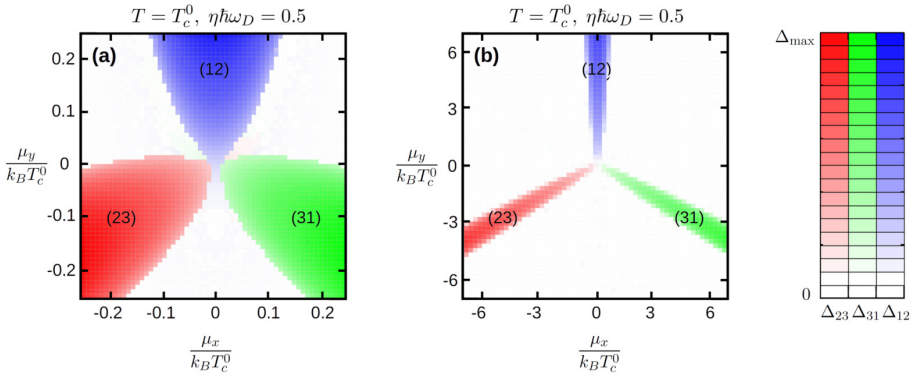

Figure 4.9: $T = T_c^0$ phase diagram at particle-hole symmetry breaking, $\eta\,\Lambda = 0.5$. In certain directions, the elevated density of states of two components with nearly equal chemical potentials favors SC pairing, and the critical temperature exceeds T_c^0. The color code indicates the absolute values of the SC order parameters, with $\Delta_{\max} = 0.14\,k_B T_c^0$ in (**a**), and $2k_B T_c^0$ in (**b**). [Parameters: identical to those in Fig. 4.3.]

4.4.3 Two-component superconductivity

If the chemical potentials of two components is roughly equal, $|\mu_1 - \mu_2| \lesssim T_c^0$, whereas that of the third component is far away from them, ($|\mu_3 - \mu_1|$, $|\mu_3 - \mu_2| \gg k_B T_c^0$), we effectively get a situation with two-component BCS pairing, in the presence of a non-gapped third species. It is thus instructive to compare our results in this regime to two-species BCS results. In order to investigate this limit, we fix the chemical potential difference μ_y at a value $\mu_y = 5\,k_B T_c^0$, and vary μ_x on a much smaller scale, as depicted by the solid line in Fig. 4.10 (a). The resulting phase diagram displays features similar to those predicted by Sarma in case of two-component pairing (see Sec. 4.1). Fig. 4.10 (b) shows the numerically obtained values of the SC order parameter Δ. At zero temperature, it is in full agreement with the BCS result,

$$\Delta(T = 0) = 1.764\,k_B T_c^*, \tag{4.34}$$

with $T_c^* = 1.027 T_c^0$ denoting the critical temperature at the $\mu_x = 0$ point, and it is independent of μ_x.[15] The SC-normal phase transition is of second order in the

[15] Note that, if the slope of the DOS η is non-zero, then T_c^* is shifted upwards from T_c^0 for a positive μ_y, while it is slightly below T_c^0 for a negative μ_y.

$T \lesssim T_c^0$ region, indicated by a continuous line, where Δ depletes in a continuous manner. Below the Sarma temperature, T^{Sarma}, however, the transition becomes of first order (dashed line), and Δ exhibits a jump at the transition [117]. This line terminates at the critical temperature μ_x^{Clog} of the SC-normal transition at zero temperature, the so-called Clogston limit, discussed in Sec. 4.1. Although the numerical value of μ_x^{Clog} seems to be shifted from that found by Sarma, Eq. (4.2), we find the same deviation *both* for two-component and three-component systems. This indicates that this difference is due to the inclusion of magnetic degrees of freedom in our mean-field free energy, Eq. (4.29), that account for interaction-related corrections to the Pauli susceptibility, $\chi \sim \rho_F$, neglected in Sarma's work [117, 133].

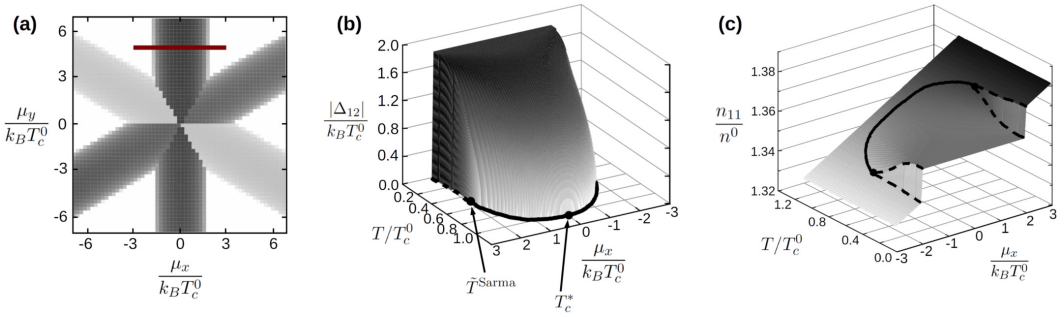

Figure 4.10: Two-particle SC phase diagram with μ_y kept fixed at $\mu_y = 5\, k_B T_c^0$, as indicated by the red line in (**a**). (**b**) The SC-normal transition is of second order at higher temperatures (solid line), with a continuously vanishing SC order parameter, whereas Δ_{12} jumps discontinuously below the Sarma temperature, T^{Sarma}. (**c**) The particle densities exhibit a similar jump at the first order phase boundary. [Parameters at the $SU(3)$ symmetric point: $g\,\rho_F = 0.2$, $\epsilon_F = 0$, $\eta\,\Lambda = 0.5$, and $k_B T_c^0/\Lambda = 0.0076$.]

Fig. 4.10 (c) displays the change in the particle densities across the SC phase diagram. At zero temperature, the SC state is non-polarizable: the Fermi surfaces of the two components are bound together, and the values of the densities do not depend on the chemical potential difference μ_x. Thus, at the SC-normal phase boundary, the densities shift abruptly, leading to an experimentally important manifestation of the phase transition[16] [111]. This shift remains discontinuous, and thus the phase transitions is of first order up to temperatures below $T^{\,\mathrm{Sarma}}$.

4.5 Symmetries of the phase diagram

Let us now discuss the effect of the $SU(3)$ symmetry of interactions on the structure of the phase diagram. Away from the $SU(3)$ symmetric point, where the chemical

[16] Although this jump is only of $\sim 1\%$ in the densities in Fig. 4.10, it is expected to take on much higher values in the strongly interacting regime (see Ref. [111]).

potential differences are non-zero, we still find significant symmetry-dictated restrictions on the possible phases of the system, as well as on the symmetries of the phase diagram. Even at the break-down of the $SU(3)$ symmetry of the interactions, the $SU(3)$ invariance of the functional integral measure in Eq. (4.15) leads to Ward identities [106] that connect the particle densities to four-point expectation values

$$(\mu_\alpha - \mu_\beta)\, n_{\alpha\beta} = \sum_\gamma (g_{\beta\gamma} - g_{\alpha\gamma}) \left\langle \Psi_\gamma^\dagger \Psi_\alpha^\dagger \Psi_\beta \Psi_\gamma \right\rangle ., \tag{4.35}$$

as we show in Appendix B.1. Since the right hand side of this equation for $SU(3)$ symmetric interactions is zero, we find that $\mathbf{n}$ (and thus $\mathbf{M}$ as well) is diagonal. We note, that a similar Ward identity can be derived within the framework of the Gaussian variational method, leading to the same conclusions (see Appendix B.2).

Similar to the order parameter $\mathbf{M}$, the matrix of (bare) chemical potentials, $\hat{\mu}$, also transforms according the adjoint representation of $SU(3)$ matrices. However, in experimental situations, $\hat{\mu}$ is diagonal, and we can restrict our investigations to this case, where $SU(3)$ transformations simply generate permutations of the hyperfine components α, and the corresponding chemical potentials, μ_α. In the (μ_x, μ_y) plane, these permutations translate to threefold rotations and reflections, and give a two-dimensional representation of the $\mathbb{S}_3 \sim C_{3v}$ group. This implies a *trigonal* symmetry of the phase diagram, see Fig. 4.8 (b) and Fig. 4.9.

In addition, in case of $SU(3)$ symmetric interactions, the EOM equations and the free energy, Eq. (4.29), obey an additional *particle-hole symmetry*, if the single particle DOS in the band is symmetric $\rho(\epsilon) = \rho(-\epsilon)$, and the band is exactly half-filled (see Appendix B.5). In this case the phase diagram Fig. 4.4 has an additional mirror symmetry, since the particle-hole transformation $(\mu_x, \mu_y) \to -(\mu_x, \mu_y)$ leaves the order parameters invariant, apart from signs, global phase rotations, and conjugation. This inversion symmetry, together with the formerly discussed $\mathbb{S}_3$ symmetry leads to a *sixfold* C_{6v} *symmetry* in the $(\delta\mu_x, \delta\mu_y)$ plane. Although exact particle-hole symmetry holds only in case of half-filling, we found in our numerical investigations that in the weak coupling regime, $k_B T_c^0 \ll \Lambda$, the mean-field free energy is sensitive only to the immediate vicinity of the Fermi surface. Therefore, particle-hole symmetry becomes an *approximate symmetry* to a good accuracy in a wide range of average chemical potentials $\overline{\mu} = (\mu_1 + \mu_2 + \mu_3)/3$, whenever the single particle DOS is constant, $\eta \equiv 0$. We thus find a phase diagram of hexagonal symmetry within our numerical accuracy, as we showed in Fig. 4.5.

4.6 Ginzburg–Landau free-energy

Many of the interesting features of the phase diagram can be captured through a Ginzburg–Landau approach incorporating both $\mathbf{\Delta}$ and $\mathbf{M}$ as order parameters. In this section, we thus analyze the central region of the phase diagram at temperatures $T \sim T_c^0$, and identify the terms in the free energy that are responsible for the symmetries of this region. As we mentioned in Sec. 4.3.3, the $SU(3)$ transformation

properties of the order parameters put significant constraints on the number of possible terms in the expansion. Their coefficients depend on microscopic parameters, we shall determine numerically from the mean-field free-energy Eq. (4.29).

In the weak coupling limit, $k_B T_c^0 \ll \Lambda$, the dimensionless free energy,

$$\tilde{f}_G \equiv \frac{f_G}{\rho_F \, (k_B T_c^0)^2} \, , \tag{4.36}$$

can be expanded near the $SU(3)$ symmetric point in terms of the dimensionless order parameters

$$\tilde{\mathbf{\Delta}} \equiv \frac{\mathbf{\Delta}}{k_B T_c^0}, \qquad \delta\tilde{\mathbf{M}} \equiv \frac{\mathbf{M} - \mathbf{M}^0}{k_B T_c^0} \, ,$$

and the dimensionless matrix of chemical potential differences

$$\delta\tilde{\mu}_{\alpha\beta} \, = \, \delta_{\alpha\beta} \, \frac{\mu_\alpha - \mu^0}{k_B T_c^0} \tag{4.37}$$

with $\mathbf{M}^0$ and μ^0 denoting the renormalized and bare chemical potentials at the $SU(3)$ symmetric point, respectively.[17] Furthermore, the expansion coefficients shall depend only on a few dimensionless parameters: the reduced temperature $t \equiv (T - T_c^0)/T_c^0$, the dimensionless interaction strength, $\tilde{g} \equiv g \, \rho_F$, and the dimensionless slope of the DOS at the Fermi energy $\tilde{\eta} \equiv \eta \, k_B T_c^0$, identified as the particle-hole symmetry breaking parameter. Since all terms in the expansion need to be $SU(3)$ invariant, the number of terms is vastly reduced [106], and thus $\tilde{f}_G$ is given by the series

$$\begin{aligned} \tilde{f}_G(\tilde{\mathbf{\Delta}}, \delta\tilde{\mathbf{M}}) = \, & \frac{A_1}{4} \, \mathrm{Tr}(\tilde{\mathbf{\Delta}}\tilde{\mathbf{\Delta}}^+) + \frac{A_2}{16} \, \mathrm{Tr}((\tilde{\mathbf{\Delta}}\tilde{\mathbf{\Delta}}^+)^2) \\ & + \, B_1 \, \mathrm{Tr}(\delta\tilde{\mathbf{M}}^2) + B_2 \, \mathrm{Tr}(\delta\tilde{\mathbf{M}})^2 + B_3 \, \mathrm{Tr}(\delta\tilde{\mu} \, \delta\tilde{\mathbf{M}}) \\ & + \frac{C_1}{4} \, \mathrm{Tr}(\delta\tilde{\mathbf{M}}\tilde{\mathbf{\Delta}}\tilde{\mathbf{\Delta}}^+) + \frac{C_2}{4} \, \mathrm{Tr}(\delta\tilde{\mathbf{M}}) \mathrm{Tr}(\tilde{\mathbf{\Delta}}\tilde{\mathbf{\Delta}}^+) \\ & + \frac{C_3}{4} \, \mathrm{Tr}(\delta\tilde{\mu}\tilde{\mathbf{\Delta}}\tilde{\mathbf{\Delta}}^+) + \ldots \, . \end{aligned} \tag{4.38}$$

Since near the $SU(3)$ symmetric phase transition the order parameters are of the order of $\delta\tilde{\mathbf{M}} \propto \delta\tilde{\mu}$ and $\tilde{\mathbf{\Delta}} \propto \sqrt{t}$, thus the above expansion contains all terms up to $\mathcal{O}(t^2, \delta\tilde{\mu} \, t, \delta\tilde{\mu}^2)$ order.[18] All of the 8 coefficients are all functions of $\tilde{g}$, t, and $\tilde{\eta}$, and their numerically determined values, obtained by fitting the free energy Eq. (4.29), are given in Table 4.1.

It is instructive to look at the expansion coefficients and uncover the nature of the different terms. The onset of superconductivity is driven by the term $A_1(t)$, which

[17] Since a simultaneous shift of all the chemical potential components shall have no considerable impact on the phase diagram, we restrict ourselves to chemical potentials with $\mathrm{Tr} \, \delta\tilde{\mu} = 0$.

[18] Since the term $(\mathrm{Tr}(\tilde{\mathbf{\Delta}}\tilde{\mathbf{\Delta}}^+))^2$ is proportional to $\mathrm{Tr}((\tilde{\mathbf{\Delta}}\tilde{\mathbf{\Delta}}^+)^2)$, it does not appear in the expansion.

parameter	approximate expression
A_1	$2.00\,t + \ldots$
A_2	$0.40 - 1.20\,t + \ldots$
B_1	$0.5000 + 0.500\,\tilde{g} + \ldots$
B_2	$-0.500\,\tilde{g} + \ldots$
B_3	$-1.000 + \ldots$
C_1	$1.25\,\tilde{\eta} + \ldots$
C_2	$-1.22\,\tilde{\eta} + \ldots$
C_3	$-1.24\,\tilde{\eta}/\tilde{g} + \ldots$

Table 4.1: Approximate expressions of the Ginzburg-Landau coefficients in Eq. (4.38). The dimensionless parameters are $\tilde{g} \equiv \rho_F g$, $\tilde{\eta} \equiv \eta\, k_B T_c^0$, and $t \equiv (T - T_c^0)/T_c^0$.

parameter	approximate expression
a_1	$2.0\,t + \ldots$
a_2	$0.40 - 1.2\,t + \ldots$
b	$\left(3.2\,t - 0.33/\tilde{g}^2\right)\,\tilde{\eta} + \ldots$
c_1	$0.125 - 0.15\,\tilde{g} - 0.13\,t + \ldots$
c_2	$-0.115 + 0.14\,\tilde{g} + 0.12\,t + \ldots$

Table 4.2: Approximate expressions of the Ginzburg-Landau coefficients in Eq. (4.40). The dimensionless parameters are $\tilde{g} \equiv \rho_F g$, $\tilde{\eta} \equiv \eta\, k_B T_c^0$, and $t \equiv (T - T_c^0)/T_c^0$.

changes sign at the critical temperature. This, together with the coefficient $A_2(t)$, determines the value of the SC order parameter Δ at the $SU(3)$ symmetric point. All other coefficients are approximately constant close to the phase transition. Whereas the terms B_i simply set the ferromagnetic susceptibility in the normal phase, the terms C_i are much more interesting: they drive the coupling between the SC order parameter and the magnetization (or chemical potential differences), and produce the density shift of the normal component at the onset of superconductivity [106].[19] This coupling is responsible for the threefold symmetry of the central region of the phase diagram (see Fig. 4.8). Importantly, all of these terms are found to be proportional to the particle-hole symmetry breaking parameter, $\tilde{\eta}$, in accordance with our previous observations, that the threefold symmetric region is characteristic only to the phase diagram of a particle-hole symmetry broken system.

Although the third order expansion above accounts for the threefold symmetric

[19]Note, that in a two-component system, these terms are actually zero, due to the symmetry of the order parameters, and the coupling of superconductivity and magnetism can only appear at higher order in these systems.

region of the phase diagram, it does not recover its sixfold symmetric structure, dominating at larger chemical potential differences. Note that, the hexagonal structure is even, while the terms C_1, C_2 and C_3 are odd under particle-hole transformation, $\delta\tilde{\mu} \leftrightarrow -\delta\tilde{\mu}, \delta\tilde{\mathbf{M}} \leftrightarrow -\delta\tilde{\mathbf{M}}^*$, and are proportional to $\tilde{\eta}$, whereas the hexagonal region dominates the phase diagram already in the particle-hole symmetric system. To cover this region, one obviously needs to go to higher orders in the expansion, and add terms with even powers of $\delta\tilde{\mathbf{M}}$ and $\delta\tilde{\mu}$, coupled to the superconducting order parameter $\tilde{\mathbf{\Delta}}$. Unfortunately, the number of terms already in the next order of the expansion is enormous, and it is thus practically impossible to determine all of their coefficients numerically. However, integrating out the small ferromagnetic response $\delta\tilde{\mathbf{M}}$, we can simply focus on an expansion in terms of the SC order parameter. By minimizing $\tilde{f}_G$ in $\delta\tilde{\mathbf{M}}$ for all fixed values of $\delta\tilde{\mu}$ and $\tilde{\mathbf{\Delta}}$, we can define a new free energy functional,

$$\widehat{f}_G(\delta\tilde{\mu}, \tilde{\mathbf{\Delta}}) \equiv \tilde{f}_G(\delta\tilde{\mu}, \tilde{\mathbf{\Delta}}, \delta\tilde{\mathbf{M}}_{\min}(\delta\tilde{\mu}, \tilde{\mathbf{\Delta}})) \,, \tag{4.39}$$

that is the functional only of the SC order parameter, but nevertheless incorporates the effects of magnetization. Keeping all $SU(3)$ symmetric terms in $\widehat{f}_G$ up to $\mathcal{O}(t^2, \delta\tilde{\mu}^2\, t)$ order, we find

$$\begin{aligned} \widehat{f}_G = {} & \frac{a_1}{4}\,\mathrm{Tr}(\tilde{\mathbf{\Delta}}\tilde{\mathbf{\Delta}}^+) + \frac{a_2}{16}\,\mathrm{Tr}((\tilde{\mathbf{\Delta}}\tilde{\mathbf{\Delta}}^+)^2) + \frac{b}{4}\,\mathrm{Tr}(\delta\tilde{\mu}\tilde{\mathbf{\Delta}}\tilde{\mathbf{\Delta}}^+) \\ & + \frac{c_1}{4}\,\mathrm{Tr}(\delta\tilde{\mu}^2\tilde{\mathbf{\Delta}}\tilde{\mathbf{\Delta}}^+) + \frac{c_2}{4}\,\mathrm{Tr}(\delta\tilde{\mu}\tilde{\mathbf{\Delta}}\delta\tilde{\mu}\tilde{\mathbf{\Delta}}^+) + \dots . \end{aligned} \tag{4.40}$$

The numerically obtained values of these coefficients are shown in Table 4.2. The particle-hole asymmetric term, b, is proportional to $\tilde{\eta}$, and it is responsible for the threefold symmetric structure of the phase diagram. It plays a role similar to the C_i coefficients of the previous expansion, Eq. (4.38). The terms c_1 and c_2, on the other hand, are independent of $\tilde{\eta}$, and they are the lowest order coefficients reproducing the sixfold symmetric structure of the phase diagram. Indeed, numerical minimization of the Eq. (4.40) leads to the correct structure of the phase diagram close to the $SU(3)$ symmetric point, as characterized by the competition between the couplings odd (b, ...) and even (c_1, c_2, ...) under particle-hole symmetry. The expansion also determines the absolute value of the SC order parameter correctly at temperatures $0.9T_c^0 < T < T_c^0$, and in the weak coupling regime $k_B T_c^0/\Lambda < 0.1$. Unfortunately, however, it reproduces the position of the triple points at the interface of the threefold and approximately sixfold symmetric structures in Fig. 4.8 only up to an error of about 50%. Although this is a rather large error, it is not very surprising, since the scale of the threefold symmetric structure is $\delta\tilde{\mu} \approx 0.2$, for the parameters considered here. Thus, $\delta\tilde{\mu}$ cannot be considered as a small parameter, and higher order terms in the expansion seem to become relevant.

4.7 Summary

In this chapter, we studied the rich phase diagram of a three-component fermionic gas, with weakly attractive $SU(3)$ symmetric interactions.[20] By using a combination of an equation of motion based technique and a Gaussian variational method, we were able to capture the interplay of ferromagnetic and superconducting (SC) ordering in an *unbiased* way, and map out the global phase diagram in the entire temperature range. The interplay of the two orders leads to qualitative differences in the vicinity of the $SU(3)$ symmetric point, where all chemical potentials are equal, and they also significantly modify the SC-normal phase boundaries. Similar to two-component gases, chemical potential differences destroy superconductivity though a Zeeman-like mechanism, and the associated phase boundary is of second order above the so-called Sarma temperature, whereas they become of first order at lower temperatures.

We identified the basic physical mechanisms that determine the shape of the phase diagram based on general energy and symmetry arguments, and mapped out the phase diagram numerically, in terms of dimensionless physical parameters. We found that, except for the $SU(3)$ symmetric point, SC order always forms in one of the three channels (12), (23) and (31), and as a rule of thumb, Cooper pairing tends to occur between components of the smallest chemical potential difference. If the density of states near the Fermi energy is approximately constant, the $SU(3)$ symmetry of interactions and the (approximate) particle-hole symmetry leads to a sixfold rotational symmetry of the phase diagram, in the plane of chemical potential differences, (μ_x, μ_y). It is only the central region of the phase diagram, where the coupling between SC and magnetism, triggered by a particle-hole symmetry breaking near the Fermi energy, $\eta \sim \rho'(\epsilon_F)/\rho(\epsilon_F)$, breaks down the rotational symmetry of this central region to a threefold symmetry. Although this region appears only in the small vicinity of the $SU(3)$ symmetric point, its relative size apparently scales as $\sim \sqrt{\eta T_c^0}$, and it is thus expected to become more pronounced in case of strong attractive interactions, $k_B T_c^0 \approx E_F \sim \Lambda$, and may thus become observable in experiments.

Finally, we constructed the Ginzburg–Landau functional associated with the central region of the phase diagram, near the critical temperature, T_c^0. We identified the terms relevant for the trigonal as well as the sixfold symmetric structures of the phase diagram, and identified their coefficients. Importantly, the terms determining the structure of trigonal symmetry, associated with the coupling between the SC and magnetic order (and chemical potentials) are driven by particle-hole symmetry breaking through the parameter η.

Experimentally, gases of $SU(3)$ symmetric interactions could be realizable in the widely used system of ^{6}Li in high magnetic fields, whereas Yb-like closed s-shell atoms, with perfect $SU(N)$ interactions, could provide an alternative realiza-

[20] In an experimental situation of a trapped gas (in the absence of an optical lattice), an appropriate definition of the weak coupling limit is $k_B T_c^0 \ll E_F$, with the Fermi energy, E_F, measured from zero energy.

tion. Although experiments with attractive three-component mixtures are generally plagued by three-particle losses [134–137], the recent experimental realization of Fermi degenerate ^{6}Li mixtures [138] indicates that experiments on intriguing color superconducting phases may be within reach.

5

Stabilizing skyrmions through strong interactions

Certain excitations in ordered media, like vortices in ^{4}He, can be surprisingly long-lived. The mechanism that stabilizes the vortex is that the winding of the condensate phase around the vortex core cannot be removed by the continuous dynamics of the superfluid, and forces the vortex to stay. Similar long-lived excitations, protected by some non-trivial topological winding of the order parameter, are ubiquitous in physics, and are often referred to as *topological excitations*. By considering the order parameter, rather abstractly, as a mapping from spatial points to the order parameter space, one can classify order parameter configurations based on whether they can be deformed into each other by continuous deformations, as described by homotopy theory in mathematics [139, 140]. Most excitations are topologically trivial, i.e. they can be smoothly removed from the system, like the above mentioned plane-wave-like quasi-particle excitation. However, certain systems with special order parameter space structure allow for excitations with topologically non-trivial winding, characterized by especially long lifetimes and exotic properties. Probably the most interesting property of these field configurations is that, in many cases, the topological winding significantly changes the nature and the spectrum of quasi-particle excitations.[1]

Topological excitations in low spatial dimensions have been discovered in several physical settings. The simplest one dimensional topological objects, domain walls,

[1] In quantum field theory, this is commonly referred to as the system being in 'a topologically different vacuum'. Since in the thermodynamic limit, the tunneling amplitude between different topological configurations goes to zero, they can be considered as different ground states or vacua of the system, with quasi-particle excitations of different nature. Probably the simplest example is the Sine–Gordon model, where the presence of solitons modifies the nature of low energy excitations [141].

besides appearing in such diverse fields as solid-state physics, cosmology, string theory [142] and one dimensional quantum field theories, have also found important applications in magnetic hard drives. Vortices and other topological line defects belong to our basic understanding of superfluidity, superconductivity [39, 96, 143] and constitute the basic mechanism behind the Berezinsky-Kosterlitz-Thouless phase transition [15, 16]. Higher dimensional topological excitations are even more interesting and complex. 't Hooft-Polyakov monopoles [144, 145], the non-Abelian counterparts of the well-known Dirac monopole of electromagnetism [146, 147], appear in several grand unified theories of particle physics. *Skyrmions*, another large class of topological excitations are smooth, localized structures of some order parameter vector field. Similarly to vortices, where winding of the phase gives a non-zero topological number, in the skyrmion's case, the order parameter vector field winds over the sphere of unit vectors in order parameter space. Although skyrmions were originally proposed to describe hadronic particles by Skyrme [148, 149], their signatures have been later observed in quantum Hall systems [150–155]. Moreover, a spontaneous formation of skyrmion lattices, displaying the topological Hall effect [156–158], has been reported in certain magnetic materials [159–161].

Individual skyrmions, monopoles and three-dimensional topological excitations in general have, however, been notoriously hard to observe. Indeed, it has been only recently that experiments convincingly demonstrated the existence of monopole-like structures in spin-ice $Dy_2Ti_2O_7$ [162, 163]. The main reason for this difficulty lies in dynamical instability problems of these excitations. In particular, smooth three-dimensional excitations are generally doomed to shrink to a point or expand into infinity, in the absence of non-trivial external gauge fields stabilizing them [164], and the underlying cause of their instability is captured by Derrick's simple argument (see Appendix C.1) [165]. Although this argument, assuming a spatially homogeneous system, does not apply to topological excitations in trapped cold atomic systems, these excitations have another important dynamical instability problem: since they can always decrease the kinetic energy associated with their non-trivial spatial structure by moving them into lower density regions of the trap, they generally slip away from the trap [166]. This so far excluded the possibility of detecting stable individual skyrmions in ultracold gases [166, 167], and only unstable skyrmion configurations have been imprinted and observed [168–171].

In this chapter, we shall discuss how to stabilize skyrmions, both topologically and dynamically in an ultracold atomic setting, through the application of strong interactions. By putting a so-called 'nematic superfluid' of spin-1 bosons, such as ^{23}Na onto a deep optical lattice, a Mott insulator core forms in the middle of the trap, surrounded by a nematic superfluid shell (similarly to the case of single component bosonic superfluids discussed in Sec. 2.7.2). Due to the order parameter structure of the nematic condensate, the closed shell can naturally host a topologically protected skyrmion, anchored by the Mott core in the middle, leading to a skyrmion of extreme stability,[2] see Fig. 5.1. Most importantly, however, the compact geometry

[2] At the temperature scales of current experiments, the Mott core is non-magnetic, and and there

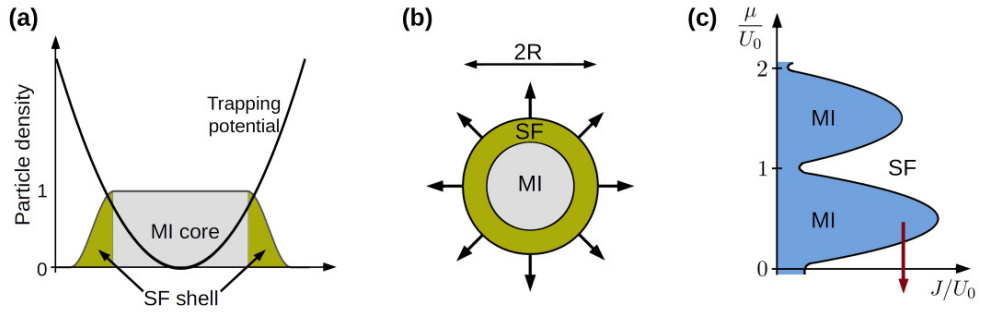

Figure 5.1: Schematic structure of the Mott skyrmion configuration. (**a**) In a deep optical lattice, a Mott insulator core forms in the central region of the trap, with essentially no magnetic ordering at the temperatures considered. The core is surrounded by a nematic superfluid shell of typical radius R, naturally hosting the skyrmion spin structure. Arrows denote the orientation of the nematic order parameter with unit winding over the sphere, $\hat{\mathbf{u}}(\mathbf{r})$ as shown in Eq. (5.1). The skyrmion is stabilized by the Mott core that keeps it from drifting out from the trap. (**b**) Schematic finite temperature phase diagram of strongly interacting bosons in a deep optical lattice, with the blue regions indicating the incompressible Mott insulator phase, with approximately integer number of atoms per site. The red arrow indicates the change of the chemical potential as one moves from the center of the trapped skyrmion towards the edge of the trap.

of this configuration allows for the experimental study of the interplay between the ground state topology and the superfluid excitation spectrum. We will see later in this chapter that the presence of the skyrmion changes drastically the superfluid's excitation spectrum as well as the quantum numbers [172]. The effect of the ground state topology on the excitation spectrum is a general phenomenon, and has been studied theoretically in a large variety of topological excitations. The Mott skyrmion proposal thus provides a unique way to observe this in an experimentally realizable system.

The results presented in this chapter are based on the following publication: M. Kanász-Nagy, B. Dóra, E. A. Demler and G. Zaránd, *"Stabilizing the false vacuum: Mott skyrmions"*, *Sci. Rep.* **5**, 7692 (2015).

5.1 Nematic superfluids

It has been noticed early in the works of Ho [25], and Ohmi and Machida [173] that certain spin $F = 1$ superfluids, such as such as ^{23}Na or ^{87}Rb at zero external magnetic field support magnetic phases [167, 174–180] that can host three-dimensional topologically protected excitations, most importantly, monopole and skyrmion-like defects [166,167,181]. In particular, interactions in a nematic (or antiferromagnetic)

is thus no coupling between the spin configurations of the core and the superfluid.

superfluid such as ^{23}Na, force the superfluid order parameter $\mathbf{\Psi}(\mathbf{r}) = (\Psi_x, \Psi_y, \Psi_z)$ to take on the remarkably simple form,[3]

$$\mathbf{\Psi}(\mathbf{r}) = \hat{\mathbf{u}}(\mathbf{r}) \sqrt{\varrho(\mathbf{r})}\, e^{i\varphi(\mathbf{r})}\,, \tag{5.1}$$

that minimize the interaction energy. Here, $\hat{\mathbf{u}}$ denotes a real unit vector, whereas ϱ and φ are the superfluid density and phase, respectively. The topological structure of the order parameter space can thus be easily determined by looking at Eq. (5.1), as $\left(S^2 \times \mathrm{U}(1)\right)/\mathbb{Z}_2$, where the unit sphere S^2 corresponds to the orientation of the unit vector $\hat{\mathbf{u}}$ whereas the U(1) symmetry is that of the phase variable, φ.[4] The $\mathbb{Z}_2$ factorization is associated with the fact that by simultaneously flipping the orientation of the unit vector and shifting the phase by π is equivalent to the original configuration, $(\hat{\mathbf{u}}, \varphi) = (-\hat{\mathbf{u}}, \varphi + \pi)$ — hence the name 'nematic' condensates. The structure of the order parameter space allows for the existence of two-dimensional skyrmions [171] and three-dimensional monopoles with their order parameter winding around the unit sphere completely, $\hat{\mathbf{u}}(\mathbf{r}) \propto \hat{\mathbf{r}}$ (see Fig. 5.1). This winding cannot be removed by continuous deformations to the order parameter configuration, making the skyrmion topologically protected.

To understand the peculiar order parameter space of nematic condensates, let us first consider the interactions of the spin $F = 1$ bosons[5] in the absence of an optical lattice [25, 173]. The ultracold collisions of these atoms are described by an interaction that is rotationally invariant in spin space. The total spin state of the two atoms is a linear combination of $F = 2$ and $F = 0$ states. Since the s-wave scattering lengths in these two channels, a_2 and a_0, are in general different, the interactions are described by a spin-dependent pseudopotential,

$$V(\mathbf{r})\,\boldsymbol{\psi}(\mathbf{r}) \;=\; \delta^{(3)}(\mathbf{r})\,\frac{\partial}{\partial r}\left(r\,\boldsymbol{\psi}(\mathbf{r})\right)\;\frac{4\pi\hbar^2}{m}\left(a_2\mathbb{P}_2 + a_0\mathbb{P}_0\right),$$

where $\mathbb{P}_F$ denotes projector to the total spin F channel. These projectors can, however be cast into a simple form by making use of the identity $\vec{\mathbf{F}}_1 \cdot \vec{\mathbf{F}}_2 = \mathbb{P}_2 - 2\mathbb{P}_0$ for the spin matrices, $\vec{\mathbf{F}} = (\mathbf{F}_x, \mathbf{F}_y, \mathbf{F}_z)$ [25]. The mean-field interaction energy of a spin-1 superfluid can thus be expressed in terms of the interaction coefficients, $c_0 = \frac{4\pi\hbar^2}{m}(a_0 + 2a_2)/3$ and $c_2 = \frac{4\pi\hbar^2}{m}(a_2 - a_0)/3$, as

$$E_{\mathrm{int}}[\boldsymbol{\phi}] = \int d^3r\,\left[\frac{c_0}{2}\,\rho^2_{\mathrm{MF}}(\mathbf{r}) + \frac{c_2}{2}\,\rho^2_{\mathrm{MF}}\,\vec{f}^{\,2}_{\mathrm{MF}}(\mathbf{r})\right], \tag{5.2}$$

[3] Here, the spinor $\mathbf{\Psi}$ is represented in the rotation matrix basis of $F = 1$ spin matrices, $(F_j)_{\alpha\beta} = -i\,\varepsilon_{j\alpha\beta}$, where ε is the totally antisymmetric Levi-Civita symbol.

[4] Skyrmions can also be susceptible to unwinding, if the interaction energy does not confine the order parameter strongly enough to the space of ground state configurations [169, 170]. This may be the case if the skyrmion's size is too small, and the kinetic energy costs of its non-trivial spatial structure overcomes the interaction energy barrier that keeps the order parameter on the $\left(S^2 \times \mathrm{U}(1)\right)/\mathbb{Z}_2$ subspace.

[5] Besides the spin-1 condensates considered here, higher spin bosons, like ^{85}Rb, ^{133}Cs and the lately created spin-2 condensates of ^{23}Na and ^{87}Rb, have even richer interaction structures and many-body phase diagrams [178, 182].

where the superfluid density and magnetization, $\rho_{\rm MF}(\mathbf{r}) = \sum_\alpha |\phi_\alpha(\mathbf{r})|^2$ and $\vec{f}_{\rm MF}(\mathbf{r}) = \sum_{\alpha\beta} \phi^*_\alpha(\mathbf{r})\, \vec{\mathbf{F}}_{\alpha\beta}\, \phi_\beta(\mathbf{r})/\rho_{\rm MF}(\mathbf{r})$, are determined by the condensate's order parameter, $\phi_\alpha(\mathbf{r})$, with the index α running over the spinor components.

The sign of the spin interaction coefficient c_2 is of crucial importance. In the nematic case, such as for ^{23}Na, when the spin coefficient is positive ($a_2 > a_0$), the interaction energy favors zero magnetization, $\vec{f}_{\rm MF} \equiv 0$. This leads to the ground state configuration space $\left(S^2 \times \mathrm{U}(1)\right)/\mathbb{Z}_2$. Indeed, by choosing the rotation matrix representation for spin matrices $(F_j)_{\alpha\beta} = -i\,\varepsilon_{j\alpha\beta}$, with the totally antisymmetric Levi-Civita symbol, $\varepsilon_{j\alpha\beta}$, the zero magnetization condition implies $\mathrm{Im}\,(\phi^*_\alpha \phi_\beta) = 0$ for all $\alpha, \beta = x, y, z$. Thus, up to a phase factor, the order parameter, $\boldsymbol{\phi}(\mathbf{r})$, is given by a real unit vector. This makes nematic condensates natural candidates for the observation of skyrmions. Ferromagnetic condensates, like ^{87}Rb, on the other hand, have a negative spin coefficients and are therefore fully magnetized, $\vec{f}^{\,2}_{\rm MF} \equiv 1$. Their configuration space is topologically equivalent to the $SO(3)$ rotation group [25], and cannot host monopole-like Mott skyrmion configurations. However, there have been a number of theoretical proposals for other topologically protected excitations in this case [167].

5.2 Lattice model

We shall now study the effects of the optical lattice on the nematic condensate, and how it leads to the formation of a Mott core in the center of the trap. We describe the dynamics of spin $F = 1$ bosons in a deep optical lattice by the Bose–Hubbard Hamiltonian with nearest neighbor hopping, $H = H_{\rm kin} + \sum_{\mathbf{r}} H_{{\rm loc},\mathbf{r}}$ whose kinetic and local parts are defined as

$$H_{\rm kin} = -J \sum_{\langle \mathbf{r},\mathbf{r}'\rangle} b^\dagger_{\mathbf{r}\,\alpha} b_{\mathbf{r}'\alpha}, \tag{5.3a}$$

$$H_{{\rm loc},\mathbf{r}} = -\mu_{\mathbf{r}}\, n_{\mathbf{r}} + \frac{U_0}{2} : n^2_{\mathbf{r}} : + \frac{U_2}{2} : \vec{F}^2_{\mathbf{r}} : \,. \tag{5.3b}$$

Here, the operators $b_{\mathbf{r}\alpha}$ annihilate a boson of spin component α ($\alpha = x, y, z$) at the lattice site $\mathbf{r}$, whereas $: \ldots :$ denotes normal ordering. $n_{\mathbf{r}} = \sum_\alpha b^\dagger_{\mathbf{r}\alpha} b_{\mathbf{r}\alpha}$ and $\vec{F}_{\mathbf{r}} = \sum_{\alpha,\beta} b^\dagger_{\mathbf{r}\alpha} \vec{F}_{\alpha\beta} b_{\mathbf{r}\beta}$ refer to the boson density and the local magnetic moment, respectively. The hopping term sets the energy gain for bosons to tunnel to neighboring sites, whereas the spatially varying chemical potential, $\mu_{\mathbf{r}} \equiv \mu - V(\mathbf{r})$, incorporates the effects of the spherically symmetric trapping potential $V(\mathbf{r}) = m\omega_0^2 \mathbf{r}^2/2$.

The structure of interactions is similar to that in free space, Eq. (5.2), which is the consequence of the $SO(3)$ symmetry of two-particle interactions in parameter space. The on-site charge interaction term U_0 describes the strong repulsion between bosons, confined onto the same lattice site, whereas much weaker spin interaction term U_2 accounts for the magnetic interaction between them. The ratio of these parameters is determined by the scattering lengths, a_2 and a_0, and is dictated by

the same symmetry argument as in Eq. (5.2),

$$\frac{U_2}{U_0} = \frac{a_2 - a_0}{a_0 + 2\,a_2}. \tag{5.4}$$

We will see later in this section that the sign of the spin term determines the ground state order parameter space of the superfluid condensate on the lattice, similarly to the free case, Eq. (5.2). If the spin term is positive, $U_2 > 0$, the interactions force the superfluid order parameter $\Psi_\alpha \propto \langle b_\alpha \rangle$ to stay within the nematic phase, Eq. (5.1), where the mean-field magnetization is zero, $\vec{f_{\mathbf{r}}} \equiv \mathbf{\Psi}^\dagger_{\mathbf{r}} \cdot \vec{\mathbf{F}} \cdot \mathbf{\Psi}_{\mathbf{r}} / |\mathbf{\Psi}_{\mathbf{r}}|^2 \equiv 0$, once the superfluid density $\varrho_r \equiv |\mathbf{\Psi}_{\mathbf{r}}|^2$ is finite. Since, in case of ^{23}Na, these scattering lengths are rather close to each other, the interaction term U_2 is suppressed, and is approximately $U_2 \approx 0.03\,U_0$ (see Refs. [27, 183]). Therefore, the superfluid-Mott phase boundaries are only negligibly modified by the spin interaction, and resembles that of a single-component bosonic lattice, shown in Figs. 2.4 and 5.1 (b).

In what follows, we shall focus on the parameter regime $zJ/U_0 \approx 0.2$ with $z = 6$ the number of nearest neighbors that can be reached easily by increasing the depth of the optical lattice.[6] By squeezing the trap or choosing high enough density, the chemical potential can be increased such that the central region of the trap becomes Mott insulating, surrounded by a nematic superfluid shell, in the outer regions of the trap, where the chemical potential diminishes (shown by red arrow in Fig 5.1 (b)). Following the parameters of the experiment in Ref. [27], in the $zJ/U_0 \approx 0.2$ regime of the phase diagram, the on-site interaction becomes $U_0 \approx 250\,\mathrm{nK}$, setting the values for the spin interaction and the hopping as $U_2 \approx 9\,\mathrm{nK}$, and $zJ \approx 50\,\mathrm{nK}$. In accordance with the temperature range used in current experiments, we assume that the temperature is already low enough ($T < zJ$) that a superfluid around the Mott core can form, with typical radius R, but it is significantly higher than the mean-field magnetic ordering temperature of the Mott insulating core, $T_C \sim 0.1\,T$, with $T_C \sim zJ^2/U_0$. This leads to essentially zero magnetization in the Mott core, therefore the interplay between the magnetism in the Mott core and superfluidity can be ignored.

5.3 Mott skyrmion structure

We shall now develop a mean-field description of the superfluid on the lattice. To identify the skyrmion state in the lattice system at a finite temperature T, we rewrite its thermodynamic partition function, $Z = \mathrm{Tr} e^{-\beta_T (H_{\mathrm{kin}} + \sum_{\mathbf{r}} H_{\mathrm{loc},\mathbf{r}})}$, in the functional integral form $Z = \int \mathcal{D}[b^\dagger, b] e^{-S[b^\dagger, b]}$, where the many-body action is given by [85]

$$S[b^\dagger, b] = \int_0^{\beta_T} d\tau \, \sum_{\mathbf{r}\alpha} b^\dagger_{\mathbf{r}\alpha}\, \partial_\tau b_{\mathbf{r}\alpha} + H_{\mathrm{kin}} + \sum_{\mathbf{r}} H_{\mathrm{loc},\mathbf{r}}, \tag{5.5}$$

[6] The J/U_0 ratio depends exponentially on the lattice depth V_0, $J/U_0 \propto \exp\left(-2\sqrt{V_0/E_R}\right)$, and can thus be easily controlled by modifying the lattice depth to reach the superfluid-Mott insulator transition [27, 177].

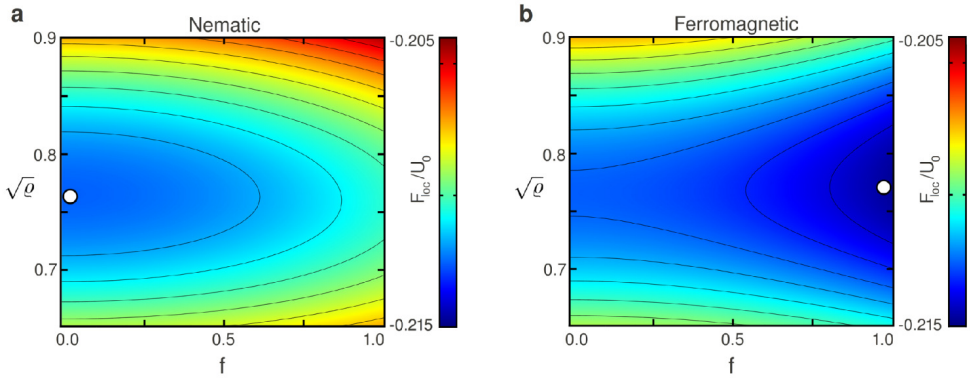

Figure 5.2: The local part $F_{\rm loc}(\varrho, \vec{f}^{\,2})$ of the free energy in Eq. (5.8), in case of (**a**) nematic and (**b**) ferromagnetic interactions, with $U_2 > 0$ and $U_2 < 0$, respectively. The minimum of the free energy (open circle) favors a non-magnetized (fully magnetized) superfluid in the nematic (ferromagnetic) case. [Physical parameters of the plot: $zJ/U_0 = 0.40$, $U_2/U_0 = 0.025$, $T/U_0 = 0.05$, and $\mu/U_0 = 0.08$.]

and $\beta_T = 1/(k_B T)$. In the regime of strong interactions, the kinetic Hamiltonian can be decoupled through a Hubbard–Stratonovich transformation [184] by introducing the superfluid field $\mathbf{\Psi}$, and making use of the identity

$$e^{\sum_{\mathbf{r}\mathbf{r}'} \mathbf{b}^\dagger_{\mathbf{r}} J_{\mathbf{r}\mathbf{r}'} \mathbf{b}_{\mathbf{r}'}} = \int \mathcal{D}[\overline{\mathbf{\Psi}}, \mathbf{\Psi}]\; e^{-\sum_{\mathbf{r}\mathbf{r}'} \overline{\mathbf{\Psi}}_{\mathbf{r}} Jz\, I^{-1}_{\mathbf{r}\mathbf{r}'} \mathbf{\Psi}_{\mathbf{r}'}}\; e^{\sum_{\mathbf{r}} Jz(\mathbf{b}^\dagger_{\mathbf{r}} \mathbf{\Psi}_{\mathbf{r}} + \text{h.c.})}, \tag{5.6}$$

where a vectorial notation has been used for the spin indices, α, and $\overline{\mathbf{\Psi}}$ denotes the conjugate field of $\mathbf{\Psi}$. We also introduced the dimensionless hopping matrix, $I_{\mathbf{r}\mathbf{r}'} = \frac{1}{Jz} J_{\mathbf{r}\mathbf{r}'}$. In the limit of small kinetic energies, as compared to the width of the first Bloch band, its inverse can be written as $I^{-1}_{\mathbf{r}\mathbf{r}'} \approx \delta_{\mathbf{r}\mathbf{r}'} - \frac{a^2}{z} \Delta_{\mathbf{r}\mathbf{r}'}$, with the discrete Laplacian $\Delta_{\mathbf{r}\mathbf{r}'}$ of the lattice model of lattice constant a. Since, the action now contains only local terms in the annihilation operators $b_{\mathbf{r}\alpha}$, these can be integrated out at each site, yielding

$$Z = \int \mathcal{D}[\overline{\mathbf{\Psi}}, \mathbf{\Psi}]\; e^{-\int d\tau\, Jz\, \overline{\mathbf{\Psi}}_{\mathbf{r}} I^{-1}_{\mathbf{r}\mathbf{r}'} \mathbf{\Psi}_{\mathbf{r}'}} \prod_{\mathbf{r}} \mathrm{Tr}_{b_{\mathbf{r}}} e^{-\beta_T \left(H_{\mathrm{loc},\mathbf{r}} - Jz(\mathbf{b}^\dagger_{\mathbf{r}} \mathbf{\Psi}_{\mathbf{r}} + \text{h.c.}) \right)}, \tag{5.7}$$

where the trace goes over the local Hilbert space at site $\mathbf{r}$. In the saddle point approximation, where we neglect the fluctuations of the action around its maximum value, the free energy $F[\mathbf{\Psi}^\dagger, \mathbf{\Psi}] = -k_B T \log Z[\mathbf{\Psi}^\dagger, \mathbf{\Psi}]$ can be written in terms of its kinetic and local parts, $F = F_{\rm kin} + \sum_{\mathbf{r}} F_{\mathrm{loc},\mathbf{r}}$, as

$$F_{\rm kin}\left(\{\mathbf{\Psi}_{\mathbf{r}}\}\right) \;=\; -Ja^2 \sum_{\mathbf{r}\mathbf{r}'} \overline{\mathbf{\Psi}}_{\mathbf{r}}\, \Delta_{\mathbf{r}\mathbf{r}'} \mathbf{\Psi}_{\mathbf{r}'}, \tag{5.8a}$$

$$F_{\rm loc}\left(\varrho_{\mathbf{r}},\, \vec{f}^{\,2}_{\mathbf{r}}, \mu_{\mathbf{r}}, T\right) \;=\; Jz\, \varrho_{\mathbf{r}} - k_B T\, \log \mathrm{Tr}_b e^{-\beta_T \left(H_{\mathrm{loc},\mathbf{r}} - Jz(\mathbf{b}^\dagger_{\mathbf{r}} \mathbf{\Psi}_{\mathbf{r}} + \text{h.c.}) \right)}, \tag{5.8b}$$

taken at a field configuration locally minimizing the free energy, $F\left(\{\mathbf{\Psi}_{\mathbf{r}}\}\right)$. The kinetic term describes the energy cost of spatial modulation of the condensate, leading

to the superfluid stiffness, whereas the local part of the free energy incorporates the effects of interaction as well as trapping. As a consequence of the $SO(3)$ rotational and the $U(1)$ gauge symmetry of the Hamiltonian, Eq. (5.3), $F_{\rm loc}$ depends only on two rotation invariant quantities, the superfluid density and the square of the magnetization, $\varrho_{\mathbf{r}}$ and $\vec{f}_{\mathbf{r}}^{\,2}$. Furthermore, $F_{\rm loc}$ can be easily determined numerically by truncating the local Hilbert space at a particle number $n_{\rm max} \sim 5$, since the filling of the states $n > n_{\rm max}$ is negligible due to the strong repulsion between atoms. We indeed find that nematic interactions $U_2 < 0$ force the superfluid to occupy the $\vec{f}_{\mathbf{r}}^{\,2} \equiv 0$ configurations, whereas ferromagnetic interactions favor $\vec{f}_{\mathbf{r}}^{\,2} \equiv 1$ states, as shown in Fig. 5.2.

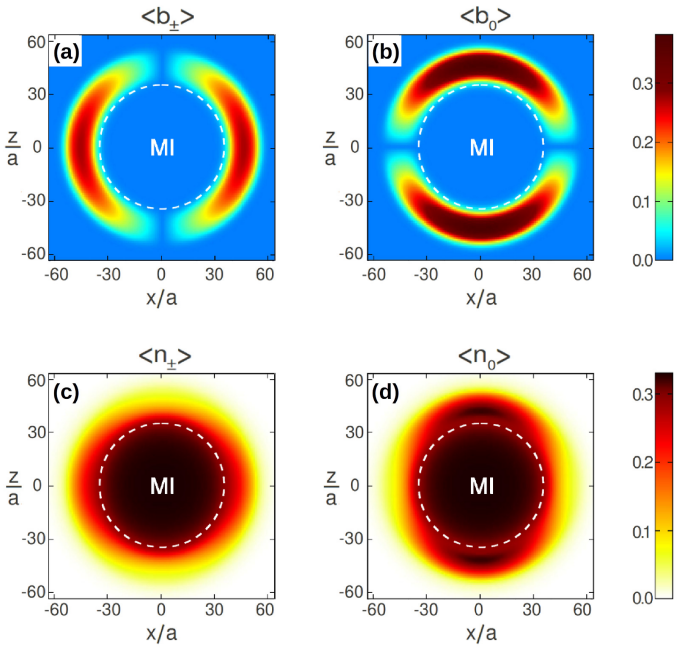

Figure 5.3: In-trap superfluid and particle densities of the skyrmion in the $(\mathbf{x}, \mathbf{z})$ plane. (**a**) The superfluid in the $|+1\rangle$ ($|-1\rangle$) bosons form a vortex (antivortex) around the equator, whereas the $|0\rangle$ condensate in (**b**) creates a dipole-like dark soliton structure at the poles. The surface of the Mott core is indicated by the dashed line. (**c**,**d**) show in-trap particle densities. Local increase in the superfluid order of one component leads to an increase of that component's particle density, whereas it repels the other two components, leading to a specific density structure characterizing the skyrmion. This structure gets significantly more pronounced at lower temperatures. [Physical parameters of the plot: $zJ/U_0 = 0.18$, $U_2/U_0 = 0.025$, $T/U_0 = 0.05$, chemical potential in the center of the trap $\mu_{\rm mid}/U_0 = 0.36$, and at the edge $\mu_{\rm edge}/U_0 = -0.09$.]

The best mean-field estimate to the superfluid order in the trap is found by minimizing the free energy functional, Eq. (5.8). Instead of the global minimum,

corresponding to the not very interesting topologically trivial configuration, $\mathbf{\Psi}_\mathbf{r} \propto \hat{\mathbf{z}}$, we need to find the skyrmion ground state in the space of superfluid configurations with unit winding. Let us, therefore, introduce the (artificial) imaginary time dynamics for the fields,

$$-\partial_\tau \Psi_{\mathbf{r}\alpha} = \frac{\delta F}{\delta \overline{\Psi}_{\mathbf{r}\alpha}}, \qquad -\partial_\tau \overline{\Psi}_{\mathbf{r}\alpha} = \frac{\delta F}{\delta \Psi_{\mathbf{r}\alpha}}, \tag{5.9}$$

that smoothly drives the free energy to a local minimum, without changing the topological winding of the superfluid. Indeed, under this dynamics, the free energy is constantly decreasing,

$$\frac{\partial F}{\partial \tau} = \sum_\mathbf{r} \left(\frac{\delta F}{\delta \mathbf{\Psi}_\mathbf{r}} \frac{\partial \mathbf{\Psi}_\mathbf{r}}{\partial \tau} + \frac{\delta F}{\delta \overline{\mathbf{\Psi}}_\mathbf{r}} \frac{\partial \overline{\mathbf{\Psi}}_\mathbf{r}}{\partial \tau} \right) = -2 \sum_\mathbf{r} \left| \frac{\delta F}{\delta \mathbf{\Psi}_\mathbf{r}} \right|^2 < 0.$$

Starting from a configuration with unit winding, the superfluid relaxes to a skyrmion configuration

$$\mathbf{\Psi}_\mathbf{r} \approx e^{i\varphi} \sqrt{\varrho(r)}\, \hat{\mathbf{r}}, \tag{5.10}$$

even in the presence of additional random noise in the initial configuration.[7]

In order to speed up numerics, $F_{\rm kin}$ was calculated using fast Fourier transform, whereas we used numerical interpolation in parameter space to calculate the local part of the free energy at each site.[8] Numerical stability of the dynamics has been reached by using a fourth order Runge-Kutta method for the imaginary time-steps. We also relied on Ref. [185] to reduce numerical and memory overhead (see Appendix C.2).

The numerically computed superfluid density $\langle b_{\mathbf{r}\alpha} \rangle$ and total particle densities $n_{\mathbf{r}\alpha} \equiv \langle b^\dagger_{\mathbf{r}\alpha}\, b_{\mathbf{r}\alpha} \rangle$, are displayed in Fig. 5.3, where the expectation values of local operators, $O_\mathbf{r}$ are given in the saddle point approximation by

$$\langle\, O_\mathbf{r} \,\rangle = \frac{{\rm Tr}_{b_\mathbf{r}} \left(O_\mathbf{r}\; e^{-\beta_T \left(H_{{\rm loc},\mathbf{r}} + Jz\, (\mathbf{b}^\dagger_\mathbf{r} \mathbf{\Psi}_\mathbf{r} + {\rm h.c.}) \right)} \right)}{{\rm Tr}_{b_\mathbf{r}} e^{-\beta_T \left(H_{{\rm loc},\mathbf{r}} + Jz\, (\mathbf{b}^\dagger_\mathbf{r} \mathbf{\Psi}_\mathbf{r} + {\rm h.c.}) \right)}}. \tag{5.11}$$

The superfluid densities are shown in the experimentally relevant basis of hyperfine spin components $F_z = \pm 1$ and $F_z = 0$, where the amplitudes of the various superfluid components read

$$\mathbf{\Psi}(\mathbf{r}) \;=\; \begin{pmatrix} \Psi_+(\mathbf{r}) \\ \Psi_0(\mathbf{r}) \\ \Psi_-(\mathbf{r}) \end{pmatrix} \;\simeq\; e^{i\varphi} \sqrt{\varrho(r)} \begin{pmatrix} \frac{\hat{\mathbf{x}} + i\hat{\mathbf{y}}}{\sqrt{2}} \\ \hat{\mathbf{z}} \\ \frac{\hat{\mathbf{x}} - i\hat{\mathbf{y}}}{\sqrt{2}} \end{pmatrix}. \tag{5.12}$$

[7] We note that in order for the skyrmion to be stable, its radius R needs to be sufficiently large so that the interaction energy gain ($\sim U_2$) exceeds the kinetic energy loss ($\sim 1/mR^2$) of skyrmion formation. In the parameter range considered in this chapter, this has always been the case.

[8] At this point, the $SO(3)$ symmetry of the interactions proved to be very helpful, since the interpolation needed to be carried out only in the two-dimensional space of $\varrho_\mathbf{r}$ and $f^2_\mathbf{r}$, instead of that of the Ψ fields, leading to a significant decrease in memory requirements.

The components $\Psi_\pm$ create a vortex and an antivortex around the equator, while the Ψ_0 component forms a 'dark soliton', a dipolar structure with opposite signs of the order parameter at the north and south poles, respectively.

The Mott core clearly suppresses the superfluid density in the central region of the trap, which forms a non-trivial structure in the superfluid shell that is also reflected in the particle densities of the components. In regions where a superfluid density of one component is stronger, its particle density also increases, on the expense of the other components. Accordingly, the density of $F_z = 0$ component is elongated along the z-axis, while those of the other two spin components are increased around the equator.

5.3.1 Skyrmion creation

The structure of the superfluid in Eq. (5.12) suggests a natural way to create a skyrmion in an experiment. By inducing an external magnetic field during the creation process, the Zeeman energy splits the hyperfine components $F_z = (1, 0, -1)$, which can therefore be addressed independently by optical means [186].

Starting with all atoms in the optical lattice in the $|F_z = -1\rangle$ component, a fraction of the atoms can be transferred into a vortex state in $|+1\rangle$ by applying a pair of counterpropagating lasers with opposite circulations, one of them with a Gaussian and the other one with Laguerre-Gaussian profile[9]. If the laser frequencies are tuned close to a transition to the transitions to a higher lying state with $F_z = 0$ spin, the atoms are transferred to the vortex state through a two-photon Λ process[10], gaining angular momentum from the Laguerre–Gaussian beam, as was demonstrated in [171]. The atoms in the $|1\rangle$ state can then be transferred into the $|0\rangle$ state using a radio-frequency π-shift[11] [187]. As a next step, the circulation of the Laguerre Gaussian beam can be switched, and a fraction of the atoms can then be transferred from the $|-1\rangle$ component to an anti-vortex state in the $|1\rangle$ state. A dark soliton in the $|-1\rangle$ state can then be created simply by illuminating the south hemisphere of the condensate with a far-detuned laser, perpendicular to the quantization axis that imprints a π phase in this component. Finally by switching the populations of the $|0\rangle$ and $|-1\rangle$ states using a radio-frequency π shift, we arrive at the skyrmion configuration in Eq. (5.12).

Alternatively, the skyrmion can also be created in a maybe even simpler way, by producing equal populations in all three components and then imprinting three

[9] Laguerre–Gaussian laser beams carry non-zero quanta of orbital angular momentum per photon. This angular momentum is due to the spatial distribution of the laser intensity, in particular its helical wave fronts, and it is not determined by the laser polarization.

[10] This is a second order virtual process, in which an atom absorbs a photon from the Laguerre–Gaussian beam, and re-emits it into the Gaussian mode, thereby being transferred into the $|0\rangle$ state.

[11] Radio-frequency signals of appropriate duration and intensity can be used to flip the populations of the states $|1\rangle \leftrightarrow |0\rangle$. Such manipulations correspond to a π-rotation around the x axis in spin space spanned by the two states. To address the $|1\rangle \leftrightarrow |0\rangle$ and $|0\rangle \leftrightarrow |-1\rangle$ transitions independently, one needs to increase the magnetic field to the regime where the so-called quadratic Zeeman effect sets in, and the two transition energies become different [188].

dark solitons in the x, y and z directions separately to create a state

$$\begin{pmatrix} \Psi_+(\mathbf{r}) \\ \Psi_0(\mathbf{r}) \\ \Psi_-(\mathbf{r}) \end{pmatrix} = \sqrt{\varrho(r)} \begin{pmatrix} \hat{\mathbf{x}} \\ \hat{\mathbf{z}} \\ -i\hat{\mathbf{y}} \end{pmatrix}. \tag{5.13}$$

Then, the skyrmion in Eq. (5.12) can be produced simply by mixing the $|+1\rangle$ and $|-1\rangle$ states using a $\pi/2$ radio frequency shift.

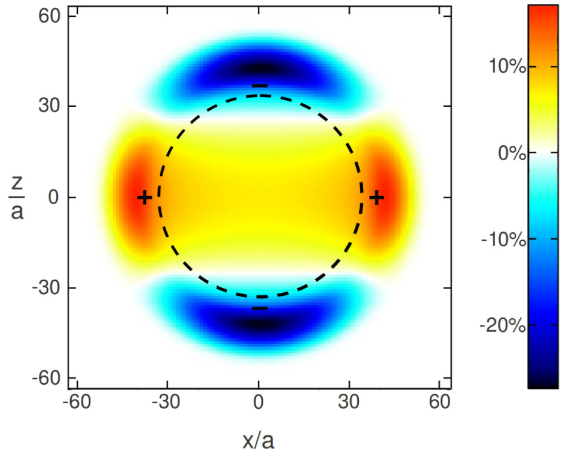

Figure 5.4: Difference of in-trap absorption images of the components $|\pm1\rangle$ and $|0\rangle$, taken along the y axis. Since the $|\pm1\rangle$ condensates form a vortex-like structure, they have a higher density around the equator, whereas $|0\rangle$ bosons, forming a dark soliton, are concentrated around the poles, see also Fig. 5.3. The surface of the Mott core is indicated by the dashed line. [Color code: integrated particle densities are shown as percentages of the largest value of component $|0\rangle$. Physical parameters: identical to the ones in Fig. 5.3.]

5.3.2 Detection through imaging

The characteristic density distribution and the superfluid correlations of the F_z spin components provides several ways to observe the skyrmion by optical imaging. The skyrmion's structure is perhaps most obviously reflected in in-trap absorption imaging, whereby a resonant, state selective[12] laser creates photographic a image of all spin components separately, showing their integrated densities along the laser axis (see Section 2.8). Although the images of different components may be similar, since most of the atoms is in the non-magnetic Mott core, the *difference* of the images clearly reveals the density structure of the shell, as shown in Fig. 5.4.

[12]By introducing a small external magnetic field, the Zeeman splitting can be increased above the laser linewidth, and the laser thus becomes resonant with only one of the components.

The skyrmion can also be detected through the commonly used time-of-flight imaging technique. After long enough free flight, the atoms' density at position $\tilde{\mathbf{r}}$ reflects the bosonic correlation function in momentum space [14],

$$C_\alpha\left(\mathbf{k}=\frac{m\tilde{\mathbf{r}}}{\hbar t}\right)=\sum_{\mathbf{r}\mathbf{r}'}e^{i\mathbf{k}(\mathbf{r}'-\mathbf{r})}\langle b^\dagger_{\mathbf{r}\alpha}b_{\mathbf{r}'\alpha}\rangle \tag{5.14}$$

at a time t (see Eq. (2.6)). In the mean-field approximation of Sec. 5.3, it is simply determined by the superfluid correlations, $C_\alpha(\mathbf{k})\approx\left|\sum_{\mathbf{r}}\langle b_{\mathbf{r}\alpha}\rangle e^{i\mathbf{k}\mathbf{r}}\right|^2$, up to an additional momentum-independent constant, and thus clearly reflects the spatial structure of the superfluid. Correspondingly, the time-of-flight image Fig. 5.5 displays sharp Bragg peaks at the centers of the Brillouin zone, originating from the lattice structure. The peaks, however, show an important fine structure, at the scale of $k\sim 1/R$, characteristic of the skyrmion superfluid structure. Indeed, the $|\pm1\rangle$ components form doughnut-shaped structures once released from the trap, reflecting their in-trap circulation, whereas the $|0\rangle$ atoms display a dark soliton-like structure along the z axis.

5.4 Excitation spectrum

We now investigate the effect of the skyrmion's non-trivial topology on the superfluid excitation spectrum, and study the Bogoliubov excitations in a two-dimensional effective field theory. We consider a thin superfluid shell of radius R, and we neglect the radial fluctuations of the superfluid, and construct an effective Lagrangian for the in-plane fluctuations of the nematic order parameter $\boldsymbol{\psi}(\mathbf{r})=(\psi_x(\mathbf{r}),\psi_y(\mathbf{r}),\psi_z(\mathbf{r}))$ on this shell. By doing so, we also neglect the effects of the Mott core on the superfluid due to the penetration of the nematic order to the insulating region, which is expected to decay abruptly, within a few atomic layers [189]. The effect of the Mott core presumably leads only to a negligible dissipation and a slight renormalization of the parameters of the two-dimensional model.

The real-time dynamics of in-plane fluctuations is determined by the two-dimensional effective Lagrangian[13] $\mathcal{L}=i\hbar\,\overline{\boldsymbol{\psi}}\,\partial_t\boldsymbol{\psi}-\mathcal{H}_{2\mathrm{D}}[\overline{\boldsymbol{\psi}},\boldsymbol{\psi}]$, with the Hamiltonian density

$$\mathcal{H}_{2\mathrm{D}}=\overline{\boldsymbol{\psi}}\left(-\frac{\hbar^2\,\Delta_2}{2m}-\tilde{\mu}\right)\boldsymbol{\psi}+\frac{u_0}{2}|\boldsymbol{\psi}|^4+\frac{u_2}{2}\left(\overline{\boldsymbol{\psi}}\vec{\mathbf{F}}\boldsymbol{\psi}\right)^2, \tag{5.15}$$

where Δ_2 denotes the Laplacian of the sphere of radius R, $\Delta_2=\vec{L}^2/R^2$, with the $\vec{L}=(L_x,L_y,L_z)$ angular momentum operator. The parameters of the Hamiltonian, the $\tilde{\mu}$ effective chemical potential of the superfluid, and the effective couplings u_0 and u_2, are determined by the parameters of the lattice model, as discussed in Appendix C.3.

[13] $\overline{\psi}_\alpha$ denotes the conjugate fields.

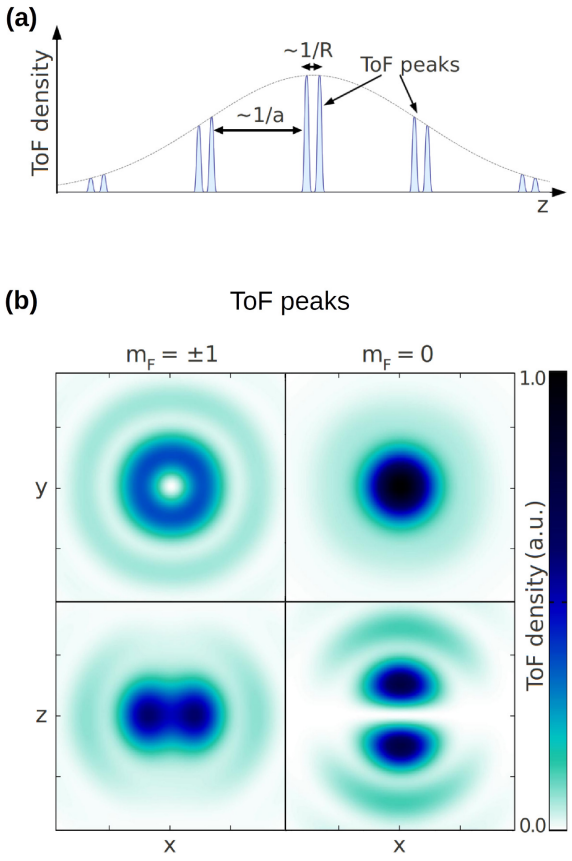

Figure 5.5: Time of flight (ToF) images of the skyrmion. (**a**) Schematic picture of the ToF peaks, concentrated around reciprocal lattice momenta ($\sim 2\pi/a$). The spatial structure of the skyrmion of spatial extent R is reflected in the fine structure ($1/R$) of the peaks. (**b**) Doughnut (dipole) shaped ToF peaks of bosons $|\pm 1\rangle$ ($|0\rangle$), on the left (right), taken along the z (y) axes, top (bottom). [Axes and color code: arbitrary but identical units. Physical parameters: identical to those in Fig. 5.3.]

The Euler–Lagrange equations generate the following equations of motion,

$$i\hbar\,\partial_t \boldsymbol{\psi} = \left(-\frac{\hbar^2\,\Delta_2}{2m} - \tilde{\mu} + u_0 |\boldsymbol{\psi}|^2 \right) \boldsymbol{\psi} + u_2 (\overline{\boldsymbol{\psi}} \vec{\mathbf{F}} \boldsymbol{\psi}) \cdot \vec{\mathbf{F}} \boldsymbol{\psi}. \tag{5.16}$$

The excitation spectrum of the condensate is obtained by linearizing Eq. (5.16) around the ground state field configuration. Notice that the linearized equations lead to the same excitation spectrum as the standard quantum mechanical treatment of Bogoliubov excitations of the superfluid, whereby one treats the fields $\psi(\mathbf{r})$ quantum mechanically, and keeps fluctuations only up to second order in the Hamiltonian. For simplicity, let us assume a spherically symmetric ground state in the trivial ('skyrmionless'), $\boldsymbol{\psi}_t = \sqrt{\rho_t}\,\hat{\mathbf{z}}$, as well as in the skyrmion configuration, $\boldsymbol{\psi}_s = \sqrt{\rho_s}\,\hat{\mathbf{r}}$.

The two-dimensional superfluid densities are determined from the stationary solutions of Eq. (5.16), as

$$\rho_t = \mu/u_0, \tag{5.17}$$

$$\rho_s = \left(\mu - \frac{\hbar^2}{mR^2}\right)/u_0. \tag{5.18}$$

Here, the curvature term $\hbar^2/(mR^2)$ is due to the topological winding of the skyrmion ground state, leading to the depletion of the superfluid density, and also modifies the excitation spectrum.

5.4.1 Trivial ground state

In the trivial ground state, $\boldsymbol{\psi}_t$, the fluctuations parallel ($\delta\boldsymbol{\psi}_{t\parallel}$) and perpendicular to the ground state ($\delta\boldsymbol{\psi}_{t\perp}$), decouple,

$$\begin{aligned} i\hbar\partial_t\delta\boldsymbol{\psi}_{t\parallel} &= -\frac{\hbar^2\,\Delta_2}{2m}\delta\boldsymbol{\psi}_{t\parallel} + u_0\rho_t\left(\delta\boldsymbol{\psi}_{t\parallel} + \delta\overline{\boldsymbol{\psi}}_{t\parallel}\right), \\ i\hbar\partial_t\delta\boldsymbol{\psi}_{t\perp} &= -\frac{\hbar^2\,\Delta_2}{2m}\delta\boldsymbol{\psi}_{t\perp} + u_2\rho_t\left(\delta\boldsymbol{\psi}_{t\perp} - \delta\overline{\boldsymbol{\psi}}_{t\perp}\right). \end{aligned}$$

and the spectrum can be obtained analytically by finding the eigenmodes of these linearized equations of motion, similarly to the case of a spatially homogeneous systems [190]. The interaction term u_0 sets the velocity of the phase and superfluid density fluctuations, $\delta\boldsymbol{\psi}_{t\parallel}$, whereas the spin interaction u_2 determines the velocity of the perpendicular spin fluctuations, $\delta\boldsymbol{\psi}_{t\perp}$. Due to the spatial rotation symmetry of the ground state, the eigenmodes are given in terms of spherical harmonic functions, and have energies

$$\begin{aligned} \epsilon_{\mathrm{ph},l} &= \sqrt{\left(\frac{\hbar^2}{2mR^2}\,l(l+1) + u_0\rho_t\right)^2 - (u_0\rho_t)^2}, \\ \epsilon_{\mathrm{sp},l} &= \sqrt{\left(\frac{\hbar^2}{2mR^2}\,l(l+1) + u_2\rho_t\right)^2 - (u_2\rho_t)^2}, \end{aligned}$$

with $l = 0, 1, \ldots$, the angular momentum quantum numbers. If, as in our case, the radius of the superfluid shell is large, as compared to the superfluid and magnetic healing lengths, $\xi_0 = \hbar/\sqrt{m\rho u_0}$ and $\xi_2 = \hbar/\sqrt{m\rho u_2}$, the excitation energies become

$$\begin{aligned} \epsilon_{\mathrm{ph},l} &\approx \frac{\hbar^2}{mR\xi_0}\sqrt{l(l+1)}, \\ \epsilon_{\mathrm{sp},l} &\approx \frac{\hbar^2}{mR\xi_2}\sqrt{l(l+1)}. \end{aligned}$$

Since the spin coupling is much smaller than the density coupling, $u_2 \ll u_0$, and thus $\xi_2 \gg \xi_0$, the spin excitations lie at a much lower energy than the density excitations and the low energy spectrum is dominated by spin excitations (see Fig. 5.6).

In a spherical trap, the rotational symmetry of the ground state implies that all excitations in the phase sector have a $(2l+1)$-fold orbital degeneracy, whereas spin excitations are $(2l+1)\times 2$-fold degenerate. The latter two-fold spin degeneracy originates from the residual $O(2)$ symmetry of the ground state in order parameter space. Although in a distorted trap the orbital degeneracy may be lifted, this two-fold degeneracy of spin modes is preserved by spin symmetry. In the $l=0$ sector, we find three zero-energy excitations (Goldstone modes), corresponding to global phase and spin rotations of the ground state around the x and y axes.[14] While the zero-mode corresponding to the phase is the artefact of the Bogoliubov treatment of superfluid excitations, the spin Goldstone modes have real physical origin, and are often referred to as Anderson tower excitations [191]. Although in our mean-field treatment, the ground state is defined by a single point in order parameter space, the real quantum mechanical ground state is actually an $SO(3)$ singlet. The associated uncertainty of the spontaneous symmetry broken phase is reflected in the appearance of spin Goldstone modes in the Bogoliubov treatment.

5.4.2 Skyrmion state

Excitations in the presence of the skyrmion are more complicated. The curvature of the ground state shifts the kinetic energy of fluctuations $\Delta_2 \to \Delta_2 + 2/R^2$, and it also couples density and spin fluctuations, $\delta\boldsymbol{\psi}_{s\parallel}$ and $\delta\boldsymbol{\psi}_{s\perp}$, parallel and perpendicular to the order parameter at that point. Thus, the dynamics of these fluctuations can only be described by the combined equations

$$i\hbar\,\partial_t\delta\boldsymbol{\psi}_s = -\frac{\hbar^2}{2m}\left(\Delta_2+\frac{2}{R^2}\right)\delta\boldsymbol{\psi}_s + u_0\rho_s\,(\delta\boldsymbol{\psi}_{s\parallel}+\delta\overline{\boldsymbol{\psi}}_{s\parallel}) + u_2\rho_s\,(\delta\boldsymbol{\psi}_{s\perp}-\delta\overline{\boldsymbol{\psi}}_{s\perp}), \quad (5.19)$$

with the fields decomposed as $\delta\boldsymbol{\psi}_s = \delta\boldsymbol{\psi}_{s\parallel} + \delta\boldsymbol{\psi}_{s\perp}$. Since the local orientation of the ground state changes constantly, the Laplacian non-trivially mixes the parallel and perpendicular fluctuations. This effect could be described by introducing non-Abelian gauge fields that account for the spatial change of the $(\delta\boldsymbol{\psi}_{s\parallel}, \delta\boldsymbol{\psi}_{s\perp})$ basis, however, the excitation modes can be more easily found by expanding the fields in Eq. (5.19) in a suitable basis. Since the spherically symmetric skyrmion is symmetric with respect to simultaneous $SO(3)$ rotations in real and in order parameter space, it is convenient to use the basis of vector spherical harmonic functions [192],

$$\mathbf{Y}_j^{m_j}(\mathbf{r}) = \hat{\mathbf{r}}\,Y_j^{m_j}(\mathbf{r}), \quad (5.20a)$$

$$\boldsymbol{\Upsilon}_j^{m_j}(\mathbf{r}) = r\,\nabla Y_j^{m_j}(\mathbf{r})/\sqrt{j(j+1)}, \quad (5.20b)$$

$$\boldsymbol{\Phi}_j^{m_j}(\mathbf{r}) = \hat{\mathbf{r}}\times\boldsymbol{\Upsilon}_j^{m_j}(\mathbf{r}), \quad (5.20c)$$

[14] Rotations around the z axis leave the ground state invariant, therefore, they do not give additional zero modes.

defined[15] using the spherical harmonic functions, Y_l^m, of angular momentum quantum numbers l and m. As shown in Appendix C.4, the vector spherical harmonics form a representation of the total angular momentum operators $\vec{J} = \vec{L} + \vec{\mathbf{F}}$, of simultaneous spatial ($\vec{L}$) and spin ($\vec{\mathbf{F}}$) rotations. Besides being orthogonal at all points in space, they form an orthonormal basis of vector fields on the sphere,

$$\int d^2\hat{r}\ \mathbf{Y}_j^{m_j\,*}(\hat{\mathbf{r}}) \cdot \mathbf{Y}_{j'}^{m'_j}(\hat{\mathbf{r}}) = \delta_{jj'}\,\delta_{m_j m'_j}, \tag{5.21a}$$

$$\int d^2\hat{r}\ \boldsymbol{\Upsilon}_j^{m_j\,*}(\hat{\mathbf{r}}) \cdot \boldsymbol{\Upsilon}_{j'}^{m'_j}(\hat{\mathbf{r}}) = \delta_{jj'}\,\delta_{m_j m'_j}, \tag{5.21b}$$

$$\int d^2\hat{r}\ \boldsymbol{\Phi}_j^{m_j\,*}(\hat{\mathbf{r}}) \cdot \boldsymbol{\Phi}_{j'}^{m'_j}(\hat{\mathbf{r}}) = \delta_{jj'}\,\delta_{m_j m'_j}, \tag{5.21c}$$

and

$$\sum_{j,m_j} \left[\mathbf{Y}_j^{m_j}(\hat{\mathbf{r}})\ \mathbf{Y}_j^{m_j\,*}(\hat{\mathbf{r}}') + \boldsymbol{\Upsilon}_j^{m_j}(\hat{\mathbf{r}})\ \boldsymbol{\Upsilon}_j^{m_j\,*}(\hat{\mathbf{r}}') + \boldsymbol{\Phi}_j^{m_j}(\hat{\mathbf{r}})\ \boldsymbol{\Phi}_j^{m_j\,*}(\hat{\mathbf{r}}') \right] = \delta^{(2)}(\hat{\mathbf{r}} - \hat{\mathbf{r}}'). \tag{5.22}$$

Vector spherical harmonics are especially well suited for the description of superfluid excitations in the skyrmion sector, since they naturally represent phase and spin fluctuations separately. The functions $\mathbf{Y}_j^{m_j}$ always point in the radial direction, and therefore, they span the space of phase (and density) fluctuations. In particular, the skyrmion itself corresponds to the function $\mathbf{Y}_0^0 \propto \psi_s$, which thus describes the variations of the global phase. Spin fluctuations, on the other hand, are spanned by the fields $\boldsymbol{\Upsilon}_j^{m_j}$ and $\boldsymbol{\Phi}_j^{m_j}$.

In the $\boldsymbol{\Phi}$-sector, the kinetic term has a particularly simple effect

$$-\left(\Delta_2 + \frac{2}{R^2}\right) \boldsymbol{\Phi}_j^{m_j} = \frac{j(j+1) - 2}{R^2}\ \boldsymbol{\Phi}_j^{m_j}, \tag{5.23}$$

whereas it mixes the $\mathbf{Y}$ and $\boldsymbol{\Upsilon}$ fields,

$$-\left(\Delta_2 + \frac{2}{R^2}\right) \begin{pmatrix} \mathbf{Y}_j^{m_j} \\ \\ \boldsymbol{\Upsilon}_j^{m_j} \end{pmatrix} = \frac{1}{R^2} \begin{pmatrix} j(j+1) & -2\sqrt{j(j+1)} \\ \\ -2\sqrt{j(j+1)} & j(j+1) - 2 \end{pmatrix} \begin{pmatrix} \mathbf{Y}_j^{m_j} \\ \\ \boldsymbol{\Upsilon}_j^{m_j} \end{pmatrix}. \tag{5.24}$$

Therefore, fluctuations in the $\boldsymbol{\Phi}$ sector decouple from the $(\mathbf{Y}, \boldsymbol{\Upsilon})$-fluctuations completely, and the corresponding $(2j+1)$-fold degenerate excitation energies can be derived analytically,

$$\epsilon_{\boldsymbol{\Phi},j} = \sqrt{\left(\frac{\hbar^2}{2mR^2}\ (j(j+1) - 2) + u_2\rho_s\right)^2 - (u_2\rho_s)^2}. \tag{5.25}$$

[15] The functions $\mathbf{Y}_j^{m_j}$ are defined for all $j = 0, 1, 2, \ldots$ angular momenta, with $m_j = -j, \ldots, j$, whereas $\boldsymbol{\Upsilon}_j^{m_j}$ and $\boldsymbol{\Upsilon}_j^{m_j}$ are only defined for $j \geq 1$, as can be clearly seen from their definitions in Eq. (5.20).

In the limit of large trap radii as compared to the superfluid and magnetic healing lengths, $R \gg \xi_0, \xi_2$, the excitation energies become

$$\epsilon_{\mathbf{\Phi},j} \approx \frac{\hbar^2}{mR\xi_2}\sqrt{j(j+1)-2}. \tag{5.26}$$

Specifically, the excitation energies are zero in the $j = 1$ angular momentum sector. The associated Goldstone modes correspond to small rotations of the skyrmion around the x, y and z axes in parameter space.[16] Together with the global phase fluctuations in the $\mathbf{Y}_{00}$ subspace, we thus find *four* zero modes in the skyrmion sector. The increased number of Goldstone modes, as compared to the trivial sector, is due to the different order parameter symmetry of the ground state. While rotation around the z axis leaves the trivial ground state $\psi_t \propto \hat{\mathbf{z}}$ invariant, they correspond to non-trivial rotations of the skyrmion, and correspondingly, find an additional zero energy mode associated with this rotation.

The eigenmodes of the $(\mathbf{Y}, \mathbf{\Upsilon})$-sector are more complicated, since the Laplacian mixes parallel and perpendicular fluctuations, see Eq. (5.24). The different total angular momentum sectors (j, m_j) are nevertheless separated due to the $SO(3)$ symmetry of the ground state, and their modes are $(2j+1)$-fold degenerate. The excitation energies can be easily determined from the equations of motion Eq. (5.19), and are given by the eigenvalues of the Bogoliubov-Hamiltonian

$$H_j^{\mathbf{Y}\mathbf{\Upsilon}} = \frac{\hbar^2}{2mR^2}\begin{pmatrix} \mathbf{h}_{0,j} & \mathbf{h}_1 \\ -\mathbf{h}_1 & -\mathbf{h}_{0,j} \end{pmatrix}, \tag{5.27}$$

with the real, dimensionless matrices

$$\mathbf{h}_{0,j} = \begin{pmatrix} j(j+1) & -2\sqrt{j(j+1)} \\ -2\sqrt{j(j+1)} & j(j+1)-2 \end{pmatrix} + \sqrt{2}\begin{pmatrix} R/\xi_0 & \\ & R/\xi_2 \end{pmatrix},$$

and

$$\mathbf{h}_1 = \sqrt{2}\begin{pmatrix} R/\xi_0 & \\ & -R/\xi_2 \end{pmatrix}.$$

We find that in the $u_2 \ll u_0$ limit, the two eigenmodes are very well separated in energy. The branch describing mainly phase excitations stays at high energies $\sim \hbar^2/(mR\xi_0)$, whereas the lower energy branch of spin excitations approaches the energies $\epsilon_{\mathbf{\Phi},j} \sim \hbar^2/(mR\xi_2)$ of the spin excitations in the $\mathbf{\Phi}$ sector (see Fig. 5.6). The splitting of these low energy spin modes (absent in the trivial case) is the result of the weak coupling of spin and charge excitation in the $(\mathbf{Y}, \mathbf{\Upsilon})$ sector, due to the skyrmion's winding.

Investigating the $j = 1$ sector of $(\mathbf{Y}, \mathbf{\Upsilon})$ excitations reveals a weak instability of the spherically symmetric skyrmion state, $\boldsymbol{\psi}_s$, towards a slight uniaxial deformation.

[16] For instance, the $(j, m_j) = (1, 0)$ mode rotates the skyrmion configuration around the z axis. Indeed, this mode is given in spherical coordinates by $\mathbf{\Phi}_1^0 \propto \sin\vartheta\ \hat{\varphi}$, ϑ and $\hat{\varphi}$ denoting the polar angle and the azimuthal unit vector, respectively.

This is also reflected in the Bogoliubov excitations, since one of the branches in this sector is imaginary, indicating that the spherically symmetric skyrmion state is unstable. Indeed, the skyrmion's energy can be decreased by allowing for a slight uniaxial deformation that amounts to only a few percent change in its shape.[17] To identify the effects of this spontaneous distortion, we numerically minimized the Hamiltonian in Eq. (5.15), and expanded it around the real, distorted ground state. We found that at this point, all eigenmodes became real, and the instability vanishes.[18] This spontaneous symmetry breaking does not influence the number of Goldstone modes, protected by symmetry, however, as indicated in Fig. 5.6, it slightly splits finite energy excitations due the $SO(3) \to SO(2)$ rotational symmetry breaking of the ground state. In particular, the lower branch of the $j = 1$ excitations in the $(\mathbf{Y}, \mathbf{\Upsilon})$-sector splits in a $3 \to (2 + 1)$-manner and their energies become extremely close to zero. The $(2j + 1)$-fold degenerate higher energy modes also exhibit a negligible splitting into j states of degeneracy 2 and a non-degenerate state, as induced by the spontaneous cylindrical distortion of the superfluid. The skyrmion's low energy spin excitation spectrum is sketched in Fig. 5.6. Notice that the structure of the excitation spectrum and the number of Goldstone modes is completely different from that of the skyrmion-free sector, and the spin degeneracy of the spin excitations completely disappears.

5.4.3 Modulation experiment

Let us now discuss the characteristic response of the skyrmion in a lattice modulation experiment. Modulation of the atom tunneling, J, excites oscillations in the superfluid density and phase, which are coupled to the low energy *spin* excitations through the skyrmion's texture, leading in effect to 'spin-orbit coupling'. In contrast, spin and phase fluctuations are completely decoupled in the trivial configuration, and lattice modulations can only excite the higher energy phase modes. This leads to a clear fingerprint of the skyrmion in the low energy spectrum of modulation experiments.

In particular, let us consider the modulation of the tunneling along the z axis, induced by varying the laser intensity of the optical lattice in this direction. Such a modulation corresponds to a ∂_z^2 perturbation (see Appendix C.3). This term is a linear combination of the tensor operators

$$\begin{aligned} T_0^0 &= (\partial_x^2 + \partial_y^2 + \partial_z^2)/\sqrt{3}, \\ T_2^0 &= (\partial_x^2 + \partial_y^2 - 2\,\partial_z^2)/\sqrt{6}, \end{aligned}$$

[17] A simple physical explanation of the distortion can be given as follows. As we showed earlier, the spatial winding of the skyrmion results in the local depletion of the superfluid density that leads, however, to interaction energy costs. This cost can be reduced by increasing the superfluid density around the poles, and also decreasing the winding of the order parameter here. Then, the regions around the equator will have stronger winding, and thus higher kinetic energy, but the superfluid density will be also lower here, leading to a net decrease of the skyrmion's energy.

[18] No such distortion was observed in our three-dimensional lattice simulations, though their spatial resolution were most likely insufficient to detect this small instability.

with angular momentum quantum numbers $(l, m) = (0, 0)$ and $(2, 0)$, respectively. Since T_0^0 and T_0^2 have spin $F = 0$, their total angular momentum quantum numbers are also given by $(j, m_j) = (l, m)$. Since T_0^0 and T_2^0 commute with $L^2 = -R^2\,\Delta_2$ and L_z, they leave the angular momentum eigenspaces invariant. In particular, since the functions $(\mathbf{Y}, \boldsymbol{\Upsilon})$ and $\boldsymbol{\Phi}$ form separate eigenspaces of L^2 (see Eqs. (5.23,5.24)). Thus, in the spherically symmetric skyrmion configuration[19] $\boldsymbol{\psi}_s \propto \mathbf{Y}_0^0$, lattice modulations can only excite

$$\mathbf{Y}_0^0 \to (\mathbf{Y}_j^0, \boldsymbol{\Upsilon}_j^0) \tag{5.28}$$

transitions, but no excitations into the $\boldsymbol{\Phi}$ subspace is allowed, and the angular momentum $m_j = 0$ is also conserved.

Further selection rules follow from the rotational symmetries of the perturbation operators. Due to the Wigner-Eckart theorem [193], the modulation operators T_0^0 and T_2^0 can only create $j = 0 \to 0$ and $j = 0 \to 2$ transitions in the total angular momentum. Therefore, the only non-vanishing matrix elements describing excitations of the spherically symmetric skyrmion are

$$\begin{aligned}
\langle \mathbf{Y}_2^0 |\, T_2^0\, | \mathbf{Y}_0^0 \rangle &= -\sqrt{\frac{2}{15}}, \\
\langle \boldsymbol{\Upsilon}_2^0 |\, T_2^0\, | \mathbf{Y}_0^0 \rangle &= \frac{1}{\sqrt{5}}, \\
\langle \mathbf{Y}_0^0 |\, T_0^0\, | \mathbf{Y}_0^0 \rangle &= -\frac{2}{\sqrt{3}}.
\end{aligned}$$

We thus find that the lattice modulations along one axis can only excite $(j, m_j) = (0, 0) \to (2, 0)$ transitions, and only in the $(\mathbf{Y}, \boldsymbol{\Upsilon})$ sector. This subspace consists of a high energy phase mode and a low energy spin mode (see the discussion below Eq. (5.27)), the being shown in the lower branch of the $l = 2$ levels in Fig. 5.6. This corresponds to the single level that can be excited through lattice modulations in the skyrmion sector.

Finally, let us also note that beside the lattice modulation experiment discussed here, one could also detect the skyrmion by modulating the trapping potential along one direction, leading to modulations of the superfluid density. These modulations would couple to the low energy spin excitations in the skyrmion sector, but not in the trivial configuration.

For typical parameters of a ^{23}Na experiment, we find that the energies of the superfluid excitation are in the range of 10 Hz, that is in the range of the trapping frequency (see Appendix C.3). It is the extreme stability of the Mott skyrmion configuration that allows for the detection of such low energy excitations, which would be essentially impossible in previous unstable skyrmion configurations [166, 172].

[19] From the point of view of modulation experiments, the spontaneous distortion of the skyrmion, on the order of one percent for the parameters considered here, is negligible. We will thus assume a spherically symmetric skyrmion in the following discussion.

5.5 Summary

In this chapter we discussed, how a stable skyrmion topological excitation can be stabilized in the ultracold atomic setting by invoking strong interactions. In the proposed setting, by loading a spin-1 nematic superfluid on a deep optical lattice, a Mott insulator core forms in the middle of the trap, surrounded by a nematic superfluid shell, that is naturally suited to host a skyrmion configuration. The Mott core pins the skyrmion, and thereby prevents it from the *dynamical* instability problems of previous proposals. We indeed verified this stability through extensive numerical simulations, whereby we treated the skyrmion on a mean-field level, by introducing the superfluid order parameter through a Hubbard–Stratonovich transformation.

We found that the non-trivial geometrical structure of the skyrmion leads to a characteristic spatial profile of both the densities and the superfluid order parameters of its spin components, that make the skyrmion detectable through commonly used imaging techniques – both in in-trap and in time-of-flight imaging. In particular, in the basis of hyperfine components $F^z = 1$, 0 and -1, the corresponding superfluid components form a vortex, a dark soliton and an anti-vortex-like structure, respectively. Since all of these structures can be imprinted separately using state-of-the-art experimental methods, it is not hard to find an experimental scheme to imprint the Mott skyrmion structure, and we indeed proposed two such methods.

The extreme stability of the skyrmion, and its compact geometry allows one to investigate the effect of its non-trivial winding on the superfluid excitation spectrum. Indeed, the skyrmion's topology significantly modifies the dynamics of superfluid excitations through two topological terms: a curvature term, leading to the depletion of the superfluid and to a shift of excitation energies, as well as a non-Abelian gauge field, that mixes charge (parallel) and spin (perpendicular) excitations, resulting in a 'spin-orbit coupling'. The low-energy (spin) excitation spectrum of the skyrmion is indeed markedly different from the topologically trivial configuration: both the energies of the levels and their quantum numbers change dramatically, and even the number of its Goldstone modes increases by one. The coupling between spin and charge excitations also leads to an important experimental signature of the skyrmion in lattice modulation experiments. Although these modulations excite only charge (density or phase) fluctuations directly, the spin-orbit coupling mechanism introduces an *indirect* coupling to the low energy spin excitations, absent in the topologically trivial configuration. Thus, we found that a low energy spin excitation peak in the lattice modulation spectrum is a direct fingerprint of the presence of the skyrmion.

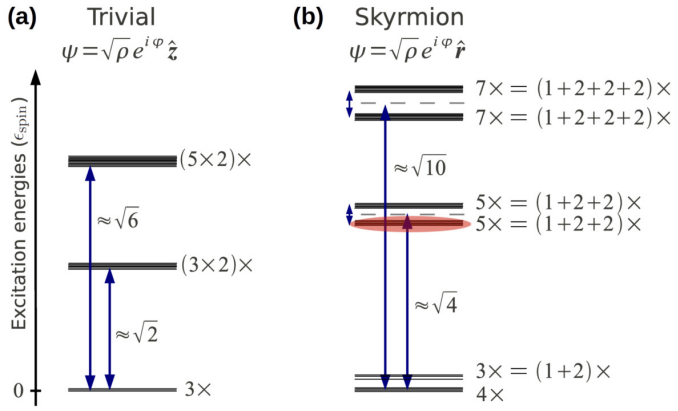

Figure 5.6: Low energy excitation spectrum of the skyrmion (right) versus that of the trivial configuration (left). The $SO(3)$ spatial rotation symmetry of the trivial configuration $\boldsymbol{\psi}_t \propto \hat{\mathbf{z}}$ leads to a $(2l+1)$ orbital degeneracy in the angular momentum sectors, l, whereas its rotation symmetry around the $\hat{\mathbf{z}}$ axis in spin space creates an extra two-fold degeneracy. In contrast, in the skyrmion sector (right), topological winding of the ground state splits the spin degeneracy, and only orbital (rotational) degeneracies survive. The topological terms also shift the energy levels of the skyrmion, leading to a markedly different excitation spectrum. The trivial and skyrmion states exhibit different number of zero modes (Goldstone modes) as well. Apart from the unphysical global phase degree of freedom, only two zero modes exist in the trivial case, corresponding to rotations around the $\hat{\mathbf{x}}$ and $\hat{\mathbf{y}}$ axes in parameter space. Rotations around $\hat{\mathbf{z}}$ leave $\boldsymbol{\psi}_t$ invariant, and we thus find no associated zero modes. However, we find an additional Goldstone mode in the skyrmion state, where all rotations provide a zero mode, in addition to the phase mode. The red ellipse denotes the single low energy spin-mode of the skyrmion that can be excited in the lattice modulation experiment discussed in Sec. 5.4.3. This mode is coupled by an effective 'spin-orbit' coupling to higher energy density/phase modes, directly excited by the modulation field. In contrast, lattice modulations do not couple (at first order) to low energy spin modes in the trivial configuration. [Excitation energies are shown in units of $\epsilon_{\rm spin} = \hbar^2/(mR\xi_2)$, with the magnetic healing length given by $\xi_2 = \hbar/\sqrt{mu_2\rho}$.]

6
Conclusions

The versatile experimental techniques of ultracold gases have led to the experimental realization of a large variety of correlated systems that had been hard to investigate in the traditional condensed matter setting. Due to their special detection and manipulation techniques, these gases provide a new viewpoint on known physical effects, but equally importantly, they have also led to the discovery of several novel phenomena, never observed before.

In this thesis, we investigated different aspects of correlated multicomponent cold atom systems, using a combination of field theoretical methods and numerical simulations. In the first part, we discussed the interactions of a two-component mixture confined into a quasi-two-dimensional bilayer structure. By solving the two-particle scattering problem exactly, we saw that the trapping potential significantly modifies interactions in these gases, and leads to the emergence of a number of novel bound and quasi-bound molecular states. Interestingly, the giant interlayer molecules persist even when the layer separation is significantly larger than the interspecies scattering length, and actually several hundred times larger than the size of the constituent atoms. Due to Feshbach-like resonances of the gas atoms with the quasi-bound molecular states, we found sharp resonances in the interspecies interactions, that are tunable by changing the separation of the layers. Thus, rather counter-intuitively, the gas can be made strongly interacting by actually separating its components. This effect provides another experimental tool, besides the commonly used magnetic Feshbach resonances, to control the interspecies and intraspecies interaction parameters of these gases independently. Furthermore, since the lifetime of the quasi-bound molecules increases significantly with increasing layer separation, they can be detected for the first time through commonly used shaking spectroscopy, as we demonstrated using detailed many-body calculations in the case of a dilute Bose gas [194].

In the second part, we discussed how weak attractive $SU(3)$ symmetric interactions lead to interesting color superconducting phases in a three-component fermion mixture. Using a combination of self-consistent equation of motion technique and a Gaussian variational approach, we were able to capture the interplay of superconductivity and magnetism in an unbiased way, and map out the system's rich global phase diagram, with a number of first and second order phase transitions and tricritical lines of special $O(2,2)$ symmetry. Furthermore, we were able to understand the basic physical mechanisms underlying this complex phase diagram based on simple energy arguments. We discussed how superconductivity is destroyed due to chemical potential differences through an unconventional (Zeeman) mechanism, and saw that the superconducting-normal boundaries become of first order at low temperatures, whereas they are of second order at higher temperatures. We also showed, through symmetry arguments, that the combination of the $SU(3)$ symmetry of the interactions and (approximate) particle-hole symmetry leads to the sixfold rotational symmetry of the phase diagram. When the particle-hole symmetry is broken, this is reduced to a threefold symmetry of the phase diagram in the region of small chemical potential differences. Finally, we performed a Ginzburg–Landau expansion of the free energy in this central region, and identified the terms that, through the coupling of superconducting and magnetic order, are responsible for the threefold symmetry of this region [133].

In the last part of this thesis, we discussed how interactions in a cold atomic system can lead to an unconventional, extremely long-lived topological excitation. In particular, we studied, how a skyrmion can be stabilized in a spin-1 nematic superfluid through exploiting strong interactions. By loading the superfluid into a deep optical lattice, a Mott insulator core forms in the central region of the trap, which is surrounded by a nematic superfluid shell, that is naturally suited to support a skyrmion due to the superfluid's non-trivial order parameter structure. We constructed the superfluid order parameter and the corresponding free energy of the shell through a Hubbard–Stratonovich transformation, and showed numerically that the 'Mott skyrmion' is indeed stable. This proposal thus opens up the way to create a stable single skyrmion excitation for the first time. We saw how the non-trivial spatial structure of the superfluid order parameter leads to characteristic fingerprints of the skyrmion using in-trap and in time-of-flight imaging techniques, and it allowed us to suggest two experimental methods to create the skyrmion. But perhaps most interestingly, the skyrmion can be detected through the effects of its topology on the superfluid excitation spectrum. Assuming a thin superfluid shell, we studied this effect in a two-dimensional effective model on the sphere, and found that the winding of the nematic order parameter introduces new topological terms for the superfluid fluctuations (a curvature term and a non-Abelian vector potential), that drastically modify the skrymion's excitation spectrum. We found significant changes in both the position and the degeneracy of the levels, and even a change in the number of Goldstone modes, as compared to the topologically trivial configuration. Using symmetry arguments, we were able to determine the skyrmion's response to lattice shaking, and found that these modulations couple to the low energy spin excitations

through an indirect 'spin-orbit coupling', induced by the skyrmion's topology. Since the characteristic energy scale of these excitations is as low as the frequency of the harmonic trap, it is the compact nature and extreme stability of the Mott skyrmion that allows for the investigation of the interplay between topology and the excitation spectrum [195].

7
Acknowledgement

I am using this opportunity to express my gratitude to the many people who supported me during my graduate studies. Foremost, I am grateful to my PhD advisor, Prof. Gergely Zaránd, who gave me great challenges during my work and from whom I learned a lot during the years. He opened up wonderful opportunities for me and his guidance was especially helpful to live with them.

I gratefully acknowledge the fruitful work with my collaborators, Prof. Eugene A. Demler and Prof. Balázs Dóra, and all the people who helped me with their ideas in my projects. My sincere thanks goes to the many members of the Exotic Quantum Phases Group and to my fellow students, especially Miklós Werner, Ákos Nagy, Péter Kómár, Ákos Rapp, György Vida and László Újfalusi, for our nice discussions and their help. I am thankful to Prof. Piet Brouwer and Prof. Felix von Oppen for the opportunity to spend a wonderful year at the Freie Universität Berlin and be part of their research group. I am also grateful to Prof. Attila Virosztek, who partly funded my research during the last year of my PhD, and to Prof. Csaba Tőke for reading and commenting on this thesis.

But most importantly, I would like to thank my wife Marie, and our sons, Zéno and Félix for their love and support, and my parents for their continuous help and motivation. This thesis is devoted to them.

A Appendix

A.1 Retarded Green's function of the confined system at short distances

The short distance behavior of the retarded Green's function $G_\epsilon^{(0)}$ in Eq. (3.5) plays a primary role in the characterization of the scattering properties of the confined quasi-two dimensional system. Whereas its $1/(4\pi\delta r)$ singularity in Eq. (3.6) simply comes from the locally three-dimensional nature of the scattering at short distances, its constant part $w_{\alpha\beta}(\epsilon/\hbar\omega_z)$ contains all information that determines the two-particle scattering states, and thus the scattering amplitudes in Eqs. (3.9, 3.10). To determine $w_{\alpha\beta}$, we compare Eqs. (3.5) and (3.6), and gain

$$w_{\alpha\beta}(\epsilon/\hbar\omega_z) = \lim_{\rho\to 0}\left(2\sum_{\nu=0}^{\infty}\sqrt{2\pi}l_z\,\phi_\nu^2(d_{\alpha\beta})K_0\left(-iq_\nu\rho\right) - \frac{\sqrt{2\pi}l_z}{\rho}\right), \tag{A1}$$

with $q_\nu = \sqrt{\frac{m}{\hbar^2}\left(\epsilon + i0^+ - \nu\hbar\omega_z\right)}$ introduced in the main text. Since the Bessel functions K_0 are logarithmic in their arguments, the sum in ν needs to be carried out to infinity, in order to gain the appropriate $1/\rho$ dependence of the second term. In order to simplify this expression, let us split the sum into two parts by choosing a large channel index, $\overline{\nu} \gg 1$, and treat the terms $\nu < 2\overline{\nu}$, and $\nu \geq 2\overline{\nu}$ separately. Since we eventually want to take the $\rho \to 0$ limit, we can assume that ρ is already small, and introduce the auxiliary constant, $\kappa \equiv \sqrt{2\overline{\nu}}\rho/l_z$, as a small parameter. In the first part of the sum, $\nu < 2\overline{\nu}$, the arguments of K_0 are small $q_\nu\rho \ll \kappa \ll 1$, we can thus use the asymptotic form of the modified Bessel functions

$$K_0(x \to 0) \sim -\log(x/2) - \gamma_E. \tag{A2}$$

in these terms.

In contrast, in the remaining part of the sum, $\nu \geq 2\overline{\nu} \gg 1$, we can make use of the fact that the energy of incoming particles are small compared to $\overline{\nu}\hbar\omega_z$, and the argument in K_0 is well approximated by $\sqrt{\nu}\rho/l_z$. Furthermore, we can use the asymptotic form of the Hermite functions in the $\nu \to \infty$ limit,

$$\sqrt{2\pi} l_z \, \phi_\nu^2(d_{\alpha\beta}) \sim \sqrt{\frac{2}{\pi}} \frac{\cos^2\left(\frac{d_{\alpha\beta}}{l_z}\sqrt{\nu+\frac{1}{2}} - \nu\frac{\pi}{2}\right)}{\sqrt{\nu}}.$$

As ν increases in this part of the sum, K_0's argument changes only slowly, whereas the $\cos^2$ term oscillates heavily, and averages to $1/2$,

$$\sum_{\nu=2\overline{\nu}}^{\infty} \sqrt{2\pi} l_z \, \phi_\nu^2(d_{\alpha\beta}) K_0\left(-iq_\nu\rho\right) \simeq \sum_{\nu=2\overline{\nu}}^{\infty} \frac{1}{\sqrt{2\pi\nu}} K_0(\sqrt{\nu}\rho/l_z).$$

Since ρ/l_z is a small parameter, this sum can be well approximated by an integral,

$$\sum_{\nu=2\overline{\nu}}^{\infty} \frac{1}{\sqrt{2\pi\nu}} K_0(\sqrt{\nu}\rho/l_z) \simeq \frac{l_z}{\rho}\sqrt{\frac{2}{\pi}} \int_\kappa^\infty dx \, K_0(x),$$

with $x = \sqrt{\nu}\,\rho/l_z$, which can be easily evaluated by making use of the identity $\int_0^\infty K_0(x)\,dx = \pi/2$, and the asymptotic form of K_0 in Eq. (A2). We thus find

$$\sum_{\nu=2\overline{\nu}}^{\infty} \sqrt{2\pi} l_z \, \phi_\nu^2(d_{\alpha\beta}) K_0\left(-iq_\nu\rho\right) \simeq \frac{l_z}{\rho}\sqrt{\frac{2}{\pi}} \left(\frac{\pi}{2} + \kappa\left(\log\frac{\kappa}{2} + \gamma_E - 1\right)\right),$$

As a final step, we put the two parts of the sum together in Eq. (A1), and by keeping $\kappa \to 0$, we take the limits $\rho \to 0$ and $\nu \to \infty$ to get

$$\begin{aligned} w_{\alpha\beta} = \lim_{\overline{\nu}\to\infty} \Bigg[& c_{\overline{\nu}} - \sum_{\nu=0}^{2\overline{\nu}-1} \sqrt{2\pi} l_z \, \phi_\nu^2(d_{\alpha\beta}) \log\left(\frac{\nu}{2} - \frac{\epsilon + i0^+}{\hbar\omega_z}\right) \\ & + \left(\gamma_E + \log\frac{\rho}{\sqrt{2}l_z}\right)\left(4\sqrt{\frac{\overline{\nu}}{\pi}} - 2\sum_{\nu=0}^{2\overline{\nu}-1} \sqrt{2\pi} l_z \, \phi_\nu^2(d_{\alpha\beta})\right)\Bigg], \end{aligned}$$

with $c_\nu = 2\sqrt{\frac{\nu}{\pi}}\log\frac{\nu}{e^2}$. In the $\overline{\nu} \to \infty$ limit, the term in the second row above vanishes, leading to the desired form of $w_{\alpha\beta}$, as given below Eq. (3.10).

Although the series form in Eq. (3.10) determines the function $w_{\alpha\beta}$ analytically, it is rather impractical for its numerical evaluation, since the series has a particularly poor $\sim \log\overline{\nu}/\sqrt{\overline{\nu}}$ convergence. Furthermore, in case of non-zero separation $d_{\uparrow\downarrow} \neq 0$, it exhibits heavily oscillating behavior. Let us derive, therefore, an integral representation of this expression as well that is much more suitable for numerical investigations. Following the initial steps of Ref. [76], we rewrite the terms in Eq. (A1) in an integral representation,

$$\frac{\sqrt{2\pi} l_z}{\rho} = \frac{1}{\sqrt{2}} \int_0^\infty \frac{d\tau}{\tau^{3/2}} e^{-\rho^2/(4l_z^2\,\tau)},$$

and

$$\frac{K_0\left(-iq_\nu\rho\right)}{2\pi} = -\frac{\hbar^2}{m}\int\frac{d^2k}{(2\pi)^2}\frac{e^{i\,\mathbf{k}\cdot\boldsymbol{\rho}}}{\epsilon+i0^+-\left(\frac{\hbar^2q^2}{m}+\hbar\nu\omega_z\right)}$$
$$= \int_0^\infty \frac{d\tau}{4\pi\tau}\, e^{\tau(\epsilon/\hbar\omega_z-\nu)}e^{-\rho^2/(4\,l_z^2\,\tau)}.$$

The latter equality holds only for the closed channels $\nu > \epsilon/\hbar\omega_z$, since otherwise the exponential integral explodes. As a second step, we choose an arbitrary closed channel $\hat{\nu} > \epsilon/\hbar\omega_z$, and rewrite the terms $\nu > \hat{\nu}$ in Eq. (A1) in the integral form,

$$w_{\alpha\beta} = \lim_{\rho\to 0}\left\{2\sum_{\nu=0}^{\hat{\nu}}\sqrt{2\pi}l_z\,\phi_\nu^2(d_{\alpha\beta})K_0\left(-iq_\nu\rho\right)\right.$$
$$\left.+\int_0^\infty\frac{d\tau}{\tau}e^{-\rho^2/(4l_z^2\,\tau)}\left[-\frac{1}{\sqrt{2\tau}}+\sum_{\nu=\hat{\nu}+1}^{\infty}\sqrt{2\pi}l_z\,\phi_\nu^2(d_{\alpha\beta})e^{\tau(\epsilon/\hbar\omega_z-\nu)}\right]\right\}. \tag{A3}$$

It is instructive to look at the exponential terms $e^{-\tau\nu}$ as thermal weights of the channel ν, multiplying the real space density ϕ_ν^2 of their wave functions. It is thus easy to see how the infinite sum above is related to the real space density matrix of a harmonic oscillator [124],

$$\sum_{\nu=0}^{\infty}\sqrt{2\pi}l_z\,\phi_\nu^2(\mathrm{z})\,e^{-\tau\nu} = \sqrt{\frac{e^\tau}{2\sinh\tau}}e^{-\tanh(\tau/2)\,\mathrm{z}^2/2l_z^2}.$$

Finally, let us rewrite the $\log(\rho/l_z)$ singularity of the modified Bessel functions K_0 in an integral representation, and take their $\rho\to 0$ asymptotic form up to linear order in ρ

$$K_0\left(-iq_\nu\rho\right) \sim \frac{1}{2}\left[i\pi-\gamma_E-\log\left(\frac{\nu\hbar\omega_z-\epsilon-i0^+}{4\hbar\omega_z}\right)\right.$$
$$\left.+\int_0^\infty\frac{d\tau}{\tau}\,\Theta\left(\frac{1}{4}-\tau\right)\,e^{-\rho^2/(4l_z^2\,\tau)}\right],$$

with the Heaviside function $\Theta(\tau)$. Substituting the above two expressions into Eq. (A3), the integral in τ becomes regular also in the $\rho\to 0$ limit, and we can thus write $w_{\alpha\beta}$ in the form

$$w_{\alpha\beta} = -\sum_{\nu=0}^{\hat{\nu}}\sqrt{2\pi}l_z\,\phi_\nu^2(d_{\alpha\beta})\left[\log\left(\frac{\nu\hbar\omega_z-\epsilon-i0^+}{4\hbar\omega_z}\right)+\gamma_E\right]$$
$$+\int_0^\infty\frac{d\tau}{\tau}\left[e^{-\tau\epsilon/(\hbar\omega_z)}\sqrt{\frac{e^\tau}{2\sinh\tau}}e^{-\tanh(\tau/2)\,d_{\alpha\beta}^2/(2l_z^2)}-\frac{1}{\sqrt{2\tau}}\right.$$
$$\left.+\sum_{\nu=0}^{\hat{\nu}}\sqrt{2\pi}l_z\,\phi_\nu^2(d_{\alpha\beta})\left(\Theta\left(\frac{1}{4}-\tau\right)-e^{\tau(\epsilon/\hbar\omega_z-\nu)}\right)\right].$$

The terms in the first row provide the logarithmically singular terms in energy up to the closed channel $\hat{\nu}$, whereas the integral contains the quantum contributions of

all other channels. Despite its complex nature at first sight, this formula is a rather handy representation of $w_{\alpha\beta}$ for numerical purposes, and we have used it extensively to evaluate the scattering amplitudes, $f_{\alpha\beta}^{\nu\nu'}$, to high numerical accuracy.

A.2 Renormalization of the T-matrix

The singular interaction term in the second-quantized Hamiltonian, Eq. (3.17), leads to divergences in the Bethe-Salpeter equations for the many-body T-matrix, and it thus needs appropriate regularization at large momenta. However, as we know from the theory of renormalization, the nature of the cut-off shall not matter from the point of view of low energy degrees of freedom of the system, as long as we express them using physically measurable quantities, such as the scattering lengths, instead of the bare interaction parameter $g_{\alpha\beta}^{\mathrm{3D}}$. We have thus introduced the regulator parameter $\boldsymbol{\rho}$ in the singular polarization operator, Eq. (3.19), that suppresses large-momentum contributions to the T-matrix.

The bare interaction parameter $g_{\alpha\beta}^{\mathrm{3D}}$ is related to the scattering lengths $a_{\alpha\beta}$ by the natural requirement that they reproduce the appropriate three-dimensional low-energy scattering properties in the vacuum. Eq. (2.2) shows that the three dimensional scattering amplitudes in this limit are given by $f_{\alpha\beta}^{\mathrm{3D}}(\epsilon \to 0) = -a$. Similar to the two-dimensional case, the three-dimensional vacuum T-matrix equals the scattering amplitudes up to a normalizing constant, and it is thus related to the three-dimensional scattering lengths as

$$\mathbf{T}_{\alpha\beta}^{\mathrm{3D}}(\Omega, \mathbf{Q}=0)\Big|_{\Omega\to 0-} = \frac{4\pi\hbar^2}{m}\, a_{\alpha\beta}, \tag{A4}$$

see Ref. [76]. It is given by the corresponding three-dimensional Bethe-Salpeter equation

$$\begin{aligned} T_{\alpha\beta}^{\mathrm{3D}}(\Omega, \mathbf{Q}) &= g_{\alpha\beta}^{\mathrm{3D}} \,+\, g_{\alpha\beta}^{\mathrm{3D}}\, \Pi^{\mathrm{3D}}(\Omega, \mathbf{Q})\, T_{\alpha\beta}^{\mathrm{3D}}(\Omega, \mathbf{Q}), \\ \Pi^{\mathrm{3D}}(\Omega, \mathbf{Q}) &= \int \frac{d^3q}{(2\pi)^3}\, \frac{e^{i\,\mathbf{q}\cdot\boldsymbol{\rho}}}{\hbar\Omega_+ - \frac{\hbar^2 Q^2}{4m} - \frac{\hbar^2 q^2}{m}} \quad \xrightarrow[\mathbf{Q}\to\mathbf{0}]{\Omega\to 0-} \quad -\frac{m}{4\pi\hbar^2}\,\frac{1}{\rho}. \end{aligned}$$

Comparing the above two equations, we can see that with the regulator $\boldsymbol{\rho}$, the bare coupling constants are related to the scattering amplitudes as

$$\frac{1}{g_{\alpha\beta}^{\mathrm{3D}}} = \frac{m}{4\pi\hbar^2}\left(\frac{1}{a_{\alpha\beta}} - \frac{1}{\rho}\right). \tag{A5}$$

Now, that we have the dependence of the bare coupling on the regulator, we can express the T-matrix in terms of the scattering lengths. Putting together Eq. (3.26) and (3.27), we find that

$$\mathbf{T}_{\alpha\beta}^{(0);NN',\nu\nu'}(\Omega, \mathbf{Q}) = \delta_{NN'}\, \frac{\phi_\nu^*(d_{\alpha\beta})\phi_{\nu'}(d_{\alpha\beta})}{\left(g_{\alpha\beta}^{\mathrm{3D}}\right)^{-1} - \sum_{\nu=0}^{\infty} \phi_\nu^2(d_{\alpha\beta})\, \Pi^{(0)}(\Omega - \nu\omega_z - E_{\mathrm{COM}}/\hbar)}, \tag{A6}$$

with the vacuum polarization operator

$$\Pi^{(0)}(\Omega) = \int \frac{d^2q}{(2\pi)^2} \frac{e^{i\mathbf{q}\cdot\boldsymbol{\rho}}}{\hbar\Omega_+ - \epsilon(q)} = -\frac{m}{2\pi\hbar^2} K_0\left(-i\,\rho\,\sqrt{m\Omega/\hbar}\right). \tag{A7}$$

Finally, expressing the T-matrix in terms of the scattering length through Eq. (A5), we find that it is indeed proportional to the scattering amplitudes, as given in Eqs. (3.10,3.28), with the function $w_{\alpha\beta}$, determining the energy dependence of the scattering amplitude, given by Eq. (A1).

Many-body corrections, in case of a strongly confined thermal gas, can be taken into account with a similar procedure. Keeping many-body corrections only in the lowest harmonic oscillator channel, we get a very similar equation for the T-matrix to Eq. (A6), with the only difference that the vacuum polarization in the $N = \nu = 0$ channel acquires a thermal correction, $\Pi^{(0)} \to \Pi^{(0)} + \delta\Pi^{\mathrm{th},00}_{\alpha\beta}$. With a similar renormalization process to the one in the vacuum case, we get back the many-body T-matrix, Eq. (3.29).

B
Appendix

B.1 Exact Ward identities

In this Appendix, by making use of the global $SU(3)$ invariance of the functional measure, we derive exact Ward identities that give constraints on the possible values of the order parameters and densities, Eqs. (4.8-4.11).

Consider the partition function $\mathcal{Z}$, defined in Eq. (4.15). For the current calculation we rewrite the action Eqs. (4.16,4.17) in the form

$$S_0(\hat{\mu}) = \sum_{\alpha\beta} \int \mathrm{d}x\, \overline{\psi}_\alpha \left((\partial_\tau + \mathcal{H}_0)\delta_{\alpha\beta} - \hat{\mu}_{\alpha\beta} \right) \psi_\beta, \tag{B1}$$

$$S_{\mathrm{int}}(\Gamma) = -\sum_{\alpha\beta\gamma\delta} \Gamma_{\alpha\beta\gamma\delta} \int \mathrm{d}x\, \overline{\psi}_\alpha \overline{\psi}_\beta \psi_\gamma \psi_\delta \; . \tag{B2}$$

by introducing $\hat{\mu}_{\alpha\beta} = \mu_\alpha\, \delta_{\alpha\beta}$ and $\Gamma_{\alpha\beta\gamma\delta} = \frac{1}{4} g_{\alpha\beta} \left(\delta_{\alpha\delta}\delta_{\beta\gamma} - \delta_{\alpha\gamma}\delta_{\beta\delta} \right)$. An $SU(3)$ transformation of the fields $\psi_\alpha(x) \to \sum_\beta U_{\alpha\beta}\psi_\beta(x)$ translates to the transformation of $\hat{\mu}$ and Γ in the functional integral. Expressing $\mathbf{U} = \exp(i \sum_{a=1}^{8} \zeta^a \mathbf{T}^a)$ with the Gell-Mann matrices $\mathbf{T}^a$, we find

$$\left. \frac{\partial}{\partial \zeta^a} \hat{\mu}_{\alpha\beta}(\zeta) \right|_{\zeta^a = 0} = i \sum_\gamma \left(\hat{\mu}_{\alpha\gamma} T^a_{\gamma\beta} - T^a_{\alpha\gamma} \hat{\mu}_{\gamma\beta} \right), \tag{B3}$$

$$\left. \frac{\partial}{\partial \zeta^a} \Gamma_{\alpha\beta\gamma\delta}(\zeta) \right|_{\zeta^a = 0} = i \left(g_{\alpha\beta} - g_{\gamma\delta} \right) \delta_{\alpha\delta}\, T^a_{\beta\gamma} \; . \tag{B4}$$

The invariance of the functional integral with respect to global $SU(3)$ transfor-

mations, $\frac{\partial \mathcal{Z}}{\partial \zeta^a}\Big|_{\zeta_a=0} = 0$, leads to the Ward identity

$$(\mu_\alpha - \mu_\beta)\,\frac{\partial \ln \mathcal{Z}}{\partial \hat{\mu}_{\alpha\beta}} = \sum_\gamma (g_{\beta\gamma} - g_{\alpha\gamma})\,\frac{\partial \ln \mathcal{Z}}{\partial \Gamma_{\gamma\alpha\beta\gamma}},$$

for any α and β, from which Eq. (4.35) follows.

B.2 Ward identities in the Gaussian approximation

Here, we derive approximate Ward identities, similar to those in Appendix B.1 that hold in the Gaussian approximation. As explained in Appendix B.3, we can assume that the inverse propagator in the definition of the partition function $\mathcal{Z}_\mathcal{G}$, Eq. (4.21), is local,

$$\mathcal{Z}_\mathcal{G} = \int \mathfrak{D}\overline{\psi}\,\mathfrak{D}\psi\, \exp\left(\frac{1}{2}\int \mathrm{d}1\, \overline{\phi}(1)\,\mathbf{G}^{-1}(1)\phi(1)\right),$$

where $\mathbf{G}^{-1}$ is defined in Eq. (4.26).

An $SU(3)$ transformation of the fields $\psi_\alpha(x) \to \sum_\beta U_{\alpha\beta}\psi_\beta(x)$ translates to the transformation of order parameters,

$$\mathbf{M} \mapsto \mathbf{U}\mathbf{M}\mathbf{U}^+, \tag{B5}$$

$$\mathbf{\Delta} \mapsto \mathbf{U}\mathbf{\Delta}\mathbf{U}^{\mathrm{T}}, \tag{B6}$$

see Eqs. (4.30,4.31). Using the invariance of the partition function with respect to these global $SU(3)$ transformations, we get the following constraints on the densities,

$$\mathrm{Tr}\left(\begin{pmatrix} \mathbf{\Gamma}^a_{\mathbf{M}} & \mathbf{\Gamma}^a_{\mathbf{\Delta}} \\ -\mathbf{\Gamma}^{a+}_{\mathbf{\Delta}} & \mathbf{\Gamma}^{a*}_{\mathbf{M}} \end{pmatrix}\begin{pmatrix} -\mathbf{n}^* & \mathbf{d} \\ \mathbf{d}^+ & \mathbf{n} \end{pmatrix}\right) = 0\,, \tag{B7}$$

with $\mathbf{\Gamma}^a_{\mathbf{M}} = [\mathbf{M}, \mathbf{T}^a]$ and $\mathbf{\Gamma}^a_{\mathbf{\Delta}} = (\mathbf{T}^a\mathbf{\Delta} + \mathbf{\Delta}\mathbf{T}^{a*})$.[1] Here the matrices $\mathbf{T}^a$, $a = 1, \ldots, 8$, are the Gell-Mann matrices.

In case of $SU(3)$ symmetric interactions, at the solutions of the EOM equations, Eqs. (4.8,4.9,4.13), this equation simplifies to the same form as the exact Ward identity, Eq. (4.35),

$$(\mu_\alpha - \mu_\beta)\, n_{\alpha\beta} = 0\,.$$

Therefore, when neither two of the chemical potentials are equal, the matrix of densities $\mathbf{n}$ and that of renormalized chemical potentials $\mathbf{M}$ are both diagonal (see Eq. (4.9)).

[1] We note that Eq. (B7) holds only at the solutions of the EOM self-consistency equations.

B.3 Saddle point equation in the Gaussian approximation

In this Appendix, starting from the saddle point equation, Eq. (4.24), we derive the saddle point form of the propagator $\mathcal{G}$ in the Gaussian approximation, Eqs. (4.25,4.26). We will use the notations of Section 4.3.2.

First, we fix the arbitrariness in the form of $\mathcal{G}^{-1}$ in the definition of $S_{\mathcal{G}}$, Eq. (4.20). We split $\mathcal{G}^{-1}$ into 3×3 matrices

$$\mathcal{G}^{-1}(1,2) = \begin{pmatrix} \mathbf{\Gamma}_A(x_1,x_2) & \mathbf{\Gamma}_B(x_1,x_2) \\ \mathbf{\Gamma}_C(x_1,x_2) & \mathbf{\Gamma}_D(x_1,x_2) \end{pmatrix}.$$

It is easy to see that, because of the anticommutation of the fields $\overline{\psi}_\alpha$ and ψ_α, modifications of $\mathcal{G}^{-1}$ that leave $\mathbf{\Gamma}_A(x_1,x_2) - \mathbf{\Gamma}_D^{\mathrm{T}}(x_2,x_1)$, $\mathbf{\Gamma}_B(x_1,x_2) - \mathbf{\Gamma}_B^{\mathrm{T}}(x_2,x_1)$ and $\mathbf{\Gamma}_C(x_1,x_2) - \mathbf{\Gamma}_C^{\mathrm{T}}(x_2,x_1)$ invariant, will not change $S_{\mathcal{G}}$. Therefore we may assume that $\mathcal{G}^{-1}$ has the symplectic symmetry

$$\begin{pmatrix} \mathbf{0} & \mathbf{1} \\ \mathbf{1} & \mathbf{0} \end{pmatrix} \mathcal{G}^{-1}(x_1,x_2) \begin{pmatrix} \mathbf{0} & \mathbf{1} \\ \mathbf{1} & \mathbf{0} \end{pmatrix} = -\left(\mathcal{G}^{-1}\right)^{\mathrm{T}}(x_2,x_1). \tag{B8}$$

The saddle point equation, Eq. (4.24), gives very strong constraints on the form of $\mathcal{G}$. In particular, it is equivalent to the EOM self-consistency equation of Section 4.3.1. To see this, we use the definition Eq. (4.19) to rewrite Eq. (4.24) in the form

$$\frac{1}{\mathcal{Z}_{\mathcal{G}}} \frac{\delta \mathcal{Z}_{\mathcal{G}}}{\delta \mathcal{G}(1,2)} = \frac{\delta \langle S - S_{\mathcal{G}} \rangle_{\mathcal{G}}}{\delta \mathcal{G}(1,2)}. \tag{B9}$$

The calculation of the left hand side of this equation is straightforward. Using only the definition of $\mathcal{Z}_{\mathcal{G}}$ (see Eq. (4.21)), and Eq. (4.23), we get

$$\frac{1}{\mathcal{Z}_{\mathcal{G}}} \frac{\delta \mathcal{Z}_{\mathcal{G}}}{\delta \mathcal{G}(1,2)} = -\frac{1}{2} \mathcal{G}^{-1}(2,1).$$

To evaluate the right hand side of Eq. (B9), omitting a constant term, we can write

$$\langle S - S_{\mathcal{G}} \rangle_{\mathcal{G}} = -\frac{1}{2} \int \mathrm{d}1 \, \mathrm{d}2 \, \mathcal{G}_0^{-1}(1,2) \mathcal{G}(2,1) + \langle S_{\mathrm{int}} \rangle_{\mathcal{G}}.$$

Then, it is easy to see that, the saddle point equation is equivalent to

$$\mathcal{G}^{-1}(1,2) = \mathcal{G}_0^{-1}(1,2) - 2 \frac{\delta \langle S_{\mathrm{int}} \rangle_{\mathcal{G}}}{\delta \mathcal{G}(2,1)}.$$

Expanding $\langle S_{\mathrm{int}} \rangle_{\mathcal{G}}$ using Wick's theorem gives a product of equal time propagators, whose variation according to the propagator matrix $\mathcal{G}$ can be straightforwardly calculated. We get the desired formulas, Eqs. (4.25,4.26), with the order parameters $\mathbf{M}$ and $\mathbf{\Delta}$ satisfying the EOM self-consistency equations, Eqs. (4.8,4.9), and (4.13). This means that the EOM method is *consistent* with the Gaussian variational approach.

B.4 Calculation of the Gaussian approximation to the free energy

In the following we calculate the Gaussian approximation of the free energy, Eq.(4.28). We first introduce the Fourier components $\psi_\alpha(\mathbf{r}) = \frac{1}{\sqrt{\Omega}} \sum_{\mathbf{k}} e^{i\mathbf{k}\mathbf{r}} a_{\alpha\mathbf{k}}$, obeying the anti-commutation relations $\{a^\dagger_{\mathbf{k}\alpha}, a_{\mathbf{k}'\beta}\} = \delta_{\alpha\beta}\,\delta_{\mathbf{k}\mathbf{k}'}$, where Ω denotes the volume. With these, the Hamiltonian, Eq. (4.27), takes on the form

$$H_{\mathcal{G}} = \frac{1}{2} \sum_{\mathbf{k}} \left\{ \left(\mathbf{a}^\dagger_{\mathbf{k}}, \mathbf{a}_{-\mathbf{k}} \right) \mathbf{\Xi}(\epsilon_{\mathbf{k}}) \begin{pmatrix} \mathbf{a}_{\mathbf{k}} \\ \mathbf{a}^\dagger_{-\mathbf{k}} \end{pmatrix} + \mathrm{Tr}\left(\epsilon_{\mathbf{k}} - \mathbf{M}\right) \right\},$$

with $\mathbf{\Xi}(\epsilon)$ defined in Eq. (4.7), and the last term originating from normal ordering.

From the above form, the calculation of $\mathcal{Z}_{\mathcal{G}} = \mathrm{Tr} e^{-\beta H_{\mathcal{G}}}$ is straightforward, though some care is needed to avoid double counting in momentum space. Note that, because of the symplectic symmetry, Eq. (4.14), and Hermiticity of the matrix $\mathbf{\Xi}(\epsilon)$, its eigenvalues are real and come in pairs. To each eigenvalue $\xi(\epsilon)$ there is another eigenvalue $-\xi(\epsilon)$. Using this property, $\log \mathcal{Z}_{\mathcal{G}}$ simplifies to

$$\begin{aligned} \log \mathcal{Z}_{\mathcal{G}} =& \frac{1}{2} \sum_{\mathbf{k}} \mathrm{Tr} \log \left(2 \cosh \left(\frac{\beta}{2} \mathbf{\Xi}\left(\epsilon_{\mathbf{k}}\right) \right) \right) \\ & - \frac{\beta}{2} \sum_{\mathbf{k}} \mathrm{Tr}\left(\epsilon_{\mathbf{k}} - \mathbf{M}\right). \end{aligned} \tag{B10}$$

It is also straightforward to determine $\langle H - H_{\mathcal{G}} \rangle_{\mathcal{G}}$ using Wick's theorem. One finds

$$\begin{aligned} \frac{1}{\Omega} \langle H - H_{\mathcal{G}} \rangle_{\mathcal{G}} =& \sum_{\alpha\beta} \frac{g_{\alpha\beta}}{2} (|n_{\alpha\beta}|^2 - n_{\alpha\alpha}\, n_{\beta\beta} - |d_{\alpha\beta}|^2) \\ & + \sum_{\alpha\beta} \left(M_{\alpha\beta} - \mu_\alpha\, \delta_{\alpha\beta} \right) n_{\alpha\beta} \\ & + \frac{1}{2} \sum_{\alpha\beta} \left(\Delta_{\alpha\beta}\, d^*_{\alpha\beta} + \Delta^*_{\alpha\beta}\, d_{\alpha\beta} \right). \end{aligned} \tag{B11}$$

Thus, using Eqs. (B10, B11), we get the result Eq. (4.29) for the Gaussian approximation of the free energy density .

In order to evaluate Eq. (B11), the densities and anomalous densities, $\mathbf{n}$ and $\mathbf{d}$, also have to be determined. These can be easily calculated from the variations of (B10) with respect to $\mathbf{M}$ and $\mathbf{\Delta}$, leading to the same equation, Eq. (4.13), as the EOM self-consistency equations.

B.5 Particle-hole transformation

Particle-hole symmetry introduces a $\mathbb{Z}_2$ symmetry of the mean-field phase diagram, when the band is half-filled, the DOS is particle-hole symmetric ($\rho(\epsilon) = \rho(-\epsilon)$), and

the interaction has $SU(3)$ symmetry ($g_{\alpha\beta} = g$ for $\alpha \neq \beta$). This symmetry together with the permutation symmetry of the fermion species makes the phase diagram six-fold symmetric, see Fig. 4.4.

In this Appendix we calculate the effect of the particle-hole transformation

$$\Psi_\alpha(x) \longleftrightarrow \Psi_\alpha^\dagger(x)$$

on the order parameters $\mathbf{M}$ and $\mathbf{\Delta}$. This transformation leaves the interaction invariant, whereas it modifies the bare chemical potentials and the single particle energies as

$$\begin{aligned} \mathcal{H}_0 &\rightarrow -\mathcal{H}_0, \\ \mu_\alpha &\rightarrow -\mu_\alpha - 2g\, n_{\max}, \end{aligned}$$

where $n_{\max} = \int_{-\hbar\omega_D}^{\hbar\omega_D} \mathrm{d}\epsilon\, \rho(\epsilon)$ is the density of the completely filled band. The bare chemical potentials remain unchanged on the mean-field level at

$$\mu_{\text{half}} = -g\, n_{\max},$$

which is precisely the condition for the band being half-filled (see Eq. (4.9)).

In order to investigate the inversion symmetry of the phase diagram, consider two Hamiltonians with opposite differences in bare chemical potentials from half-filling,

$$H^{(1)} \equiv H(\mathcal{H}_0, \mu_{\text{half}} + \delta\mu_\alpha, g, \Psi_\alpha^\dagger, \Psi_\alpha), \tag{B12}$$

$$H^{(2)} \equiv H(\mathcal{H}_0, \mu_{\text{half}} - \delta\mu_\alpha, g, \Psi_\alpha^\dagger, \Psi_\alpha), \tag{B13}$$

as defined in Eq. (4.3). A particle-hole transformation of $H^{(2)}$ leads to the equation

$$H^{(2)} = H(-\mathcal{H}_0, \mu_{\text{half}} + \delta\mu_\alpha, g, \tilde{\Psi}_\alpha^\dagger, \tilde{\Psi}_\alpha) \equiv H^{(3)}, \tag{B14}$$

where $\tilde{\Psi}_\alpha = \Psi_\alpha^\dagger$. Accordingly, the densities in the original and the particle-hole transformed system can be connected as

$$\begin{aligned} n_{\alpha\beta}^{(3)} &\equiv \langle \tilde{\Psi}_\alpha^\dagger(x)\tilde{\Psi}_\beta(x)\rangle_{(3)} = -n_{\alpha\beta}^{(2)*} + n_{\max}, \\ d_{\alpha\beta}^{(3)} &\equiv \langle \tilde{\Psi}_\alpha(x)\tilde{\Psi}_\beta(x)\rangle_{(3)} = -d_{\alpha\beta}^{(2)*}. \end{aligned}$$

Then, it is also straightforward to show from the definitions Eqs. (4.8,4.9) that the relation between the order parameters are

$$\mathbf{M}^{(2)} = -\mathbf{M}^{(3)*}, \quad \mathbf{\Delta}^{(2)} = -\mathbf{\Delta}^{(3)*}. \tag{B15}$$

Looking at their definitions, we see that the only difference between $H^{(2)}$ and $H^{(3)}$ is in the sign of $\mathcal{H}_0$. However, if the DOS is electron-hole symmetric,

$$\rho(\epsilon) = \rho(-\epsilon),$$

then all of the EOM self-consistency equations Eqs. (4.8,4.9,4.13), and the mean-field free energy Eqs. (4.13,4.29) are identical in the two systems. Therefore, the set of the

possible mean-field configurations have to be the same ($\mathbf{M}^{(1)} = \mathbf{M}^{(3)}$, $\mathbf{\Delta}^{(1)} = \mathbf{\Delta}^{(3)}$). Putting this, and Eq. (B15) together, we obtain the desired equations

$$\begin{aligned} \mathbf{M}(\mu_{\rm half} + \delta\mu_\alpha) &= -\mathbf{M}^*(\mu_{\rm half} - \delta\mu_\alpha), \\ \mathbf{\Delta}(\mu_{\rm half} + \delta\mu_\alpha) &= -\mathbf{\Delta}^*(\mu_{\rm half} - \delta\mu_\alpha), \end{aligned}$$

connecting order parameters at opposite $\delta\mu_\alpha$ values, with the other parameters of the system unchanged.

We remark that in the special case when $\delta\mu_1 + \delta\mu_2 + \delta\mu_3 = 0$, the particle-hole symmetry connects the points of the same (μ_x, μ_y) plane, and the mean-field phase diagram has an inversion symmetry. Away from this plane the inversion symmetry is only approximate, due to logarithmic corrections to the values of the order parameters, coming from the asymmetric cut-off.

C Appendix

C.1 Derrick's argument

The Derrick–Coleman theorem [141, 165] (or virial theorem) simply states that in a three-dimensional spatially homogeneous field theory, static localized excitations of finite energy cannot be stable in the absence of gauge fields, and they can always lower their energy by expanding or shrinking. Therefore, even though a topological excitation may be topologically protected, it can still be dynamically unstable. In more concrete terms, the argument refers to a scalar field theory in d dimensions, described by the classical (multicomponent) fields $\boldsymbol{\phi}(\mathbf{r})$. In the spatially homogeneous case, the kinetic and interaction energies of the model can be written as $E[\boldsymbol{\phi}] = E_{\rm kin}[\boldsymbol{\phi}] + E_{\rm int}[\boldsymbol{\phi}]$,

$$\begin{aligned} E_{\rm kin}[\boldsymbol{\phi}] &= \int d^d r \, \frac{\hbar^2}{2m} \left(\nabla \boldsymbol{\phi}(\mathbf{r})\right)^\dagger \left(\nabla \boldsymbol{\phi}(\mathbf{r})\right) \\ E_{\rm int}[\boldsymbol{\phi}] &= \int d^d r \, U_{\rm int}(\boldsymbol{\phi}(\mathbf{r})), \end{aligned}$$

with an unspecified interaction term $U_{\rm int}$. Let us take a localized, energetically stable, static field configuration, $\boldsymbol{\phi}_1$, which is thus a local minimum of the free energy functional $E[\boldsymbol{\phi}]$. Now consider the scaled fields $\boldsymbol{\phi}_\lambda(\mathbf{r}) \equiv \boldsymbol{\phi}_1(\lambda \mathbf{r})$, whose energy functional $E[\boldsymbol{\phi}_\lambda] = \lambda^{2-d} \, E_{\rm kin}[\boldsymbol{\phi}_1] + \lambda^{-d} \, E_{\rm int}[\boldsymbol{\phi}_1]$ can be easily determined by scaling out the factor λ. Since $\boldsymbol{\phi}_1$ is in a local minimum, the energy functional needs to be flat at $\lambda = 1$,

$$\partial_\lambda E[\boldsymbol{\phi}_\lambda]|_{\lambda=1} = (2-d) \, E_{\rm kin}[\boldsymbol{\phi}_1] - d \, E_{\rm int}[\boldsymbol{\phi}_1] = 0.$$

Substituting this equation to expression for the second derivative of the energy, we find that $\partial_\lambda^2 E|_{\lambda=1}$ is always negative in $d = 3$ dimensions,

$$\partial_\lambda^2 E[\boldsymbol{\phi}_\lambda]\Big|_{\lambda=1} = -2(d-2)\, E_{\text{kin}}[\boldsymbol{\phi}_1]$$

and the field configuration $\boldsymbol{\phi}_1$ cannot be stable. Therefore, it is always favorable for localized defects, to expand, or to shrink to a point, and thereby to vanish from the system.

C.2 Numerical methods

The imaginary time equations Eq. (5.9) for the minimization of the free energy lead to the following non-linear dynamics for the superfluid order parameters

$$\partial_\tau \Psi_{\mathbf{r}\alpha} = -Ja^2 \sum_{\mathbf{r}'} \Delta_{\mathbf{r}\mathbf{r}'} \Psi_{\mathbf{r}'\alpha} + \frac{\delta F_{\text{loc}}(\varrho_{\mathbf{r}}, \vec{f}_{\mathbf{r}}^{\,2})}{\delta\, \overline{\Psi}_{\mathbf{r}\alpha}}, \tag{C1}$$

where the variation of the local part of the free energy, $F_{\text{loc}}(\varrho,\ \vec{f}^{\,2})$, can be rewritten as

$$\frac{\delta F_{\text{loc}}}{\delta \overline{\Psi}_{\mathbf{r}\alpha}} = \frac{\delta F_{\text{loc}}}{\delta \varrho_{\mathbf{r}}} \frac{\delta \varrho_{\mathbf{r}}}{\delta \overline{\Psi}_{\mathbf{r}\alpha}} + \frac{\delta F_{\text{loc}}}{\delta \vec{f}_{\mathbf{r}}^{\,2}} \frac{\delta \vec{f}_{\mathbf{r}}^{\,2}}{\delta \overline{\Psi}_{\mathbf{r}\alpha}}.$$

While $\delta\varrho_{\mathbf{r}}/\delta\overline{\Psi}_{\mathbf{r}\alpha}$ and $\delta\vec{f}_{\mathbf{r}}^{\,2}/\delta\overline{\Psi}_{\mathbf{r}\alpha}$ depend only algebraically on Ψ_α, the variations of F_{loc} can only be evaluated from Eq. (5.8b) at high numerical cost. Therefore, in order to reduce the computational load of solving Eq. (C1), we precalculate $\delta F_{\text{loc}}/\delta\varrho$ and $\delta F_{\text{loc}}/\delta\vec{f}^{\,2}$ for a range of ϱ, $\vec{f}^{\,2}$ and μ values at the start of the simulation, and used numerical interpolation to evaluate their values at run time.[1]

In order to propagate the fields $\Psi_{\mathbf{r}\alpha}$ in imaginary time, we used a modified version of the Fourth-Order Runge–Kutta in Interaction Picture (RK4IP) method that is highly optimized for reducing memory and computational overhead. Since the algorithm is described in detail in Ref. [185], we just mention its basic idea here. As a first step, we separate the kinetic and local terms of Eq. (C1) as

$$-\partial_\tau \boldsymbol{\Psi} = \hat{D} \cdot \boldsymbol{\Psi} + \hat{U}\,[\boldsymbol{\Psi}] \cdot \boldsymbol{\Psi}, \tag{C2}$$

where we have dropped here the indices of the fields for convenience. Here, $\hat{D} = -Ja^2\Delta$ is a simple diffusion operator, whereas $\hat{U}$ is related to the variation of F_{loc} in Eq. (C1), and depends non-linearly on Ψ_α. By transforming the fields into interaction picture,

$$\boldsymbol{\Psi}_I(\tau) = e^{-(\tau-\tau_0)\hat{D}} \boldsymbol{\Psi}, \tag{C3}$$

[1] We evaluate the (infinite dimensional) trace in Eq. (5.8b) by truncating the Hilbert space at five particles per site. Note that, due to the large on-site repulsion U_0 of particles, higher on-site occupations are highly unlikely at the temperatures considered here.

one can express their time evolution as

$$-\partial_\tau \mathbf{\Psi}_I = \hat{U}_I\,[\mathbf{\Psi}_I]\cdot\mathbf{\Psi}_I \tag{C4}$$

with $\hat{U}_I = e^{(\tau-\tau_0)\hat{D}}\,\hat{U}\,e^{-(\tau-\tau_0)\hat{D}}$. The advantage of this form over Eq. (C2) is that one can efficiently calculate the diffusion exponential using fast Fourier transform (FFT), and simultaneously make use of the fact that $\hat{U}$ is spatially local by calculating it in real space. This provides significant numerical advantage as compared to the naive solution, whereby one simply uses a real-space matrix form of $\hat{D}$ and $\hat{U}$. Eq. (C4) can then be solved using a variety of numerical methods. The fourth order Runge–Kutta method, in particular, offers a high numerical performance with a small overhead. Furthermore, at midpoints of the time-steps, the diffusion exponential transformations can be made to vanish by an appropriate choice of τ_0 for that step, leading to further simplifications in the numerics. For further details of the algorithm the reader is referred to Ref. [185].

The numerical simulation for the minimization of the free energy in Eq. (5.8), based on an optimized version of the RK4IP algorithm, has been written by the author using the combination of C++ and MATLAB. For a lattice size of $256\times 256\times 256$ sites, the run time of the algorithm was on the order of one day on a standard laptop.

C.3 Effective two-dimensional model

In this Appendix, we give a rough estimate of the parameters of the two-dimensional effective Hamiltonian density in Eq.(5.15), by relating them to those of the lattice Hamiltonian, Eq. (5.3) and construct the fields ψ_α. Notice that the structure of the Hamiltonian density is dictated by the $SO(3)$ symmetry of the underlying lattice model, and although its parameters here are useful to determine the energy scale of the low energy excitations of the superfluid, their precise values are not important, since they do not influence the ratio of the excitation energies in the skyrmion versus the trivial sector, shown in Fig. 5.6.

Let us approximate the superfluid shell of the Mott skyrmion locally by an infinite two-dimensional slab of thickness $\eta\sim 10$ lattice sites in the z direction, whose real-time dynamics is described by the many-body lattice action [85]

$$\mathcal{S}_{\rm latt} = \int dt \sum_{\mathbf{r}\alpha} i\hbar\bar{b}_{\mathbf{r}\alpha}\,\partial_t b_{\mathbf{r}\alpha} - \left(H_{\rm kin}[\bar{b},b] + \sum_{\mathbf{r}} H_{{\rm loc},\mathbf{r}}[\bar{b},b]\right),$$

with the lattice Hamiltonian, Eq. (5.3). Since the superfluid shell is thin, we assume that the low energy dynamics of the superfluid is dominated by excitations in which the fields $b_{\mathbf{r}\alpha}$ are constant in the z direction. To describe the in plane variations of the superfluid, let us introduce the continuum fields $b_{\mathbf{r}\alpha}/a\to\psi_\alpha(\mathbf{r})$, governed by the effectively two-dimensional action

$$\mathcal{S}_{\rm latt} \approx \eta\int dt\int d^2r\,\sum_\alpha i\hbar\,\overline{\psi}_\alpha\,\partial_t\psi_\alpha - \mathcal{H}_{\rm 2D}[\overline{\boldsymbol{\psi}},\boldsymbol{\psi}], \tag{C5}$$

where the effective Hamiltonian density $\mathcal{H}_{2D}$ is defined in Eq. (5.15), with the parameters defined as $m = 1/(2Ja^2)$, $\tilde{\mu} = \mu + 6Jz$, $u_0 = U_0\, a^2$ and $u_2 = U_2\, a^2$. In the weak coupling limit, $zJ \gg U_0, U_2$, the low energy dynamics of the system can be described by the bare action above, in the saddle point approximation. In the limit of strong interactions, the parameters of the Hamiltonian are renormalized by quantum corrections, however, we assume that these effects do not change the order of magnitude of superfluid excitation energies significantly.

In this approximation, we also neglected the effect of the penetration of the nematic order to the Mott core, which may lead only to a small renormalization of the Hamiltonian parameters, and possibly to a negligible dissipation. Indeed, since the temperature range of the Mott skyrmion used here is an order of magnitude above the spin ordering temperature of the Mott core, the nematic order can only appear here due to the penetration of the superfluid (proximity effect), which is expected to decay within a few atomic layers [189]. Thus, the magnetization of the Mott core is expected to lead to negligible effects.

As we have seen in Sec. 5.4, the low energy excitations of the superfluid shell are of the order $\epsilon_{\rm spin} = \hbar^2/(mR\xi_2) = \sqrt{u_2\rho\hbar^2/mR^2}$, which is of the order of

$$\epsilon_{\rm spin} \simeq \frac{\sqrt{U_2\, J}}{R/a} \approx 10\,{\rm Hz},$$

assuming a two-dimensional superfluid density $\rho = 0.5/a^2$, and using the lattice model parameters in Sec. 5.2.

C.4 Vector spherical harmonics

Whereas the trivial configuration $\boldsymbol{\psi}_t = \sqrt{\rho_t}\,\hat{\mathbf{z}}$ of the two-dimensional model is symmetric with respect to spatial $SO(3)$ rotations, the spherically symmetric skyrmion, $\boldsymbol{\psi}_s = \sqrt{\rho_s}\,\hat{\mathbf{r}}$, is left invariant by simultaneous $SO(3)$ rotations *both* in spin and in real space. Since the Hamiltonian density in Eq. (5.15) is also invariant with respect to these rotations, the superfluid excitations will be characterized their total angular momentum quantum numbers

$$\vec{\mathbf{J}} = \vec{L} + \vec{\mathbf{F}}.$$

Here the operators L_α are the angular momentum operators around axes $\alpha = x, y, z$, whereas the operators $\mathbf{F}_\alpha$ are the corresponding spin rotation operators. Using the spherical harmonic functions Y_l^m of angular momentum quantum numbers (l, m), it is rather easy to create a *reducible* representation of the total angular momentum operator

$$\mathrm{Y}_l^{m\nu}(\hat{\mathbf{r}}) = Y_l^m(\hat{\mathbf{r}})\ |\nu\rangle\,,$$

where $|\nu\rangle$ denotes the $F_z = \nu$ eigenstates in order parameter space. Indeed, the vector functions $\mathrm{Y}_l^{m,\nu}$, defined on the unit sphere, have the following quantum numbers

in real and spin space,

$$\begin{aligned} L^2\ \mathrm{Y}_l^{m\nu} &= l(l+1)\ \mathrm{Y}_l^{m\nu}, \\ L^z\ \mathrm{Y}_l^{m\nu} &= m\ \mathrm{Y}_l^{m\nu}, \\ F^2\ \mathrm{Y}_l^{m\nu} &= 2\ \mathrm{Y}_l^{m\nu}, \\ F^z\ \mathrm{Y}_l^{m\nu} &= \nu\ \mathrm{Y}_l^{m\nu}. \end{aligned}$$

By making use of the Clebsch–Gordan coefficients $\langle j, m_j | l, m; 1, \nu \rangle$, one can construct an irreducible representations for the total angular momentum operator $\vec{\mathbf{J}}$,

$$\begin{aligned} \mathrm{Y}_{j;l}^{m_j} &\equiv \sum_{m,\nu} \langle j, m_j \,|\, l, m;\, 1, \nu \rangle\ \mathrm{Y}_l^{m\nu} \\ &= \sum_{\nu} \langle j, m_j \,|\, l, m_j - \nu;\, 1, \nu \rangle\ \mathrm{Y}_l^{m_j - \nu, \nu} \end{aligned}$$

on the subspace of angular momentum l vector functions.[2] These irreducible functions have the following quantum numbers

$$\begin{aligned} J^2\ \mathrm{Y}_{j;l}^{m_j} &= j(j+1)\ \mathrm{Y}_{j;l}^{m_j}, \\ J^z\ \mathrm{Y}_{j;l}^{m_j} &= m_j\ \mathrm{Y}_{j;l}^{m_j}, \\ L^2\ \mathrm{Y}_{j;l}^{m_j} &= l(l+1)\ \mathrm{Y}_{j;l}^{m_j}, \\ F^2\ \mathrm{Y}_{j;l}^{m_j} &= 2\ \mathrm{Y}_{j;l}^{m_j}, \end{aligned}$$

and they form a complete orthonormal basis among vector functions on the unit sphere

$$\begin{aligned} \int d^2\hat{r}\ \mathrm{Y}_{j;l}^{m_j\,*}(\hat{\mathbf{r}}) \cdot \mathrm{Y}_{j';l'}^{m'_j}(\hat{\mathbf{r}}) &= \delta_{jj'}\, \delta_{m_j m'_j}\, \delta_{l\,l'} \\ \sum_{l,j,m_j} \mathrm{Y}_{j;l}^{m_j}(\hat{\mathbf{r}})\ \mathrm{Y}_{j;l}^{m_j\,*}(\hat{\mathbf{r}}') &= \delta^{(2)}(\hat{\mathbf{r}} - \hat{\mathbf{r}}') \end{aligned}$$

Despite the simple transformation properties of the vector functions $\mathrm{Y}_{j;l}^{m_j}$, it is worth to perform a unitary transformation into the geometrically more transparent basis of *vector spherical harmonics* [192],

$$\begin{pmatrix} \mathbf{Y}_j^{m_j} \\ \mathbf{\Phi}_j^{m_j} \\ \mathbf{\Upsilon}_j^{m_j} \end{pmatrix} = \begin{pmatrix} \sqrt{\frac{j+1}{2j+1}} & 0 & \sqrt{\frac{j}{2j+1}} \\ 0 & 1 & 0 \\ -\sqrt{\frac{j}{2j+1}} & 0 & \sqrt{\frac{j+1}{2j+1}} \end{pmatrix} \begin{pmatrix} \mathrm{Y}_{j;j+1}^{m_j} \\ \mathrm{Y}_{j;j}^{m_j} \\ \mathrm{Y}_{j;j-1}^{m_j} \end{pmatrix},$$

also given by Eq. (5.20). Since the transformation is unitary, the spherical vector harmonics also provide an orthonormal basis among the vector functions on the

[2] Since the spin quantum number is a triplet, the vector functions $\mathrm{Y}_{j;l}^{m_j}$ are non-zero only for $j = l-1$, l and $l+1$.

sphere, similar to the functions $\mathrm{Y}_{j;l}^{m_j}$ in Eq. (C6). Furthermore, by looking at their defining equations, Eq. (5.20), it is easy to see that they are orthogonal for given $(j,\, l,\, m_j)$ at all spatial points, and the fields $\mathbf{Y}$ span the space of radial vector fields, whereas the $\boldsymbol{\Upsilon}$ and $\boldsymbol{\Phi}$ fields span the space of tangential vector fields on the sphere. This property makes the spherical vector harmonics functions especially well-suited for the description of superfluid excitations in the skyrmion sector, since the phase and spin fluctuations can be treated separately in this basis.

Bibliography

[1] M. H. Anderson, J. R. Ensher, M. R. Matthews, C. E. Wieman, and E. A. Cornell, *Science* **269**, 198 (1995).

[2] C. C. Bradley, C. A. Sackett, J. J. Tollett, and R. G. Hulet, *Phys. Rev. Lett.* **75**, 1687 (1995).

[3] K. B. Davis *et al.*, *Phys. Rev. Lett.* **75**, 3969 (1995).

[4] B. DeMarco, and D. D. Jin, *Science* **285,** 1703 (1999).

[5] F. Schreck *et al.*, *Phys. Rev. Lett.* **87**, 080403 (2001).

[6] R. P. Feynman, *Int. J. Theor. Phys.* **21**, 467 (1982).

[7] I. Bloch, T. W. Hänsch, and T. Esslinger, *Phys. Rev. Lett.* **82**, 3008 (1999).

[8] T. Anker *et al.*, *Phys. Rev. Lett.* **94**, 020403 (2005).

[9] J. R. Abo-Shaeer, C. Raman, J. M. Vogels, and W. Ketterle, *Science* **292**, 476 (2001).

[10] M. W. Zwierlein, J. R. Abo-Shaeer, A. Schirotzek, C. H. Schunck and W. Ketterle, *Nature* **435**, 1047 (2005).

[11] K. E. Strecker, G. B. Partridge, A. G. Truscott and R. G. Hulet, *Nature* **417**, 150 (2002).

[12] L. Khaykovich *et al.*, *Science* **296**, 1290 (2002).

[13] J. Denschlag *et al.*, *Science* **287**, 97 (2000).

[14] M. Greiner, O. Mandel, T. Esslinger, T. W. Hänsch, and I. Bloch. *Nature* **415**, 39 (2002).

[15] J. M. Kosterlitz and D. J. Thouless, *J. Phys. C: Solid State Phys.* **6**, 1181 (1972).

[16] J. M. Kosterlitz, *J. Phys. C: Solid State Phys.* **7**, 1046 (1973).

[17] Z. Hadzibabic, P. Krüger, M. Cheneau, B. Battelier and J. Dalibard, *Nature* **441**, 1118 (2006).

[18] V. Schweikhard, S. Tung, and E. A. Cornell, *Phys. Rev. Lett.* **99**, 030401 (2007).

[19] B. Paredes *et al.*, *Nature* **429**, 277 (2004).

[20] T. Kinoshita, T. Wenger, D.S. Weiss, *Science* **305**, 1125 (2004).

[21] E. Haller *et al.*, *Science* **325**, 1224 (2009).

[22] E. Haller *et al.*, *Nature* **466**, 597 (2010).

[23] M. Gring *et al.*, *Science* **337**, 1318 (2012).

[24] Y. Castin, in *Les Houches - Ecole d'Ete de Physique Theorique, Vol. 72*, edited by R. Kaiser, C. Westbrook and F. David (Springer Berlin Heidelberg, 2001).

[25] T.-L. Ho, *Phys. Rev. Lett.* **81**, 742 (1998).

[26] F. Zhou, *Phys. Rev. Lett.* **87**, 080401 (2001).

[27] K. Xu *et al.*, *Phys. Rev. A* **72**, 043604 (2005).

[28] T. Hänsch and A. Schawlow, *Opt. Commun.* **13**, 68 (1975).

[29] D. Wineland, D. Hehmelt, *Bull. Am. Phys. Soc.* **20**, 637 (1975).

[30] C. N. Cohen-Tannoudji and W. D. Phillips, *Phys. Today* **43**, 33 (1990).

[31] S. Chu, L. W. Hollenberg, J. E. Bjorkholm, A. Cable, A. Ashkin, *Phys. Rev. Lett.* **55**, 48 (1985).

[32] W. H. Wing, *Prog. Quant. Elec.* **8**, 181 (1984).

[33] P. Meystre, *Atom Optics*, (Springer, New York, 2001).

[34] W. Ketterle and N. J. van Druten in *Advances in Atomic, Molecular, and Optical Physics, Vol. 37*, edited by B. Bederson and H. Walther (Academic Press, San Diego, 1996).

[35] M. D. Barrett, J. A. Sauer, and M. S. Chapman, *Phys. Rev. Lett.* **87**, 010404 (2001).

[36] J. Dalibard, C. Cohen-Tannoudji, *J. Opt. Soc. Am. B* **2**, 1707 (1985).

[37] R. Grimm and M. Weidemüller in *Advances in Atomic, Molecular, and Optical Physics, Vol. 42*, edited by B. Bederson and H. Walther (Academic Press, 2000).

[38] P. Meystre and M. Sargent, *"Elements of Quantum Optics"* (Springer, 1999).

[39] I. Bloch, J. Dalibard and W. Zwerger, *Rev. Mod. Phys.* **80**, 885 (2008).

[40] W. Krauth, *Phys. Rev. Lett.* **77**, 3695 (1996).

[41] L. D. Landau and E. M. Lifshitz, *Quantum Mechanics: Non-Relativistic Theory* (Pergamon Press, New York, 1987).

[42] H. Feshbach, *Ann. Phys. (N.Y.)* **5**, 337 (1958).

[43] E. Tiesinga, A. Moerdijk, B. J. Verhaar, and H. T. C. Stoof, *Phys. Rev. A* **46**, R1167 (1992).

[44] E. Tiesinga, B. J. Verhaar, and H. T. C. Stoof, *Phys. Rev. A* **47**, 4114 (1993).

[45] M. Theis *et al.*, *Phys. Rev. Lett.* **93**, 123001 (2004).

[46] C. Becker *et al.*, *New J. Phys.* **12**, 065025 (2010).

[47] M. Atala *et al.*, *Nat. Phys.* **9**, 795 (2013).

[48] G. Roati *et al.*, *Nature* **453**, 895 (2008).

[49] N. W. Ashcroft and N. D. Mermin, *"Solid State Physics"* (Holt, Rinehart and Winston, 1976).

[50] E. Demler and F. Zhou, *Phys. Rev. Lett.* **88**, 163001 (2002).

[51] M. P. A. Fisher, P. B. Weichman, G. Grinstein, and D. S. Fisher, *Phys. Rev. B* **40**, 546 (1989).

[52] Y. Kato, Q. Zhou, N. Kawashima and N. Trivedi, *Nat. Phys.* **4**, 617 (2008).

[53] A. Altland and B. Simons, *"Condensed matter field theory"* (Cambridge University Press, 2010).

[54] F. D. M. Haldane, *Phys. Rev. Lett.* **61**, 2015 (1988).

[55] B. A. Bernevig, T. L. Hughes, and S.-C. Zhang, *Science* **314**, 1757 (2006).

[56] C. Nayak, S. H. Simon, A. Stern, M. Freedman, and S. Das Sarma, *Rev. Mod. Phys.* **80**, 1083 (2008).

[57] P. Fazekas, *"Lecture Notes on Electron Correlation and Magnetism"* (World Scientific, 1999).

[58] P. A. Lee, N. Nagaosa, and X.-G. Wen, *Rev. Mod. Phys.* **78**, 17 (2006).

[59] M. W. Zwierlein, A. Schirotzek, C. H. Schunck, and W. Ketterle, *Science* **311**, 492 (2006).

[60] J. W. Park *et al.*, *Phys. Rev. A* **85**, 051602(R) (2012).

[61] M. W. Zwierlein, J. R. Abo-Shaeer, A. Schirotzek, C. H. Schunck, and W. Ketterle, *Nature* **435**, 1047 (2005).

[62] P. Makotyn, C. E. Klauss, D. L. Goldberger, E. A. Cornell, and D. S. Jin, *Nat. Phys.* **10**, 116 (2014).

[63] M. Olshanii, *Phys. Rev. Lett.* **81**, 938 (1998).

[64] D. S. Petrov, M. Holzmann, and G. V. Shlyapnikov, *Phys. Rev. Lett.* **84**, 2551 (2000).

[65] D. S. Petrov and G. V. Shlyapnikov, Phys. Rev. A **64**, 012706 (2001).

[66] W. Fu, Z. Yu and X. Cui, Phys. Rev. A **85**, 012703 (2012).

[67] L. V. Butov, A. C. Gossard, and D. S. Chemla, *Nature* **418**, 751 (2002).

[68] J. A. Seamons, C. P. Morath, J. L. Reno, and M. P. Lilly, *Phys. Rev. Lett.* **102**, 026804 (2009).

[69] S. Mukerjee, C. Xu, and J. E. Moore, *Phys. Rev. Lett.* **97**, 120406 (2006).

[70] D. Podolsky, S. Chandrasekharan, and A. Vishwanath, *Phys. Rev. B* **80**, 214513 (2009).

[71] E. Tutuc, M. Shayegan, and D. A. Huse, *Phys. Rev. Lett.* **93**, 036802 (2004).

[72] M. Kellogg, J. P. Eisenstein, L. N. Pfeiffer, and K. W. West, *Phys. Rev. Lett.* **93**, 036801 (2004).

[73] J. P. Eisenstein and A. H. MacDonald, *Nature* **432**, 691 (2004).

[74] D. Blume and C. H. Greene, *Phys. Rev. A* **65**, 043613 (2002).

[75] P. Naidon, E. Tiesinga, W. F. Mitchell and P. S. Julienne, *New. J. Phys.* **9**, 19 (2007).

[76] For the inclusion of many-body effects see V. Pietilä, D. Pekker, Y. Nishida, and E. Demler, *Phys. Rev. A* **85**, 023621 (2012).

[77] L. P. Kadanoff and G. Baym, *"Quantum Statistical Mechanics: Green's Function Methods in Equilibrium and Nonequilibrium Problems"* (W.A. Benjamin Inc, New York, 1962).

[78] M. Babadi and E. Demler, *Phys. Rev. A* **84**, 033636 (2011).

[79] P. Wicke, S. Whitlock, and N. J. van Druten, arXiv:1010.4545.

[80] T. Kinoshita, T. Wenger, and D. S. Weiss, *Science* **305**, 1125 (2004).

[81] B. Paredes *et al.*, *Nature* **429**, 277 (2004).

[82] D. Pekker *et al.*, *Phys. Rev. Lett.* **106**, 050402 (2011).

[83] B. Fröhlich, M. Feld, E. Vogt, M. Koschorreck, W. Zwerger, and M. Köhl, *Phys. Rev. Lett.* **106**, 105301 (2011).

[84] A. T. Sommer, L. W. Cheuk, M. J. H. Ku, W. S. Bakr, and M. W. Zwierlein, *Phys. Rev. Lett.* **108**, 045302 (2012).

[85] J. W. Negele and H. Orland, *"Quantum many-particle systems"* (Westview Press, 1988).

[86] S. Sala *et al.*, *Phys. Rev. Lett.* **110**, 203202 (2013).

[87] H. Moritz, T. Stöferle, K. Günter, M. Köhl, and T. Esslinger, *Phys. Rev. Lett.* **94**, 210401 (2005).

[88] C. Chin, R. Grimm, P. Julienne, and E. Tiesinga, *Rev. Mod. Phys.* **82**, 1225 (2010).

[89] A. Widera *et al.*, *Phys. Rev. Lett.* **100**, 140401 (2008).

[90] G. Modugno, M. Modugno, F. Riboli, G. Roati, and M. Inguscio, *Phys. Rev. Lett.* **89**, 190404 (2002).

[91] G. Thalhammer *et al.*, *Phys. Rev. Lett.* **100**, 210402 (2008).

[92] J. Catani, L. De Sarlo, G. Barontini, F. Minardi, and M. Inguscio, *Phys. Rev. A* **77**, 011603(R) (2008).

[93] S. B. Papp, J. M. Pino, and C. E. Wieman, *Phys. Rev. Lett.* **101**, 040402 (2008).

[94] A. Bohr, B. R. Mottelson, and D. Pines, *Phys. Rev.* **110**, 936 (1958).

[95] M. Alford, A. Schmitt, K. Rajagopal, T. Schäfer, *Rev. Mod. Phys.* **80**, 1455 (2008).

[96] M. Tinkham, *"Introduction to Superconductivity"* (McGraw-Hill Book Co., New York, 1975).

[97] V. Mourik *et al.*, *Science* **336**, 1003 (2012).

[98] N. Prokof'ev and B. Svistunov, *Phys. Rev. Lett.* **99**, 250201 (2007).

[99] S. Jochim *et al.*, *Phys. Rev. Lett.* **91**, 240402 (2003).

[100] S. Jochim *et al.*, *Science* **302**, 2101 (2003).

[101] W. V. Liu and F. Wilczek, *Phys. Rev. Lett.* **90**, 047002 (2003).

[102] M. M. Forbes, E. Gubankova, W. V. Liu, and F. Wilczek, *Phys. Rev. Lett.* **94**, 017001 (2005).

[103] C. Honerkamp, and W. Hofstetter, *Phys. Rev. Lett.* **92**, 170403 (2004).

[104] Á. Rapp, G. Zaránd, C. Honerkamp, and W. Hofstetter, *Phys. Rev. Lett.* **98**, 160405 (2007).

[105] Á. Rapp, W. Hofstetter, and G. Zaránd, *Phys. Rev. B* **77**, 144520 (2008).

[106] R. W. Cherng, G. Refael, and E. Demler, *Phys. Rev. Lett.* **99**, 130406 (2007).

[107] I. Titvinidze *et al.*, *New. J. Phys.* **13**, 035013 (2011).

[108] C. Chin and E. C. Mueller, *Physics* **6**, 118 (2013).

[109] H. Miyake, G. A. Siviloglou, C. J. Kennedy, W. C. Burton, and W. Ketterle, *Phys. Rev. Lett.* **111**, 185302 (2013).

[110] G. Jotzu *et al.*, *Nature* **515**, 237 (2014).

[111] Y. Shin, C. H. Schunck, A. Schirotzek, and W. Ketterle, *Nature* **451**, 689 (2008).

[112] P. Fulde, R. A. Ferrell, *Phys. Rev.* **135**, A550 (1964).

[113] A. I. Larkin, Yu. N. Ovchinnikov, *Zh. Eksp. Teor. Fiz.* **47**, 1136 (1964).

[114] A. I. Larkin, Y. N. Ovchinnikov, *Sov. Phys. JETP* **20**, 762 (1965).

[115] G. B. Partridge, W. Li, R. I. Kamar, Y. Liao, and R. G. Hulet, *Science* **311**, 503 (2006).

[116] M. W. Zwierlein, A. Schirotzek, C. H. Schunck, and W. Ketterle, *Science* **311**, 492 (2006).

[117] D. S. Sarma, *J. Phys. Chem. Solids* **24**, 1029 (1963).

[118] A. M. Clogston, *Phys. Rev. Lett.* **9**, 266 (1962).

[119] A. V. Gorshkov *et al.*, *Nature Phys.* **6**, 289 (2010).

[120] C. Wu, J. P. Hu, and S. C. Zhang, *Phys. Rev. Lett.* **91**, 186402 (2003).

[121] M. Bartenstein *et al.*, *Phys. Rev. Lett.* **94**, 103201 (2005).

[122] K. M. O'Hara, *New. J. Phys.* **13**, 065011 (2011).

[123] C. Honerkamp, W. Hofstetter, *Phys. Rev. B* **70**, 094521 (2004).

[124] R. P. Feynman, *Statistical Mechanics: A Set Of Lectures* (Westview Press, 1998).

[125] T. Ozawa and G. Baym, *Phys. Rev. A* **82**, 063615 (2010).

[126] J. Cardy, *Scaling and Renormalization in Statistical Physics*, (Cambridge Lecture Notes in Physics, 1996).

[127] A. Aharony in *Phase Transitions and Critical Phenomna, Vol. 6*, edited by C. Domb and M. S. Green (Academic Press, 1977).

[128] P. Calabrese, A. Pelissetto, and E. Vicari, *Phys. Rev. B* **67**, 054505 (2003).

[129] E. Vicari and J. Zinn-Justin, *New J. Phys.* **8**, 321 (2006).

[130] A. Aharony and S. Fishman, *Phys. Rev. Lett.* **37**, 1587 (1976).

[131] R. A. Cowley, A. D. Bruce, *J. Phys. C: Solid State Phys.* **11**, 3577 (1978).

[132] A. Aharony, *Phys. Rev. Lett.* **88**, 059703 (2002).

[133] M. Kanász-Nagy and G. Zaránd, Phys. Rev. B **86**, 064519 (2012).

[134] J. H. Huckans, J. R. Williams, E. L. Hazlett, R. W. Stites, and K. M. O'Hara, *Phys. Rev. Lett.* **102**, 165302 (2009).

[135] J. R. Williams *et al.*, *Phys. Rev. Lett.* **103**, 130404 (2009).

[136] A. Kantian *et al.*, *Phys. Rev. Lett.* **103**, 240401 (2009).

[137] T. Kraemer *et al.*, *Nature* **440**, 315 (2006).

[138] T. B. Ottenstein, T. Lompe, M. Kohnen, A. N. Wenz, and S. Jochim, *Phys. Rev. Lett.* **101**, 203202 (2008).

[139] N. D. Mermin, *Rev. Mod. Phys.* **51**, 591 (1979).

[140] B. A. Dubrovin, A. T. Fomenko, and S. P. Novikov, *"Modern Geometry - Methods and Applications, Part II: The Geometry and Topology of Manifolds"* (Graduate Texts in Mathematics, Springer, 1985).

[141] R. Rajaraman, *"Solitons and Instantons: An Introduction to Solitons and Instantons in Quantum Field Theory"* (Elsevier Science B. V., 1982).

[142] M. Pospelov *et al.*, *Phys. Rev. Lett.* **110**, 021803 (2013).

[143] G. E. Volovik, *"The Universe in a Helium Droplet"* (Clarendon Press, 2003).

[144] G. 't Hooft, *Nucl. Phys. B* **79**, 276 (1974).

[145] A. M. Polyakov, *JETP Lett* **20**, 194 (1974).

[146] P. A. M. Dirac, *Proc. Roy. Soc. Lond.* **A133**, 60 (1931).

[147] M. W. Ray, E. Ruokokoski, S. Kandel, M. Möttönen, and D. S. Hall, *Nature* **505**, 657 (2014).

[148] T. H. R. Skyrme, *Nucl. Phys.* **31**, 556 (1962).

[149] T. H. R. Skyrme, *Proc. Roy. Soc. Lond.* **A260**, 127 (1961).

[150] S. E. Barrett, G. Dabbagh, L. N. Pfeiffer, K. W. West, and R. Tycko, *Phys. Rev. Lett.* **74**, 5112 (1995).

[151] A. Schmeller, J. P. Eisenstein, L. N. Pfeiffer, and K. W. West, *Phys. Rev. Lett.* **75**, 4290 (1995).

[152] E. H. Aifer, B. B. Goldberg, and D. A. Broido, *Phys. Rev. Lett.* **76**, 680 (1996).

[153] D. R. Leadley *et al.*, *Phys. Rev. Lett.* **79**, 4246 (1997).

[154] S. P. Shukla, M. Shayegan, S. R. Parihar, S. A. Lyon, N. R. Cooper, and A. A. Kiselev, *Phys. Rev. B* **61**, 4469 (2000).

[155] Y. P. Shkolnikov, S. Misra, N. C. Bishop, E. P. De Poortere, and M. Shayegan, *Phys. Rev. Lett.* **95**, 066809 (2005).

[156] M. Lee, W. Kang, Y. Onose, Y. Tokura, and N. P. Ong, *Phys. Rev. Lett.* **102**, 186601 (2009).

[157] A. Neubauer *et al.*, *Phys. Rev. Lett.* **102**, 186602 (2009).

[158] T. Schulz *et al.*, *Nat. Phys.* **8**, 301 (2012).

[159] S. Mühlbauer *et al.*, *Science* **323**, 915 (2009).

[160] X. Z. Yu *et al.*, *Nature* **465**, 901 (2010).

[161] S. Seki, X. Z. Yu, S. Ishiwata, and Y. Tokura, *Science* **336**, 198 (2012).

[162] D. J. P. Morris *et al.*, *Science* **326**, 411 (2009).

[163] C. Castelnovo, R. Moessner, and S. L. Sondhi, *Nature* **451**, 42 (2008).

[164] Y. Brihaye, C. T. Hill, and C. K. Zachos, *Phys. Rev. D* **70**, 111502(R) (2004).

[165] G. H. Derrick, *J. Math. Phys.* **5**, 1252 (1964).

[166] H. T. C. Stoof, E. Vliegen, and U. Al Khawaja, *Phys. Rev. Lett.* **87**, 120407 (2001).

[167] U. Al Khawaja, and H. T. C. Stoof, *Nature* **411**, 918 (2001).

[168] J. Choi, S. Kang, S. W. Seo, W. J. Kwon, and Y. Shin, *Phys. Rev. Lett.* **111**, 245301 (2013).

[169] J. Choi, W. J. Kwon, and Y. Shin, *Phys. Rev. Lett.* **108**, 035301 (2012).

[170] J. Choi *et al.*, *New J. Phys.* **14**, 053013 (2012).

[171] L. S. Leslie, A. Hansen, K. C. Wright, B. M. Deutsch, and N. P. Bigelow, *Phys. Rev. Lett.* **103**, 250401 (2009).

[172] J. Armaitis, H. T. C. Stoof, and R. A. Duine, *Phys. Rev. Lett.* **110**, 260404 (2013).

[173] T. Ohmi, and K. Machida, *J. Phys. Soc. Jpn.* **67**, 1822 (1998).

[174] C. K. Law, H. Pu, and N. P. Bigelow, *Phys. Rev. Lett.* **81**, 5257 (1998).

[175] J. Lovegrove, M. O. Borgh, and J. Ruostekoski, *Phys. Rev. Lett.* **112**, 075301 (2014).

[176] R. A. Battye, N. R. Cooper, and P. M. Sutcliffe, *Phys. Rev. Lett.* **88**, 080401 (2002).

[177] E. Demler, and F. Zhou, *Phys. Rev. Lett.* **88**, 163001 (2002).

[178] A. M. Turner, R. Barnett, E. Demler, and A. Vishwanath, *Phys. Rev. Lett.* **98**, 190404 (2007).

[179] A. E. Leanhardt, Y. Shin, D. Kielpinski, D. E. Pritchard, and W. Ketterle, *Phys. Rev. Lett.* **90**, 140403 (2003).

[180] D. M. Stamper-Kurn *et al.*, *Phys. Rev. Lett.* **80**, 2027 (1998).

[181] I. F. Herbut, and M. Oshikawa, *Phys. Rev. Lett.* **97**, 080403 (2006).

[182] R. Barnett, A. Turner, and E. Demler, *Phys. Rev. Lett.* **97**, 180412 (2006).

[183] J. Stenger, S. Inouye, D. M. Stamper-Kurn, H.-J. Miesner, A. P. Chikkatur, and W. Ketterle, *Nature* **396**, 345 (1998).

[184] M. P. A. Fisher, P. B. Weichman, G. Grinstein, and D. S. Fisher, *Phys. Rev. B* **40**, 546 (1989).

[185] B. M. Caradoc-Davies, *"Vortex Dynamics in Bose-Einstein Condensates"* (Ph.D. Thesis, 2000).

[186] J.-P. Martikainen, A. Collin, and K.-A. Suominen, *Phys. Rev. Lett.* **88**, 090404 (2002).

[187] M. A. Nielsen and I. L. Chuang, *"Quantum Computation and Quantum Information"* (Cambridge University Press, 2010).

[188] L. I. Schiff and H. Snyder, *Phys. Rev.* **55**, 59 (1939).

[189] R. W. Helmes, T. A. Costi, and A. Rosch, *Phys. Rev. Lett.* **101**, 066802 (2008).

[190] Y. Kawaguchi, and M. Ueda, *Phys. Rep.* **520**, 253 (2012).

[191] P. W. Anderson, *Phys. Rev.* **86**, 694 (1952).

[192] E. L. Hill, *Am. J. Phys.* **22**, 211 (1954).

[193] J. J. Sakurai, *"Modern Quantum Mechanics"* (Addison-Wesley, 1994).

[194] M. Kanász-Nagy, E. A. Demler and G. Zaránd, arXiv:1401.5798 (2014).

[195] M. Kanász-Nagy, B. Dóra, E. A. Demler and G. Zaránd, *Sci. Rep.* **5**, 7692 (2015).